Master's thesis

NTNU
Norwegian University of Science and Technology
Faculty of Natural Sciences
Department of Materials Science and Engineering

Marie R. Sørlie

Fracture modes in naturally aged aluminium alloys and an investigation of accelerated age hardening by incremental stretching

Master's thesis in Materialteknologi
Supervisor: Bjørn Holmedal
June 2023

NTNU
Norwegian University of
Science and Technology

Marie R. Sørlie

Fracture modes in naturally aged aluminium alloys and an investigation of accelerated age hardening by incremental stretching

Master's thesis in Materialteknologi
Supervisor: Bjørn Holmedal
June 2023

Norwegian University of Science and Technology
Faculty of Natural Sciences
Department of Materials Science and Engineering

NTNU
Norwegian University of
Science and Technology

Preface

This Master thesis was conducted at the Department of Materials Science and Engineering at NTNU, Trondheim.

This project would not be possible without the help of several people both regarding practical and theoretical work. Special thanks to my supervisor Dr. Bjørn Holdmedal who has provided me with useful discussions and helpful feedback throughout this project, both regarding the experimental work and the writing of the thesis.

I also wish to thank Pål C. Skaret, Marit E. O. Odden, Ruben Å. Hansen and Yingda Yu for providing the required training on the equipment used for the experiments, and for showing great patient and resourcefulness in helping me with the more challenging parts of the lab work.

And finally a great big thank you to my parents, brothers and grand parents for having been kind and supportive throughout this whole project.

Abstract

A previous investigation on the effects of cyclic aging on 7xxx aluminium alloys from flat extruded profiles found that both natural aging and certain combinations of cyclic aging lead to early slant ductile fractures during tensile testing. The cause of these early fractures is unknown, but the possibility of dynamic strain aging being the cause was ruled out. This thesis investigated the potential correlation between texture and the early ductile slant fractures, with the hypothesis being that specimens with a rolling texture would experience early slant ductile fractures while specimens with axis-symmetric textures would experience necking prior to fracture. The potential occurrence of local necking was also be checked using two different specimen geometries. In addition to this the ability of achieving large strains in tensile specimens using incremental elongation testing was investigated and this thesis also focused on the effect of strain rate to see if dynamic strain aging, previously found to be a problem with the incremental elongation testing, could be avoided.

To investigate the effect of texture tensile specimens with 6x6 mm cross sections were taken from the middle and edges of a naturally aged 7108 massive extruded profile, where the middle specimens were assumed to have an axis-symmetric texture and the edges a rolling texture. Two different specimen geometries were also taken from a naturally aged 7108 flat extruded profile, the first with a square cross section of 3x3 mm and the second with a rectangular cross section of 3x24 mm. Tensile tests were performed on all the specimen types and the fracture surfaces analysed using light optical microscopy, secondary and backscatter electron imaging and EDS analysis. EBSD scans were done on the middle and edge specimens to determine the texture.

None of the specimens experienced necking, neither diffuse or local. All fractures where slant fractures and the suspected cause was the occurrence of a local plastic instability, in this case the formation of a shear band, resulting in a softening along the direction of the maximum shear stress. It was determined that the fracture surfaces of the edge specimens had ductile characteristics, while the surfaces of the middle, square and rectangular specimens had a brittle character. It is suspected that the middle specimens experienced a mix of transgranular and intergranular fracture due to precipitation free zones around the grain boundaries leading to early fracture rather than necking. The backscatter imaging reviled particles embedded in the fracture surfaces identified as constituent particles using EDS analysis. The EBSD scans also reviled that the edge specimens, as with the middle

specimens, had a fairly axis-symmetric texture contrary to what was assumed. The effect of texture was therefor not observed here both due to the lack of texture differences and the occurrence of precipitation free zones.

For the incremental elongation testing tensile specimens were taken from 6082 and 7003 flat extruded profiles with cross section of 6x6 mm. Three different strain rates for the increments were tested on each alloy, 0,05, 0,07 and 0,1 s^{-1}. All specimens were solutionized right before the elongation testing. The strains achieved here were compared to the uniform strains achieved on solutionized specimens in a regular tensile test and specimens aged to T6 found in literature. For the 6082 specimens the largest uniform strain achieved was 44% using a strain rate of 0,05 s^{-1}, compared to 12% and 6% for solutionized and T6 tensile tested specimens. For the 7003 specimens the largest uniform strain achieved was 55% using a strain rate of 0,1 s^{-1}, compared to 10% and 9% for solutionized and T6 tensile tested specimens. However, dynamic strain aging occurred in all cases, leading to rough and uneven surfaces and slant fractures. The fracture surface of a 7003 specimen was investigated using the same methods as with the 7108 tensile specimens. The fracture surface had a ductile character with particles embedded in dimples reviled to be constituent particles through EDS analysis. The incremental elongation tests showed that the strain rates achievable on the equipment used was not great enough to avoid dynamic strain aging.

Sammendrag

En tidligere undersøkelse av effekten av syklisk elding på 7xxx aluminiumslegeringer fra flate ekstruderte profiler fant at både naturlig elding og visse kombinasjoner av syklisk elding førte til tidlige duktile skjærbrudd under strekktesting. Årsaken til disse tidlige bruddene er ukjent, men dynamisk tøyningselding har blitt utelukket. Denne avhandlingen undersøkte den potensielle sammenhengen mellom tekstur og tidlige duktile skjærbrudd, med hypotesen om at prøver med valsetekstur ville oppleve tidlige duktile skjærbrudd mens prøver med aksesymmetrisk tekstur ville oppleve necking før brudd. Den potensielle forekomsten av lokal necking ble også undersøkes ved å teste to ulike prøvegeometrier. I tillegg ble muligheten for å oppnå store tøyninger i strekkprøver ved bruk av inkrementell forlengelse undersøkt og denne avhandlingen fokuserte på effekten av tøyningshastighet for å se om dynamisk tøyningselding, som tidligere har vært et problem, kan unngås.

For å undersøke effekten av tekstur ble strekkprøver med et tverrsnitt på 6x6 mm tatt fra midten og kantene av et naturlig eldet 7108 massivt ekstrudert profil, hvor midt-prøvene da ble antatt å ha en aksesymmetrisk tekstur og kant-prøvene en valsetekstur. To ulike prøvegeometrier ble og tatt fra et 7108 flatt ekstrudert profil, den første med et kvadratisk tverrsnitt på 3x3 mm og den andre med et rektangulært tverrsnitt på 3x24 mm. Strekktester ble utført på alle prøvetypene og bruddflatene ble undersøkt ved bruk av lysmikroskopi, SEM og EDS-analyse. EBSD scan ble gjort av midt- og kant-prøver for å avgjøre teksturen.

Ingen av prøvene opplevde necking, verken diffus eller lokal. Alle bruddene var skjær-brudd og det mistenkes at grunnen var forekomst av en lokal plastisk instabilitet, i dette tilfelle et skjærbånd, som gjorde materialet svakere i retningen av maximum skjærspen-ning. Bruddflaten til kant-prøvene ble fastslått å ha en duktil karakter, mens bruddflatene til midt-, kvadrat- og rektangulærprøvene hadde en sprø karakter. Det ble mistenkt at midt-prøvene opplevde en kombinasjon av et transgranulært og intergranulært brudd på grunn av presipitatfrie soner langs korngrensene som førte til tidlige brudd før necking. SEM bildene viste partikler på bruddflaten til alle prøvene, og disse ble bestemt å være konstitutive partikler basert på EDS-analysen. EBSD scannene viste også at kant-prøvene, slik som med midt-prøvene, hadde en relativt aksesymmetrisk tekstur i motsetning til hva som var forventet. Effekten av tekstur ble derfor ikke observert her, både på grunn av manglende teksturforskjeller og presipitatfrie soner.

For den inkrementelle forlengelsestestingen ble strekkprøver tatt fra 6082 og 7003 flate ekstruderte profiler. Tre ulike tøyningshastigheter ble testet for hver legering, 0,05, 0,07 og 0,1 s^{-1}. Alle prøvene ble innherdet rett før testing. Tøyningene oppnådd her ble sammenlignet med de uniforme tøyningene oppnådd på innherdede prøver utsatt for vanlig strekktesting og prøver eldet til T6 fra litteraturen. For 6082-prøvene var den lengste uniforme tøyningen oppnådd ved en tøyningshastighet på 0,05 s^{-1}, sammenlignet med 12% og 6% for innherdede og T6 strekktestede prøver. For 7003-prøvene var den lengste uniforme tøyningen oppnådd ved en tøyningshastighet på 0,1 s^{-1}, sammenlignet med 10% og 9% for innherdede og T6 strekktestede prøver. Dynamisk tøyningselding forekom derimot i alle tilfellene, og førte til ujevne overflater og skjærbrudd. Bruddflaten av en 7003-prøve ble undersøkt ved bruk av samme metoder som for 7108-prøvene nevnt over. Bruddflaten hadde en duktil karakter med partikler observert i bunden av dimpler, funnet å være konstitutive partikler basert på EDS-analysen. Den inkrementelle forlengelsestestingen viste at tøyningshastighetene som var oppnåelig på utstyret brukt i dette forsøket ikke var høye nok til å unngå dynamisk tøyningselding.

Table of Contents

List of Figures

List of Tables

Chapter 1

Introduction

1.1 Background

Due to their high strength and relatively low weight 6xxx and 7xxx aluminium alloys are being used more frequently in the automobile, aerospace and construction industry as a replacement for steel. In terms of use in transportation vehicles the light weight results in lower fuel consumption which in term leads to better fuel economics and less emissions. Aluminium alloys of the 6xxx and 7xxx series are medium to high strength alloys making it possible for them to be used for structural elements in the automobile industry. For instance 7xxx alloys are being used for bumpers [1].

Due to the current interest in aluminium alloys and their use in structural components for the automobile, aerospace and construction industry, mapping out and understanding their limitations as well as their strengths is important. A resent investigation of flat extruded 7xxx grade aluminium alloys comparing the strengthening effect of different aging methods Shah et al. [2] found that some of the aging methods led to early slant ductile fracture during tensile testing prior to necking. This master thesis will continue to research the findings of Akash Gopal's [3] thesis, which is were the slant fractures in 7003 specimens, taken from an extruded flat profile, were documented.

In addition to investigating these slant fractures, formability will also be investigated in the form of incremental elongation testing. As the demand for these medium to high strength aluminium alloys increases, so does the need for more complex geometries. This thesis will investigate the effects of incremental elongation testing on both 6082 and 7003 alloys as a continuation of the project work "Enhanced formability in tension by deformation induced precipitation" [4] from the previous semester, where cyclic and incremental elongation testing of 6082 tensile specimens were attempted.

1.2 Aim and objective

Regarding the investigation of the non ductile slant fractures the aim is to try and determine if texture has an impact on weather or not necking occurs prior to fracture. The 7003 specimens used by Gopal [3] were all taken from an extruded flat profile and assumed to have a rolling texture. The hypothesis is that 7003 specimens with a rolling texture will experience a slant ductile fracture prior to diffuse necking, while materials with an axis-symmetric texture will develop a diffuse neck.

In order to investigate the effect of texture tensile specimens will be taken from different areas of a 7108 massive extruded profile where the center of the profile is assumed to have an axis-symmetric texture and the edges a rolling texture. This will be confirmed by doing EBSD scans of different areas in the massive profile to map out the texture.

Tensile tests will then be performed. The results from the specimens from the edges and the middle of the massive extruded profile will be compared based on the stress-strain curves acquired and on the state of the fracture surfaces. Light optical microscopy, secondary electron (SE) and backscatter electron (BSE) imaging and EDS analysis will be used to analyse the fractures. The results will hopefully help determine textures effect on the plastic behaviour of the tensile specimens as well as the characteristics of the fracture surfaces and fracture modes.

In addition to this, tensile tests will be performed on specimens taken from a 7108 flat extruded profile to see if different geometries are affected differently due to anisotropy. A specimen with a square cross section of 3x3 mm will be compared to a specimen with a rectangular cross section of 3x24mm, and the aim is to observe if the rectangular specimens experience localized necking or not. The resulting fractures of these specimens will also be analysed with the aim of characterizing the fracture surfaces and determining fracture modes.

Regarding the investigation of incremental elongation testing this is a continuation of the experiments from the previous semester's project work [4], where 6082 specimens were tested. These experiments will also be conducted using solutionized specimens in a setup where they are stretched in small increments and then held still for a few seconds before the next increment. The hypothesis was, and still is, that Considere's necking criterion can be avoided by stretching the specimen into uniform plastic deformation where it work hardens, pushing the strain necessary for the onset of necking further for each incremental elongation so that in the next increment the necessary strain is even higher and necking will still not occur. Another assumption is that the work hardening effect comes from precipitation along vacancies from the solutionizing and from jogs on screw dislocations climbing, causing a strengthening of the material.

Considerable elongations were achieved for the 6082 specimens in the project work [4], but dynamic strain aging appeared to be a limiting factor for this method on this material. This thesis will investigate if the same problem occur in 7003 specimens, and if an increase

in strain rate, up to what the machine can tolerate, can help prevent the occurrence of dynamic strain aging.

For the 6082 specimens from last semester the slant fractures had a rough and dimpled fracture surfaces when investigated using SE imaging in the SEM, indicating a ductile fracture. EDS analysis were performed on particles observed embedded in the dimples. The 7003 specimens will be investigated similarly, with the addition of BSE imaging, in order to try and determine the fracture mode. An EBSD scan will be done to map out the texture both relevant to the incremental elongation testing and to confirm that the material used by Gopal [3] had a rolling texture.

In Chapter 2 necessary theory will be presented relating to the subjects as well as relevant research used to understand the findings from the experiments and subsequent analyses. Chapter 3 will cover the materials and methods used for testing and analysis and the following results are presented in Chapter 4, where the results from the tensile tests and incremental elongation tests are divided into two separate sections. In Chapter 5 the results will then be discussed and compared to relevant theory and previous findings, and a conclusion to the findings of this thesis will be given in Chapter 6. Chapter 7 will provide suggestions for future work on the topics.

Chapter 2

Theory

2.1 Wrought aluminium alloys

Aluminium is a metal with relatively low density, good corrosion resistance and high formability. Due to the low strength of pure aluminium it is often alloyed with different elements to increase the strength, and to achieve other properties like for example low recrystallisation tendencies during heat treatment or to promote precipitation during age hardening [1]. The type and amounts of alloying elements determine what properties are added, enhanced or limited. There are mainly two groups of aluminium alloys, cast alloys and wrought alloys. Cast alloys consist of a single phase with the alloying elements in solid solution. These alloys are non-heat treatable and cannot be precipitation hardened, making the main strengthening mechanism solid solution hardening. Wrought alloys are strengthened through precipitation hardening. These precipitates are intermetallic particles precipitated during aging. The cast and wrought alloys are further categorized into different grades [5].

For wrought aluminium alloys these grades consist of four digits where the first digit is the most descriptive as it is related to the major alloying elements of the alloy. The remaining digits are serial numbers, where the second digit in some cases represent a similarity between two different alloys [1]. 6xxx grade aluminium alloys are primarily alloyed with magnesium (Mg) and silicone (Si), signified by the first digit, and sometimes copper (Cu), in addition to small amounts of other elements like manganese (Mn) and chromium (Cr) [5, 6].They are considered medium strength alloys, suited for forming processes such as extrusion and forging, and are often used in the car manufacturing industry [1].

7xxx grade aluminium alloys are primarily alloyed with zinc (Zn) and magnesium (Mg), again signified by the first digit, and in some cases small amounts of other elements such as zirconium (Zr) or copper (Cu) [5, 6]. These alloys are considered high strength alloys generally used for applications that require a tolerance for high stresses. This grade is therefore commonly used in structural components in the air craft- and automobile industry [5]. In terms of forming processes it is suited for both forging, extrusion and

sheet rolling [1].

2.2 Precipitation strengthening in aluminium alloys

In wrought aluminium alloys the primary strengthening mechanism is precipitation strengthening. Precipitation strengthening, or precipitation hardening, is the strengthening of a material through small coherent or semi-coherent particles that restrict the movement of dislocations, thus increases the strain required to deform the metal. In the case of aluminium alloys these dispersed particles are precipitates usually achieved through age hardening. It should be mentioned that solid solution strengthening, work hardening and grain size also affects the strength of these alloys, but to a lesser degree [6]. The strengthening effect of the particles on the material depends mainly on the distance between particles, if the particles are shearable or not and the coherency of the particles.

2.2.1 The strengthening effect of particle density

The strengthening effect of shearable particles increases with increasing particle density, and the higher the density the lower the mean distance between particles in the metal. This means that during dislocation glide the dislocations are affected by a larger number of particles that inhibit or limit their movement, thus increasing the stress required to achieve plastic deformation. The mean distance between particles in a given control volume is [7]:

$$\lambda = \sqrt{\frac{2\pi}{3}} \cdot \frac{r}{\sqrt{f}} \tag{2.1}$$

Where λ is the mean distance between all particles piercing the slip area, r is the particle size and f is the volume fraction of particles. This is assuming that the particles are spherical and relatively weak pinning points for dislocations. As this strength contribution is related to particle density it is here further connected to the age hardening of aluminium, especially in the case of artificial aging. When the material is aged past peak hardening a coarsening of the alloy occur where the larger particles will grow at the expense of the smaller ones, causing them to dissolve. This leads to r increasing and f decreasing, which according to equation 2.1 causes the mean distance between particles to grow and ultimately have a negative impact on strength [7].

2.2.2 The strengthening effect of particle shearability

Depending on weather or not the particles are shearable they can inhibit or limit dislocation glide in one of two ways. For non-shearable particles the dislocations will bow out between the dispersed particles in its glide plane. For shearable particles the the dislocations will cut through them. Both mechanisms require a larger shear stress in order

for dislocations to move past the particles compared to moving unhindered through the matrix, thus increasing the strength [8].

In most cases dislocations will not immediately shear the particles on encounter, but rather bow out a little between the particles before shearing them. In the category of shearable particles there are strong and weak ones, depending on the angle between dislocation segments bowing out around a particle. The angle is shown in Figure 2.1. When the angle is large the particle is considered weak, whilst strong particles give smaller angles. In the case of strong shearable particles the strengthening contribution of the precipitates are also related to the force a dislocation experiences when meeting such a particle, in addition to the stress required to shear it. This force is equal to [9]:

$$F = 2\Gamma cos\frac{\theta}{2} \tag{2.2}$$

Where Γ is the line tension pulling on the dislocation segment, and θ is the angle between the dislocation bow outs. Both these values are marked in Figure 2.1.

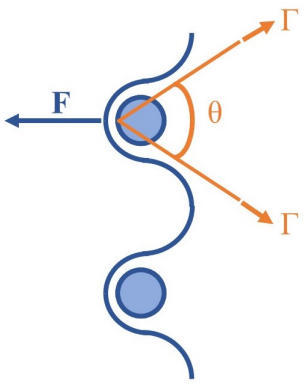

Figure 2.1: The θ angle between dislocation bow outs, the line tensions Γ and the force F the dislocation experience from the particle.

If a dislocation encounters non-shearable particles in the slip plane, it will bow out between the particles, as they are "rigid". The dislocation will protrude further out in the space between them as the shear stress is increased. Eventually it will rejoin with other bowed segments, recombining into a line and leaving a dislocation loop around the particle, as Figure 2.2 depicts. The shear stress, τ, required for a dislocation to glide on a slip plane containing non-shearable particles is given as [7]:

$$\tau = \frac{Gb}{\lambda} \tag{2.3}$$

Where G is the shear modulus, b is the length of the burgers vector and λ is the mean distance between particles in the glide plane. The equation for the shear stress required for a dislocation to glide past these particles is similar to the critical stress required to activate

a Frank-Read source as both involves the dislocation segment bowing out. However, the bowing segments here do not function as actual Frank-Read sources and will only leave one dislocation loop around the particle before continuing its glide [7].

As seen from Equation 2.3 the shear stress is inversely proportional to the distance between the dispersed particles in the glide plane, meaning the smaller the distance the larger the shear force required. When a dislocation loop is formed around a particle this, in practicality, has an effect corresponding to increasing the particle size, r, of the section of the particle cutting through the relevant slip plane. This in turn decreases the mean distance between particles, as seen from Equation 2.1, and their dislocation loops, meaning a larger shear stress will be needed for the next dislocation to pass [8, 7].

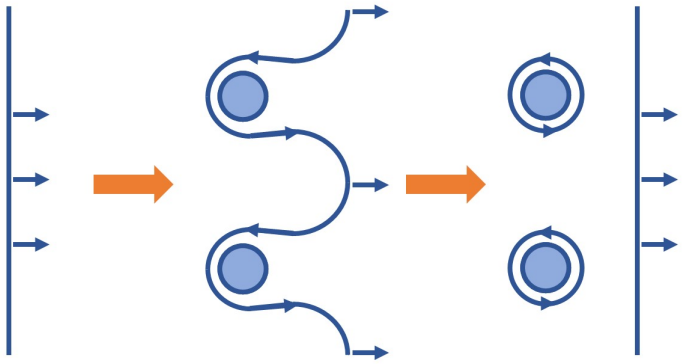

Figure 2.2: A dislocation gliding past non-shearable particles, resulting in the formation of dislocation loops.

When dislocations encounter shearable particles in the glide plane the dislocation will cut through them, as illustarted in Figure 2.3, leaving half of the particle displaced one Burgers vector. The shear stress required to cut through a particle is related to the formation of new surfaces and the breakdown of order of the particle. In order for a dislocation to shear a particle two new surfaces must be created and this requires a certain shear stress, as shown in Equation 2.4. As two new surfaces are created they are also displaced. This displacement requires an additional shear stress, as given in Equation 2.5 [7].

$$\tau = \frac{3f\gamma_s}{2r} \tag{2.4}$$

$$\tau = \frac{3f\gamma_p}{2b} \tag{2.5}$$

Here γ_s is the surface formation energy and γ_p is the interface energy per area due to local disorder. These equations are valid for weak particles when considering their interactions with straight dislocations. Both these shear stresses combine to the total shear stress required for the dislocation to shear the particle. There are other factors such as elastic

fields and coherency stress fields that also impact the total shear stress, but to a lesser degree [7].

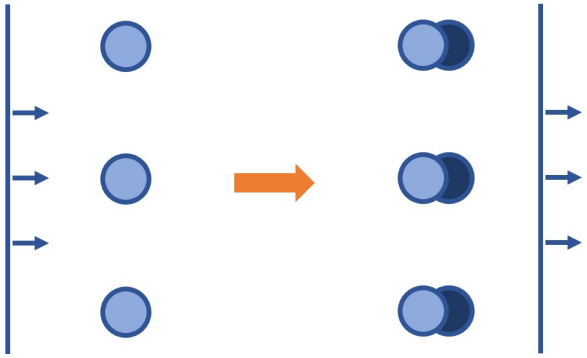

Figure 2.3: Shearable particles being cut by a dislocation resulting in one half being displaced one burgers vector.

2.2.3 The strengthening effect of particle coherency

The coherency between the precipitates and matrix is relevant to their strengthening effect. A particle is coherent with the matrix when the lattice planes of their crystal structures match up [10]. Although there in practise will be a small lattice misfit due to atom- and unit cell size differences, it is not great enough to prohibit the atoms of the interfaces to line up enough for them to bond together [9]. This occurs when the crystal structure of particle and matrix is the same or similar, leading to low interfacial energy compared to non-coherent particles [11]. Dislocations can only move through coherent particles that interfere with their glide plane. Since non-coherent particles are separate from the matrix they will have little effect on the dislocation glide as dislocations do not move between phases [8].

Coherent or semi-coherent particles have one or more sides connected to the matrix. These will interfere with the glide planes of dislocations and have an impact on the force required to move past them. In part this force is related to weather these precipitates are strong or weak particles, as mentioned above, but also to the strain misfit between the coherent areas between particle and matrix. This misfit strain has a strengthening effect on the material due to the increased stress required for the dislocations to move trough it. According to Ahmadi et al. [9] this coherency effect lead to an increase in precipitation strengthening with increasing particle size.

2.3 Aging of 6xxx and 7xxx aluminium alloys

The precipitation of particles in aluminium alloys are achieved through age hardening. Age hardening is a heat treatment technique where the material, in a state of supersaturated solid solution (SSSS), is left at a certain temperature over time to precipitate particles. The particles precipitated and their strength contribution depend on temperature and time, and the two main aging processes are natural aging and artificial aging. Natural aging is done at room temperature over longer periods of time whilst artificial aging is done at higher temperatures over shorter periods of time [6]. As the particles precipitated are separate phases from the matrix, weather the phase transformation will occur or not depends on if it lowers the free energy, Gibbs energy, of the system. In addition to it being thermodynamically possible an activation barrier for nucleation has to be reached. This barrier, ΔG, is determined by the negative contribution of the creation of the volume of the new particle and the positive contributions from the creation of an interface between the two surfaces and the misfit strain between them. These are the main contributions in the case of homogeneous phase transformations [11].

However, most phase transformations are heterogeneous meaning the particles precipitate on defects in the metal such as grain boundaries, dislocations, stacking faults, vacancies, inclusions and free surfaces. If the precipitation of a particle along a defect destroys it or reduces its free energy this gives a negative contribution to the activation barrier, and in some cases annihilates it completely. The equation for the activation energy barrier is given as [11]:

$$\Delta G = -V(\Delta G_v - \Delta G_s) + A\gamma - \Delta G_d \tag{2.6}$$

Where V is the volume of the particle, ΔG_v is the free energy released from volume reduction when the new particle is created, ΔG_s is the misfit strain energy, A is the area of the interface, γ is the energy required for the formation of a new surface area and ΔG_d is the free energy released from the destruction of a defect [11].

2.3.1 The formation of successful critical nuclei

The process of age hardening an alloy begins with a solution heat treatment. The material is heated up to a temperature below the melting temperature where the alloying elements are in solid solution. At what temperature solid solution occurs depends on the types- and weight percentages of alloying elements. The material is held at this temperature until all particles and impurities are assumed completely dissolved throughout the sample. Immediately after the solution heat treatment it is quenched in water. This rapid cooling prevents any phase transformations as there is little time for diffusion. Therefore the solid solution remains supersaturated at room temperature [6, 11].

In addition to dissolving impurities solutionizing the alloy increases the number of va-

cancies in it. Number of vacancies increases with increasing temperature, and as the quenching of the alloy prevents phase transformations, so it contributes to maintain the high numbers of vacancies. These vacancies become nucleation sites for the precipitates, but still have a relatively low ΔG_d meaning the activation energy barrier remains similar to the one for homogeneous nucleation. In this case the precipitation of particles is largely dependent on temperature, and a critical undercooling temperature must be reached before successful critical nuclei start to form. The number of successful critical nuclei is here determined by the rate of homogeneous nucleation in a solid, which is given in the equation below [11]:

$$N = \omega C_0 e^{-\frac{\Delta G_m}{kT}} \cdot e^{-\frac{\Delta G^*}{kT}} \tag{2.7}$$

Where N is the nucleation rate in the unit nuclei/$m^3 s^1$, ω is a factor representing the vibration frequency of the atoms and the area of the critical nucleus, C_0 is the number of atoms per unit volume in the phase, ΔG_m is the activation energy for atomic migration, T is temperature and ΔG^* is an activation energy barrier. As ΔG_m can be considered independent of temperature, a decrease in temperature rapidly causes the number of successful critical nuclei to increase. In order to achieve the best strengthening effect from the precipitates they need to evenly distributed with a shorter mean distance between particles and a reasonable size and coherency, as discussed in Chapter 2.2. This means achieving a good balance between nucleation and growth with the heat treatment. In addition to increasing the number of vacancies in the metal the solution heat treatment also ensures a more evenly distribution of the concentration of alloying elements, and promotes more even precipitation and not just along grain boundaries and other defects [11]. It should be mentioned that for some metals and alloys the presence of a large number of vacancies helps promote precipitation more than for others, and in these cases energy barriers for nucleation will be lower.

As the expression $-\frac{\Delta G_m}{kT}$ from Equation 2.7 represents the potential concentration of nuclei that increases with decreasing temperature, the expression $-\frac{\Delta G^*}{kT}$ represents atomic mobility. The mobility increases with temperature as it is diffusion related meaning the greatest nucleation rate, N, is obtained at the temperature at the intersection of these parameters, as demonstrated in Figure 2.4. It should be mentioned that in practice the nucleation rate is not constant, but will begin low before increasing gradually. Then as the first nuclei start to grow it will decrease as the solute atoms available now also supports this growth [11].

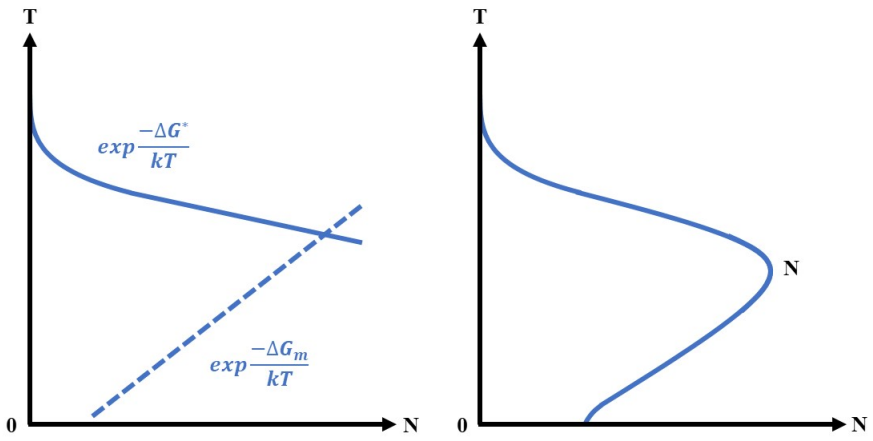

Figure 2.4: The figures show the combination of the expressions for the potential concentration of nuclei and atomic mobility into the nucleation rate N as a function of temperature [11].

2.3.2 The growth of precipitated particles in 6xxx and 7xxx alloys

As the formation of successful critical nuclei depends on temperature, so does the growth of the particles. However, the growth rate is determined by diffusion which in turn increases with increasing temperature, making these mechanisms competing. The growth rate of a particle in general varies with shape, but is in all cases diffusion related. After the solution heat treatment and quenching the alloy is age hardened. The temperature at which the alloy is hardened is then a combination of a temperature where nucleation will occur, and where growth rate is reasonable. There are mainly two types of aging processes that are time and temperature based, natural aging and artificial aging. Natural aging happens at room temperature over a longer period of time, usually several days or months, while artificial aging happens at higher temperatures over a shorter time period, often no longer than 24 hours. In some cases artificially aged material is first stored at room temperature where natural aging occur, before being further age hardened at higher temperatures [6, 11].

When an alloy is super saturated it is not stable and precipitation of particles will in general begin in order to reach a phase equilibrium, at a rate depending on temperature. At equilibrium most aluminium alloys will have a softer matrix with harder, non-coherent particles dispersed through it. However, these particles are not the first to be precipitated due to their high barrier of nucleation, resulting in several metastable intermediate phases being formed in a time and temperature related sequence ending in the final equilibrium phase. In the case of natural aging the precipitation process in 6xxx and 7xxx alloys start with the formation of GP zones, Guinier–Preston zones, followed by one or two transitional

phases and then the final phase [11].

The formation of GP zones and intermediate phases prior to the equilibrium phase is due to their activation energy barriers, as they are much lower than for the equilibrium phase. This significant difference in the barrier of nucleation is related to the interfacial energy between precipitates and matrix. The equilibrium phases of 6xxx and 7xxx alloys are a separate, intermetallic phases to their matrixe with complex crystal structures compared to it. Therefore these phases can only form with high energy incoherent interfaces, and although the driving force to precipitate the final phase is higher, the interfacial energy required to form two new non-coherent surfaces leads to the activation barrier being so high it is virtually impossible to reach. This is the bases for the formation of the intermediate phases [11].

In comparison these phases are intermediate stages with structures that are fully coherent or semi-coherent with the matrix, where the early stages have a higher level of coherency and structures more resembling of the matrix's. As the precipitates change towards the equilibrium phase they increase in size and elastic misfit strain, and form a structure more resembling of the final phase, resulting in less coherency. GP zones are often precipitated first, and they are fully coherent with the matrix where additionally the strain energy is also minimized through shape. The latter is the case for the intermediate phases as well. The formation of these transition phases result in the free energy of the alloy decreasing more rapidly compared to in a direct transition to the equilibrium phase [11].

2.3.3 The relationship between aging time and hardness

As mentioned above the different precipitates are closely linked to the hardness of the alloys, which is in term related to both the types of precipitates and their coarseness. Figure 2.5 shows a simplified aging curve for artificial aging which gives an overview over the general relationship between hardness and aging time for wrought aluminium alloys. After a certain aging period the alloy reaches peak hardening, and prior to that it is underaged [8]. Here the precipitates are often small and shearable and super saturated elements are still available in the matrix, meaning more particles can still be precipitated or the existing ones will grow, creating stronger dislocation obstacles. Early stage precipitates such as GP zones dominate in the first part. As the curve approaches peak hardening both the hardness of the alloy, nucleation rate and volume fraction of particles increases. There is also particle growth during this stage [11].

As the aging continues other intermediate phases start to develop, and these dominate at the point of peak hardening. For 6xxx and 7xxx alloys these are the β" and η' respectively [6]. Here there are no super saturated elements left and the volume fraction of particles is constant. If the aging process continues after this a coarsening of the particles occur as they continue to grow. However, as there are no more super saturated elements left in the matrix the smaller particles will dissolve in order to supply elements for larger particles to grow [6, 11]. This leads to fewer and larger particles, and as the particles grow they

change into the final, incoherent equilibrium phase. This phase contributes little to the strengthening of the materials as these particles do not inhibit dislocation glide, and so the hardness of the alloy decreases [11].

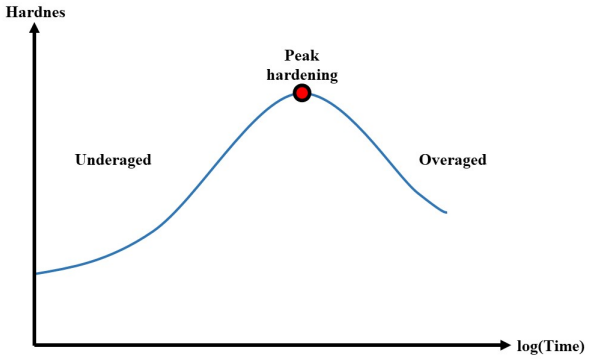

Figure 2.5: A simplified version of the artificial aging curve for aluminium alloys showing the relationship between hardness and aging time.

For natural aging the curve, as shown in Figure 2.6, is somewhat different. Room temperature is not enough for a coarsening of β" and η' into the equilibrium phase to occur, as the free energy barrier of this phase transition is to high [11]. Therefore the curve only increases slowly in hardness as it first precipitates the GP zones and then later the intermediate phases which have strong effects on the hardness of the alloy. It can take several months or even years for a the equivalent of peak hardening for artificially aged alloys to be reached [6].

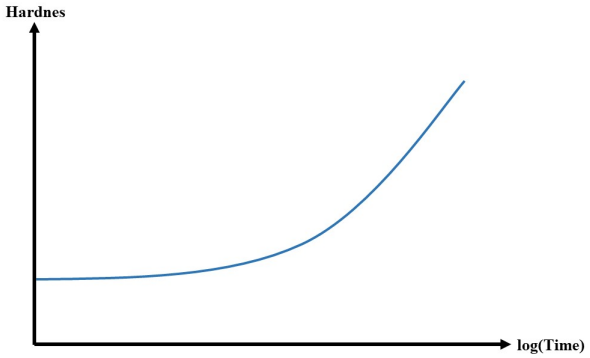

Figure 2.6: A simplified version of the natural aging curve for aluminium alloys showing the relationship between hardness and aging time.

2.3.4 T tempers for heat treatable aluminium alloys

With aluminum alloys heat treatments are used to control particle precipitation and microstructure, and the standardized treatments for wrought aluminium alloys are referred to as T tempers. The T tempers are a list of combinations of pre-treatements and age aging sequences that correspond to different results in terms of hardness, as well as microstructure, and they are covered in the standard NS-EN 515:2017. This standard is related to the main characteristic result of a heat treatment and an overview of what this treatment consisted of. For more specific instructions on solutionizing temperatures and aging times and temperatures the specifications for the individual alloy must be consulted. The T tempers range from T1-T9. T stands for thermally treated to a stable temper, and the following digits specify the sequence of heat treatments required to achieve the properties associated with that T temper. Table 2.1 list the parent categories of the T tempers [12].

Table 2.1: An overview of the T tempers and the treatment sequences they entail [12].

T tempers	Heat treatment sequence
T1	Cooled from an elevated temperature shaping process and naturally aged to a substantially stable condition.
T2	Cooled from an elevated temperature shaping process, cold worked and naturally aged to a substantially stable condition.
T3	Solution heat-treated, cold worked and naturally aged to a stable condition.
T4	Solution heat-treated and naturally aged to a substantially stable condition.
T5	Cooled from an elevated temperature shaping process and then artificially aged.
T6	Solution heat-treated and then artificially aged.
T7	Solution heat-treated and over-aged/stabilized.
T8	Solution heat-treated, cold worked and then artificially aged.
T9	Solution heat-treated4, artificially aged which are then cold worked.
T10	Cooled from an elevated temperature shaping process, cold worked and artificially aged.

The temper T6 is for most alloys equivalent to peak hardness where for 6xxx and 7xxx alloys the main precipitates are β" and η' as mentioned previously in this chapter. The prior T tempers correspond to earlier stages to peak hardness where the alloys are under aged and primarily contain either weaker precipitates or fewer precipitates of the ideal one. After T6 the alloys are over aged and less coherent or non-coherent particles begin to develop and increase in size, resulting in a decrease in volume fraction from T7 to T10 until eventually the main hardening particles or other particles are completely replaced with the equilibrium phase [12].

2.4 Particles in the 6xxx and 7xxx aluminium alloys

The alloy systems of aluminium alloys vary depending on alloying elements and heat treatments. Wrought alloys will contain a fine distribution of precipitates of varying types and sizes depending on the aging process [6]. Additionally the addition of manganese or chromium in 6xxx grade aluminium alloys and the addition of zirconium in 7xxx grade alloys can promote the formation of dispersoids. These are larger intermetallic particles that reduces or prevents recrystallization during for example annealing [13]. Contamination from some unwanted elements is difficult to avoid and these will also have an impact on the microstructure. Iron is a common impurity found in small amounts in most aluminium alloys. Due to its low solubility in aluminium larger, brittle, iron rich intermetallic particles called constituent particles are precipitated during the casting process [6]. Some alloys can also have precipitate free zones, small areas where no precipitates have formed at all. These can also have a significant impact on the mechanical properties of the alloy.

2.4.1 Precipitates from age hardening in 6xxx grade alloys

In terms of strength contribution the precipitates are the most relevant particles, and their strengthening effect is related to their place in the precipitation sequence. These particles are only a few tens of nanometers in scale at the most, and they are the smallest of the particles found in 6xxx and 7xxx grade alloys. For an alloy in the 6xxx series the generic precipitation sequence for these particles is:

SSSS $\rightarrow$ GP zones $\rightarrow$ β" $\rightarrow$ β' $\rightarrow$ β

This simplified version of the sequence covers the most prominent and observable phases, with the GP zones and β" being the greatest strength contributors. The complete precipitation sequence is quite complex and consist of several more intermediate phases that can occur more separately or simultaneously as the precipitates listed in the simplified sequence. Saito et al. [14] investigated the precipitates in Al–Mg–Si alloys with low Cu contents (around 0,10 wt%) and found that prior to the formation of the GP zones, solute clusters form in the super saturated solid solution. They also observed that when aged past T6 the β' phase is accompanied by other structures, mainly U1, U2 and B'.

Saito et al. [15] further investigated the structures of the GP zones, intermediate phases and equilibrium phase for a 6082 grade alloy. The GP zones were found to be highly coherent needle shapes, around 2 x 2 x 20 nm with a primary monoclinic unit cell and a composition of $Mg_xAl_{5-x}Si_6$. The β" particles were needle shaped of around 4 x 4 x 50 nm and had a monoclinic C2/m unit cell, aligning along the $\langle 100 \rangle$ Al directions, and the composition Mg_5Si_6. They appeared fully coherent along the b-axis, and semi-coherent along the a- and c-axis.

The β' particles however were found to be rod shaped, several hundred nano meters long, and around 10 nm across. They consisted of hexagonal unit cells and appeared coherent

with the ⟨100⟩ directions of the aluminium matrix along the [001] direction. It had the composition of $Mg_{1.8}Si$ [15, 16] These β' particles, along with the coexisting U1, U2 and B', produces a coarse microstructure, causing the strength to decrease with their precipitation [16].

The equilibrium phase β, $Mg_{1.8}Si$, is the final phase of the precipitation sequence, and is fully non-coherent with the matrix. Saito et al. [15] found these unit cells have a CaF type FCC structure, and the particles form plates or cubes. Due to the lack of coherency between matrix and particles they do not inhibit dislocation glide making the alloy softer than when GP zones and β" are the dominating precipitates [8].

2.4.2 Precipitates from age hardening in 7xxx grade alloys

The case is similar for 7xxx grade alloys as to 6xxx grade alloys, with the actual precipitation sequence being quite complicated containing several intermediate faces occurring separately or simultaneously as the main precipitates. These are presented in the simplified precipitation sequence for the 7xxx grade alloys [6]:

SSSS $\rightarrow$ GP zones $\rightarrow \eta$' $\rightarrow \eta$

With this being a simplified sequence, Lervik et. al. [17] describes intermediate stages between η' and η referred to as $\eta_{(1-13)}$. In this article the specific phases η_1 and η_2 were mentioned as phases that would coexist with η' and η. For the alloy 7003 specifically they found that in water quenched (WQ) samples aged to T7, β' particles characteristic for alloys of the 6xxx series were also precipitated, likely due to the high silicone content of the alloy.

Following the state of supersaturated solid solution GP zones are formed. For the 7003 alloy Lervik et al. [18] also found that the GP zones favour a high Zn/Mg ratio. The unit is described as "a three-layered shell structure around an Al unit cell, which can take up an interstitial during build-up: an octahedron formed by the six side centres, a cube with Mg on the eight corners and the immediate truncated cube octahedral shell with 24 atomic positions" [18]. Figure 2.7 shows an illustration of the structure of the cluster unit cell. Each unit is stacked according to the principals [002], ⟨411⟩ and ⟨330⟩, and the GP zones have either four units connecting into a ⟨411⟩ square or three units with one ⟨330⟩ connection and two ⟨411⟩ connections. The latter being less favorable due to the high pressure. These configurations generally gives the GP zones the chemical formula of Mg_8Zn_{25} and Mg_8Zn_{31} respectively. Both these configurations are coherent with the matrix [18].

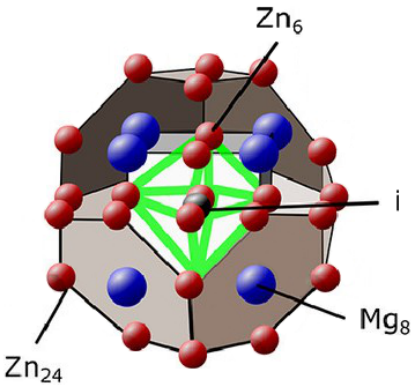

Figure 2.7: The single cluster unit, a 3-shell truncated cube with a octahedron structure, of a GP zone in a 7xxx aluminium alloy [18].

The hardening phase of 7003 alloy, η', consist of plate shaped particles on the {111} Al planes. These plates are built up of orthorhombic sub units, and are semi-coherent with the matrix [19]. As the aging process continues the material will coarsen and the volume fraction of η' decrease, leading to the creation of η particles, the equilibrium phase. These particles have plate like shapes with hexagonal unit cells, and are completely non-coherent [17]. Zhang et al. [20] investigated the effect of cooling rates on 7150 and 7055 grade alloys after solutionizing prior to aging, and found that it had an impact on both the volume fraction and size of the η' precipitates. Higher cooling rates led to higher volume fractions of η' where the precipitates were smaller in comparison to at lower cooling rates, which led to a coarsening with a lower volume fraction of larger η' precipitates.

2.4.3 Precipitation free zones

Precipitation free zones (PFZs) are areas where no particles have precipitated. As mentioned in Chapter 2.3, vacancies are the most important nucleation sites for heterogeneous precipitation of particles, and in order for nucleation to take place a critical vacancy supersaturation is needed. A PFZ is often formed on each side of a grain boundary and Figure 2.8 shows a simplified illustration of such a zone. This is either because of vacancies diffusing into the grain boundary where they are absorbed leaving the vacancy saturation in the surrounding area lower than the critical supersaturation, or because precipitates form on the grain boundaries leaving the solute concentration in the surrounding area to low for precipitates to form. The width of the PFZ is dependent on the solutionizing temperature, quenching rate and aging temperature. At higher solutionizing temperatures more vacancies are formed, and the higher the quenching rate the less time vacancies have to diffuse into the grain boundaries. If the quenching rate is lower the vacancies have more time at higher temperatures to diffuse and disintegrate into the grain boundaries. At lower aging temperatures the nucleation rate is higher making the critical vacancy supersaturation lower and precipitation is then possible closer to the grain boundary [21].

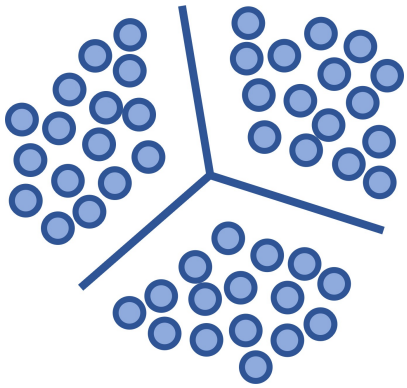

Figure 2.8: Precipitation free zone around a grain boundary.

Fourmeau et al. [22] investigated the geometry and chemical composition of PFZs in a 7075-T651 and found that high angle grain boundaries were surrounded by PFZs around 40 nm wide. They were also found around low angle (sub) grain boundaries with a width of about 20 nm. In both cases grain boundary precipitates were observed. Figure 2.9 show a bright field TEM image of the PFZs around a high and low angle grain boundary. The PFZs contained less zinc, magnesium and copper compared to the bulk material, but still had some alloying elements in solid solution.

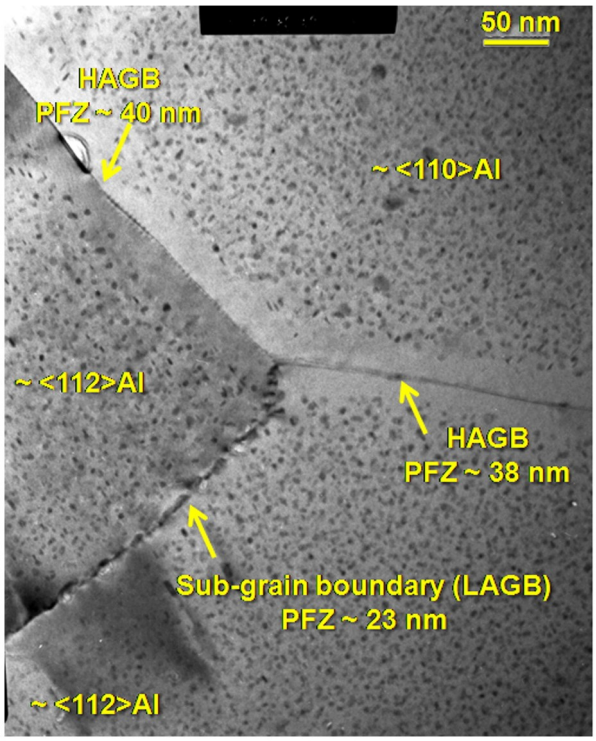

Figure 2.9: A brigth field TEM image showing the width of the PFZs found around two high angle grain boundaries and a low angle grain boundary [22].

This was however the case of an artificially aged alloy, where PLZ is more likely to occur. More relevant in terms of natural ageing is the research of Mansouri et al. [23] on PLZs

in naturally aged Al-0.71Mg-0.95Si-0.25Mn-0.2Fe alloys. They investigated two different cases, one where the specimens were air cooled (3°C/s) after solutionizing, prior to natural aging, and one where they were water quenched (less than 2000°C/s). Using TEM imaging they found grain boundary precipitates in the air cooled specimens, but not in the water quenched ones. They did not explicitly observe the PFZs, but suspected their existence due to the grain boundary precipitates found in the air cooled sample. This indicated there must have been a low vacancy saturation in the surrounding areas leading to PFZ during aging. Further testing reviled a strain localization in regions near the grain boundaries for both specimen types that was around 20 times greater than the far field strain for the air cooled specimen and 5 times for the water quenched. They proposed PFZs being the cause.

2.4.4 Dispersoids and constituent particles

Dispersoids are formed during homogenizing of cast aluminium billets as a result of additional alloying elements meant to promote these particles. The particles are generally larger than the particles precipitated during aging, varying from between 10 to 200 nm in scale. As these particles occur as a result of solid-solid reaction from heating the billet they are often at least semi-coherent with the matrix due to their solid-solid transformation. Their strength contribution is however less than for the precipitated particles as they are fewer with a larger mean distance between them, instead they prevent or limit recrystallization. For the alloy 6013 the chemical composition of the dispersoids are $Al_{12}Mn_3Si$. For the alloys 7X50 and 7055 which are alloyed with zirconium in order to promote dispersoids, the dispersoids have the chemical composition of Al_3Zr. Al_3Zr is fully coherent with the matrix as it precipitates into a metastable $L1_2$ structure with similar lattice parameters to those of the aluminium matrix. These particles are also resitsant to coarsening unless the alloy is heated above their solvus temperature [6].

Constituent particles form during the solidification of the aluminium and are the result of a liquid-solid phase transition. They are mainly cast by iron impurities in the alloy, but silicone can also cause the formation of constituent particles, often in combination with iron. These particles are large and inchoherent and range between 1 to 30 µm in size, and their size is mainly determined by solidification rate, iron or silicone content and amount of deformation. These intermetallic particles are brittle and often insoluble or sparsely soluble due to their high melting point [6].

2.5 Deformation mechanisms for aluminium

Metals are crystalline materials, meaning they are built up of repeating structures that make up the entire material. The smallest repeating structure is the unit cell, and its form varies based on the type of metal or alloy. There are seven different unit cell structures, and a total of 14 different variations of atom placement in these cells. The unit cell of aluminium and aluminium alloys has a face centered cubic (FCC) structure which, together with HCP, is a close packed structures. These structures have the most densely packed crystal planes when stacked. However, the structure of metals is never perfect and will suffer from defects such as plane defects which includes grain boundaries in poly crystalline materials, line defects like dislocations and point defects like vacancies. Dislocation movement is the cause of plastic deformation in metals and is related to the crystal structure of the material. Primarily there are two types of dislocations, edge dislocations and screw dislocations [24].

2.5.1 Dislocations

An edge dislocation is a half plane of atoms inserted into the crystal structure. This extra lattice plane presents a line defect where the edge of the plane meets the structure below. The Burgers vector is represents the direction and magnitude of the lattice distortion caused by the dislocation, and a visual representation of it for an edge dislocation is shown in Figure 2.10. The Burgers vector shows the direction of the dislocation movement and for edge dislocations the Burgers vector is normal to the dislocation line. Screw dislocations are somewhat harder to visualize, but distinguishes themselves from the edge dislocations by their Burgers vector being parallel to the dislocation line. Mixed dislocations is the general case, where parts of the dislocation segment might be neither pure edge or pure screw. This usually occurs in dislocations that contains segments of both edge and screw character, where the sections in between become mixed and the dislocation line is between normal and parallel to the Burgers vector, as Figure 2.11 shows [24].

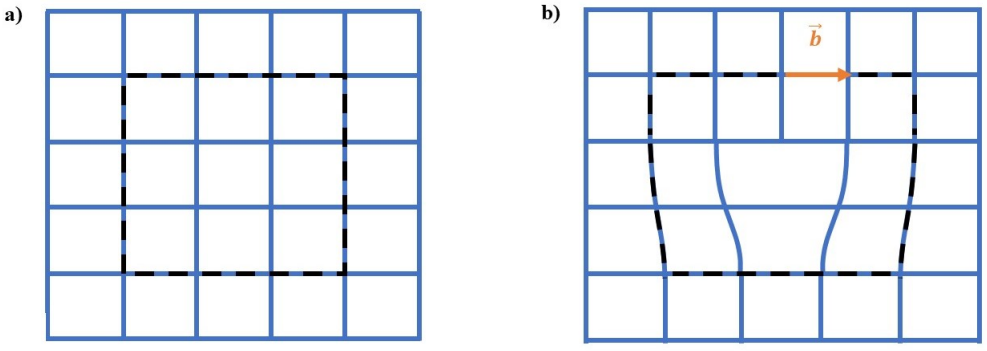

Figure 2.10: a) shows the Burgers circuit in a perfect lattice, and b) shows the Burgers circuit with an inserted dislocation segment, where the gap corresponds to the Burgers vector.

A metal is deformed plastically through the sliding of crystal planes relative to each other causing a relative displacement of atoms by one $\vec{b}$ above compared to the glide plane below, without changing the crystal lattice. This is called slip, and occur mainly through dislocation glide along slip systems. Slip systems consist of a slip plane and a slip direction and for FCC crystals dislocations glide along the $\{111\}$ planes in the $\langle 110 \rangle$ directions, resulting in a total of 12 slip systems. These are the most densely packed planes and directions in the unit cell. With edge dislocations the glide plane is determined by the Burgers vector and the dislocation line, $\vec{t}$, which are normal to each other. Glide occurs in the direction of the Burgers vector. For screw dislocations the Burgers vector and dislocation line is parallel, allowing glide along several glide planes with the direction of glide being normal to the Burgers vector. Figure 2.11 show the relationship between the Burgers vector and the dislocation line for edge, screw and mixed dislocations [24].

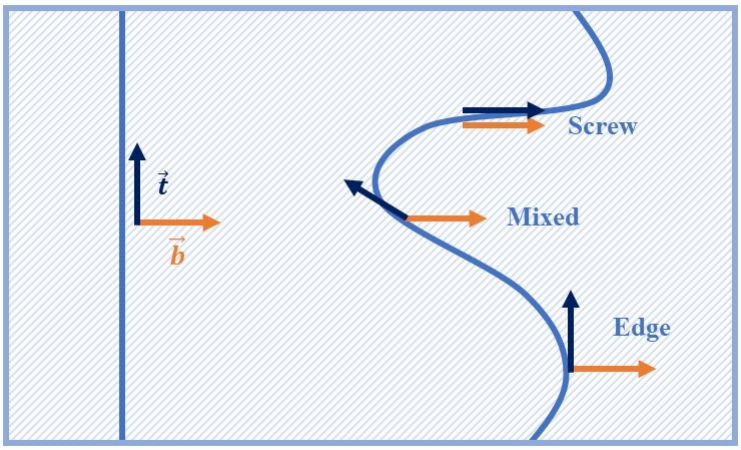

Figure 2.11: A dislocation gliding in its glide plane at different speeds throughout the segment, leading to areas with screw, edge and mixed character.

2.5.2 Conservative and non-conservative dislocation movements

When a dislocation glides it will move with a speed varying throughout the segment, and interact with other planes and dislocations. This means it does not glide as a constant, unaffected segment. As some parts of the segment glides faster than others this results in a curved dislocation with different areas of the dislocation having different characteristics such as edge, screw or mixed. Up close these curves consists of small kinks in the dislocation, which are small, atom sized steps in the glide plane. Dislocations or segments with a pure screw characteristic can cross glide, which involves the pure screw changing glide plane. This is possible as the Burgers vector and the dislocation line vector are parallel and therefore do not define a glide plane. Since the glide plane of an edge dislocation is defined by these two vectors cross glide is not possible [24].

Movement of dislocations are not only limited to glide, but can also happen through

climb. While dislocation glide is a conservative movement that requires smaller stresses to be activated, climb is a non-conservative movement that does not conserve the number of atoms in the dislocation as it climbs. It requires an exchange of vacancies in order for the dislocation to climb normal to its current plane, and is therefore more common at higher temperatures as this is diffusion controlled. Climb is also only possible for edge dislocations as it happens along the dislocation line. During climb a row of atoms will diffuse to or from the dislocation line, leaving behind a row of vacancies and the dislocation line one atom longer or shorter [24].

Jogs in a dislocation segment can also occur, and these are small atom sized steps out of the glide plane. A jog in a screw dislocation will move along the dislocation segment with a similar mechanism to dislocation climb. Jogs in screw dislocations do not lay in the dislocation glide planes, meaning that in order for the dislocation to glide the jog will have to climb resulting in it leaving behind vacancies. However, compared to climb, thermal activation is not necessarily needed as it can move under high enough stresses [24].

2.6 Extrusion of aluminium

Extrusion is a common forming process used on metals to create profiles with a variety of different sizes and cross section geometries. It involves pushing a larger metal billet through a smaller die orifice with the shape of the wanted cross section, resulting in a longer profile with the same cross section throughout its length. The equipment used to extrude the metal primarily consists of a container that holds the billet in place, a die in one end of the container, with a cross section and size of the wanted geometry to extrude the metal through, and a ram at the other end to apply the compressive forces. The resulting quality of the extruded profile depends on the cross section reduction the angle of the die, speed, temperature and friction [25, 5].

Due to the relatively high yield point of most metals extrusion is done at elevated temperatures as this lowers the yield point, lessening the force required to extrude the metal. Aluminium and aluminium alloys are extruded at temperatures between 400-500°C and often at a higher speed of deformation. This generates heat in the deformation area further increasing the temperature and metal flow there. The friction between the billet and the container greatly affects the metal flow through the die. High friction results in a greater velocity deviation between the metal flow in the center of the billet compared to the outside, as illustrated in Figure 2.12. This increases the risk of both internal defects and surface defects. To minimize the friction the sides of the container is well lubricated and the speed adapted accordingly [25, 26].

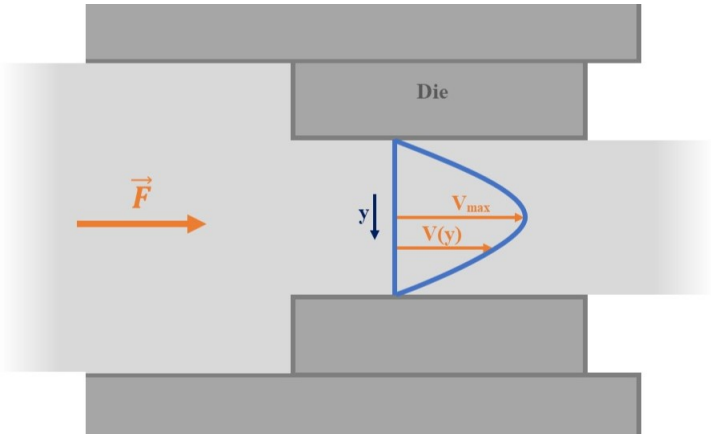

Figure 2.12: The velocity gradient in the profile as it passes through the die.

During extrusion the material deforms greatly, and the macroscopic deformation caused by the process is reflected in the microstructure. As the billet increases in length and decreases in cross section area the grains in extruded profiles are often elongated along the extrusion direction. The geometry of the cross section of the grains somewhat depends on the cross section geometry of the extruded profile. In the case of an axis symmetric profile the grains themselves will be mostly axis symmetric with a more equal diameter between the transverse directions. For flat extruded profiles the grains will have a flatter and

wider cross section. However for both axis symmetric extrusions and flat extruded profiles the grain shape might vary throughout the profile. Closer to the surface the grains can be flatter compared to in the center of the profile, as they have experienced a somewhat different flow due to the friction between the metal and the container resulting in a velocity deviation, and more uneven compression. This is more evident in axis symmetric profiles and thicker flat extruded profiles [27, 26].

Extrusion is one of several processing steps the aluminium goes through before achieving the final product. The metal is first cast into billets, cooled, and then homogenized in order to recrystallize the material, and for some alloys promote the formation of dispersoids. Later the billets can be extruded to reach the wanted shape. As the extrusion happens at higher temperatures the extruded profile can either be quenched right out of the die, combining the hot extrusion process and solid solution heat treatment, or it can be cooled more slowly and then solution heat treated at a later time. Finally the product can be heat treated to the wanted level of strength or hardens. Figure 2.13 shows a simplified version of the temperature profile for the processing steps.

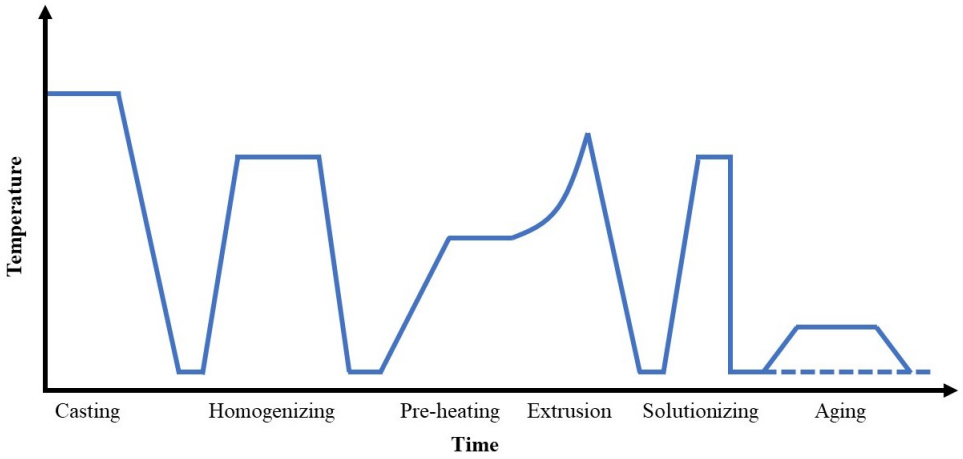

Figure 2.13: The processing steps from casting to age hardened aluminium product.

With constituent particles being precipitated prior to extrusion these are often also affected by the forming process. Ii et al. [28] investigated the effect of extrusion on the constituent particles in an Al-10Zn-2.5Mg-2.5Cu alloy and determined that the two main types of iron rich intermetallic particles found behaved similarly when the material was extruded, with them either braking and aligning themselves with the extrusion direction or aligning themselves with the extrusion direction without much breakage. Figure 2.14 show the placement of the particles after homogenization and after extrusion. The images show the two different constituents marked with arrows labeled a and b, and depict how the particles marked b mostly maintained their size while particles marked a broke apart. The larger, unbroken particles in the extruded material are around 2-3 µm wide and a little over 10 µm long according to the figure. Both are aligned in the extrusion direction.

However, as this report is not investigating 7xxx grade alloys containing large amounts

copper, Liao et al. [29] has discussed what effect the addition of copper had on a hot rolled Al-8Zn-1,6Mg-0,4Zr-0,03Fe alloy. The copper content was increased to 0,77 wt% and 1,64 wt%. He observed that the added copper resulted in an increase in the volume fraction of constituent particles and precipitated particles, but had little effect on the particle sizes.

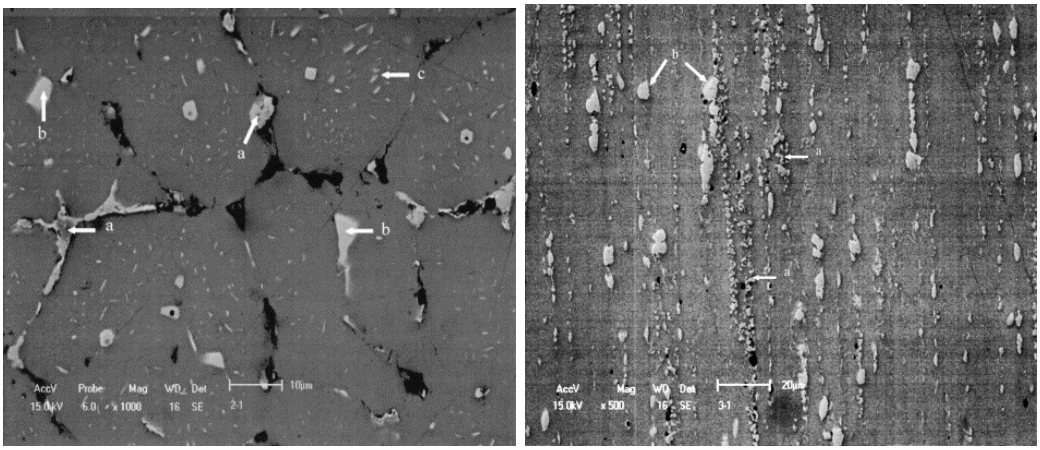

Figure 2.14: The distribution of type a and type b constituent particles after to homogenization, left image, and extrusion, right image [28].

2.7 Aluminium and texture

With poly crystalline metals each grain has a distinct crystallographic orientation, and different forming processes and heat treatments will affect these orientations. The texture of a metal is a measure of the distribution of crystallographic orientations in it, and is dependent on both material and processing. Metal products that have a weak texture have grains with seemingly random crystal orientations, with most orientations represented and repeated throughout the material. Metal products with a strong texture have a few select crystal orientations repeated throughout the material. Texture is the main cause of mechanical anisotropy. Changes in the texture can be caused by plastic deformation or an exposure to higher temperatures over longer periods of time [30]. If a single crystal is plastically deformed it will rotate in order to activate more slip systems. When a polycrystalline material is deformed in rolling, extrusion, forging or other forming processes the randomly oriented grains will experience slip on their activated slip systems and rotate from their initial position relative to the direction of the applied stresses, and under the constraint from neighbouring grains [24].

2.7.1 Pole figures

Pole figures are used to depict the distribution of orientations. These are stereographic projections of crystal planes onto a reference coordinate system. For extrusion there are two common reference systems. The first system consists of the extrusion direction (ED), a transverse direction (TD) and a normal direction (ND), as shown in Figure 2.15 a), and is often used for profiles that are flat or otherwise not axis-symmetric. The second system can be used for profiles that are axis-symmetric, and has the extrusion direction as normal direction and then two transverse directions (TD_1 and TD_2), as shown in Figure 2.15 b) [30].

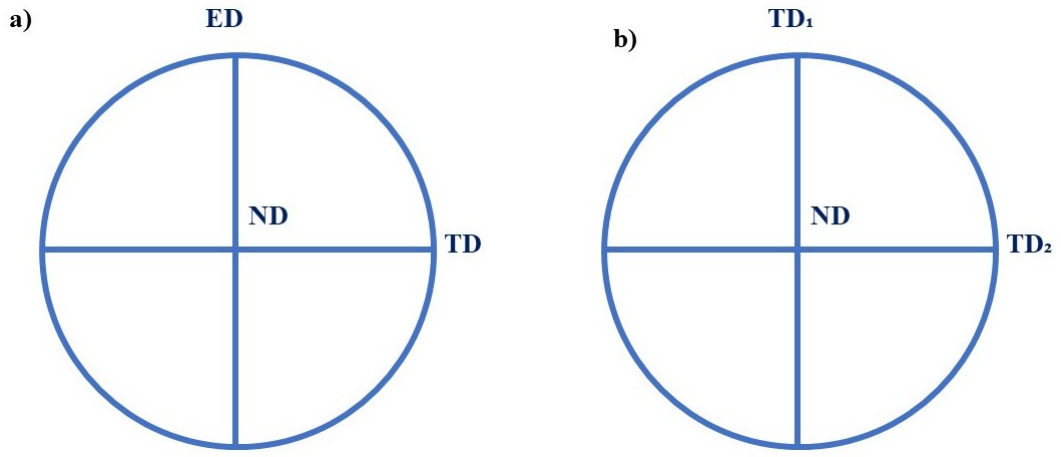

Figure 2.15: The reference systems for extruded profiles.

The pole figures of a material show a distribution of patterns where the reflecting planes

intersect with the reference system. It is created by considering the reference plane as the equator plane of a sphere. The orientation of a unit cell from each grain is then considered compared to this system by "placing" it at the cross section of the three axis. A line normal to the planes in question is drawn out until they reach the edge of the sphere. Then these points are connected to the focus point at the bottom of the sphere with another line, and the points where these lines intersect with the reference plane is the cell's stereographic projection. Figure 2.16 illustrates this configuration using the reference system from Figure 2.15 a). When several grains are tested the pole figure will show the overall distribution of the given plane, and when there is a clear texture there will be a clear pattern projected.

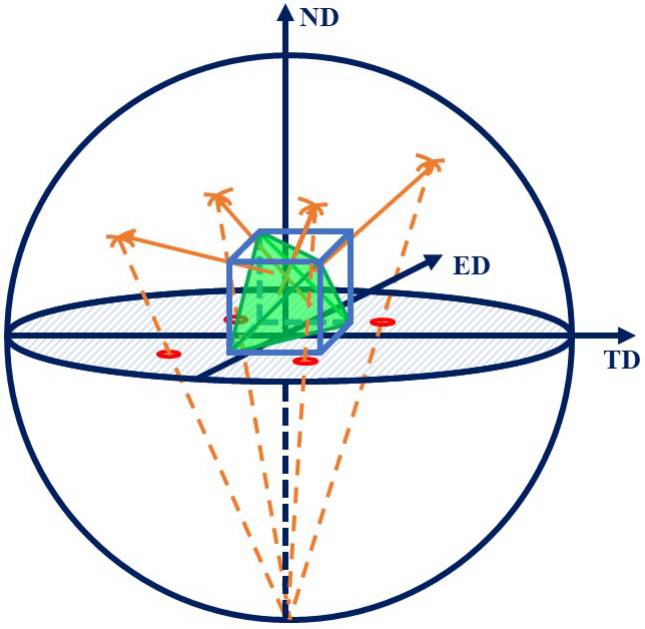

Figure 2.16: A demonstration of how the stereographic projection of the 111-planes in an FCC crystal is created in the reference system using ED, TD and ND.

A description of the texture is given in the form of texture components. For rolling or extrusion of flat profiles, which result in similar textures, the texture component is defined by rolling plane and rolling direction. Different texture components can be visualized and compared by using the same reference planes, for example 111-planes, as the reflecting planes and see what projections they give. This is then a 111 pole figure showing these two textures. For axis-symmetric extrusion the texture component consists of only fiber direction. The pole figures of different fiber directions can also be compared by using the same reflecting plane as reference. Knowing the reflections a plane can create depending on the texture components make it possible to recognize the texture components of a material from a measured pole figure [30].

2.7.2 The texture of flat extruded aluminium profiles and axis- symmetric profiles

As texture is dependant on both the metal or alloy, forming processes and heat treatments a variety of different textures can be promoted. Some are often more wanted then others as texture is strongly related to mechanical properties and anisotropy, meaning it is often taken into consideration when choosing processing steps and parameters. Forming processes like rolling or extrusion of flat profiles and axis-symmetric extrusion often induce a strong texture because the grains will rotate to more stable orientations. For aluminium, which has an FCC structure, common texture components after rolling or extrusion of flat profiles are S, $\{123\}\langle 41\bar{2}\rangle$, Cu, $\{112\}\langle 11\bar{1}\rangle$ and Brass, $\{110\}\langle 1\bar{1}2\rangle$. Figure 2.17 show an illustration of the projections of these components in a 111 and 001 pole figure. With axis-symmetric extrusion aluminium tend to develop $\langle 111\rangle$ and $\langle 001\rangle$ fibres [8, 30]. Figure 2.18 show an illustration of the projections of these fibres in a 111 and 001 pole figure. In some cases a shear texture might occur in areas were the material experience shear stresses during forming. The shear texture is somewhat more complicated in terms of texture components, but Figure 2.19 show an illustration of a typical 111 pole figure for an FCC material were these texture components are projected [31].

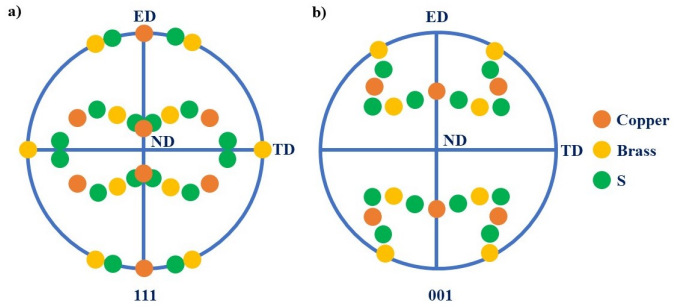

Figure 2.17: The a) 111 and b) 001 pole figures of the S, Cu and Brass texture components in a ED-TD reference system.

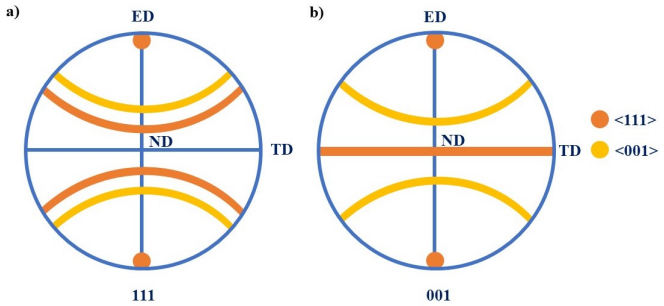

Figure 2.18: The a) 111 and b) 001 pole figures of the $\langle 111\rangle$ and $\langle 001\rangle$ fibres in a ED-TD reference system.

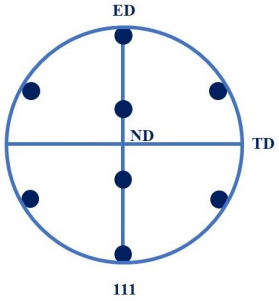

Figure 2.19: The 111 pole figure showing the projected shear texture.

As a single FCC crystal does not have equal mechanical properties in all directions, an uneven distribution of crystal orientation in a material will make it anisotropic. Anisotropy in metals mean that some properties will vary based on directions, like mechanical properties. For a sheet of aluminium with a strong texture a tensile sample cut along the extrusion direction will not have the same yield strength as one cut 45° to the extrusion direction. With polycrystalline materials this anisotropy is mostly caused by texture, but is also affected by lattice defects, precipitated particles from casting or aging and the formation of shear bands. The r-value is used to describe the level of anisotropy in a material, and is the ratio between the plastic strain in the width and the plastic strain in the thickness of a tensile sample after a tensile test. The equation for r-value is given in Equation 2.8 [8].

$$r = \frac{\epsilon_w}{\epsilon_t} = \frac{ln\frac{w}{w_0}}{ln\frac{t}{t_0}} \tag{2.8}$$

Where ϵ_w is the plastic strain in the width direction, ϵ_t is the plastic strain in the thickness direction, w and t is the width and thickness of the specimen close to the fracture and w_0 and t_0 is the width and thickness before testing. In order to determine if the material is isotropic or not tensile samples are cut in different angles to the extrusion or rolling direction of the flat profile, and then a tensile test is performed on them. If r=1 in all the samples the plastic strain of the width and thickness is the same and the material is isotropic. The r-value both describes weather or not the sample is anisotropic, and indicates to what degree [8].

2.7.3 EBSD as a method for identifying and mapping texture

EBSD, electron backscatter diffraction, is used to map out texture by scanning and indexing the crystal orientation in each grain in a poly crystalline material. The analysis is done in a SEM with the required detectors, where an EDSP, electron backscatter pattern, is created for each grain and then put together in a program to create the complete EBSD image. In the SEM the sample is rotated 60-80° to get a high impact angle of the electron beam. Some of the primary electrons that are fired at the sample will backscatter at a high

angle, and are diffracted as they exit the sample. This diffraction pattern is depicted as several bands crossing each other, called a Kikuchi pattern, where the band intersections correspond to where Braggs law has been fulfilled and represents specific crystallographic directions. These can be used to determine the crystal orientation of the grain [32].

When several EDSPs are put together they make up an EBSD image. It can be visualized as a pole figure showing all the texture components with respect to a reference plane, or an IPF, inverse pole figure, map that gives information about the near surface texture, orientation relationships between grains or phase boundaries, sub grains, grain size and shape, among other things [32]. The data from the EDSPs can be processed on-line or off-line. When processed off-line the data is downloaded and used in a separate program where the pole figures and IPF images are created.

2.8 Uniaxial tensile testing and properties of aluminium alloys

Tensile testing is the most commonly used methods to evaluate materials. Uniaxial tensile testing is the simplest test form, and involves gripping each side of a specimen and applying a tensile force to elongate the sample at a constant rate, until it eventually fractures [33].

2.8.1 Stress and strain

The force-extension data from this test is translated into a stress-strain curve. These curves provide useful and comparable data about how the material behaves under the increasing load and constant strain rate. A typical stress-strain curve for a metal with some of the more notable characteristics noted, is shown in Figure 2.20. The stress, along the y-axis of the diagram, is derived from the force. Most commonly the engineering stress, also called nominal stress, s, is used. It is calculated using Equation 2.9 [33]:

$$S = \frac{F}{A_0} \tag{2.9}$$

Where F is the force applied at a given time and A_0 is the cross section area of the specimen before testing. The stress is usually given in Mega Pascal. Throughout the curve the force factor in the stress will vary while the initial cross section area is a constant, meaning this stress calculation does not take into consideration that in practicality the cross section area decreases as the length increases. True stress however, takes into consideration the change in area and uses an instant value, A, rather than a constant, A_0. The result is that the true stress is often higher than the nominal stress, and the relationship between nominal and true stress is given as [33]:

$$\sigma = s(1 + e) \tag{2.10}$$

Where s is the nominal stress and e is the nominal strain. The strain is derived from the elongation of the sample and shown as the x-axis on the stress-strain curve. Nominal strain is the elongation of the sample relative to its original length, as shown in Equation 2.11 [33]:

$$e = \frac{l - l_0}{l_0} \tag{2.11}$$

Where l is the current length of the sample and l_0 is the initial length of the sample. The nominal strain, however, only takes into account the total elongation as compared to the initial length. The true strain represents the change in length as compared to the previous length. True strain is related to the nominal strain, and Equation 2.12 shows the relationship [33]:

$$\epsilon = ln(\frac{l}{l_0}) = ln(1 + e) \tag{2.12}$$

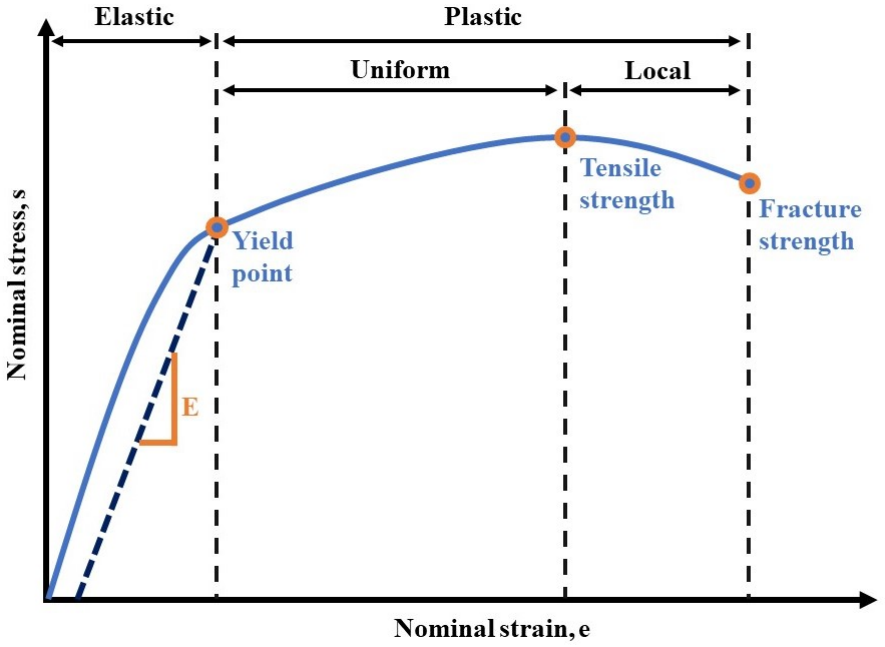

Figure 2.20: An exemplified version of a stress-strain curve for a metal showing the different regions of the curve and the yield point, tensile strength and fracture strength.

2.8.2 Characteristics of the stress-strain curve

A number of material characteristics can be observed from the stress-strain curve. The nominal stress-strain curve seen in Figure 2.20 is considered. The first region in the stress-strain curve is the elastic region, which is the linear area. Here no permanent elongation occur and if the specimen is unloaded it will go back to its initial length. Therefore there is no slip in this region as this causes permanent deformation, rather the crystal lattices are being stretched in the direction of the applied tensile force. The elastic modulus (E), or Young's modulus, is the slope of the elastic region and essentially represents the spring constant of a material [33, 24].

As the specimen is stretched further the material moves out of the elastic region and into the plastic region. The deformations that occur here are permanent as a result of slip, and the specimen will not recover its original shape when the stress is removed. For a nominal stress-strain curve of a metal this region traditionally contain a yield point, an ultimate tensile stress and a fracture stress. The yield point is between the elastic and plastic region where the stress has just become high enough to activate slip in the crystal lattices, leading to dislocation glide and permanent deformation. The point of this change is more obvious in some materials than others, and often the yield point is determined by drawing a line parallel to the elastic modulus from 0.002 strain on the x-axis until it crosses the curve. This intersection is referred to as the offset yield strength, $R_{p0.2}$ [33, 24].

The plastic region of the curve is further divided into a region of uniform deformation and a region of local deformation, where necking or plastic instability occur. During uniform deformation the specimen deforms evenly along the gauge section until the ultimate tensile strength is reached. The ultimate tensile stress essentially represents the stress at the onset of necking. Following the offset yield strength the material is work hardening causing the stress needed to deform the material to increase. Simultaneously the cross section area is decreasing and the force required to stretch the specimen is decreasing. Initially the slope climbs as the work hardening effect is greater than the effect of the cross section reduction, but as the sample is stretched the work hardening decreases and the reduction of the cross section area increase. Eventually the slope peaks at the ultimate tensile strength before necking is initiated. The onset of necking, or diffuse necking to be specific, is described by the Considere criterion. For a nominal stress-strain curve the onset of necking occur at [24, 34]:

$$\frac{dF}{dL} = \frac{ds}{de} = 0 \tag{2.13}$$

Where F is the applied force, L is the increase in length, s is nominal stress and e is nominal strain. Equation 2.13 in practise describes the top point or the point of maximum stress in the nominal stress-strain curve. The neck initiated here is a local area on the specimen where the reduction in cross section area will continue to happen until fracture, as illustrated in Figure 2.21 a). For ductile metals the ultimate tensile strength corresponds to the point where necking begins. However, for brittle metals necking do not occur and the fracture strength will be either the same as the ultimate tensile strength or the yield strength depending on if the metal deforms uniformly prior to fracture or not [24, 34].

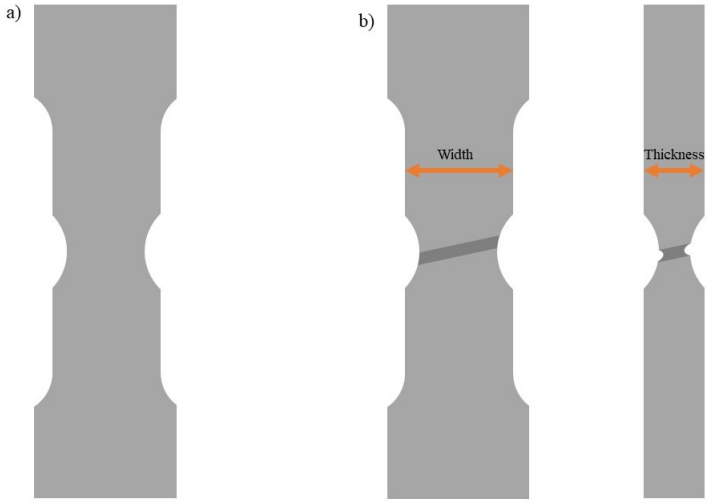

Figure 2.21: An illustration of a) a diffuse neck in a tensile specimen and b) a local neck in a tensile specimen.

During tensile testing some metals with sample geometries with relatively high width to thickness ratios can experience localized necking. Localized necking is related to anisotropy and r-value, discussed in Chapter 2.7. Here a neck develops within the diffuse neck where the specimen only gets thinner, but the width is unchanged as Figure 2.21 b) illustrates. The local neck is not 90° to the tensile axis, but occur at an angle θ, as Figure 2.22 depicts. This angle is related to the r-value of the of the material and the relationship is given in Equation 2.14 [34]:

$$tan\theta = \sqrt{\frac{r+1}{r}} \tag{2.14}$$

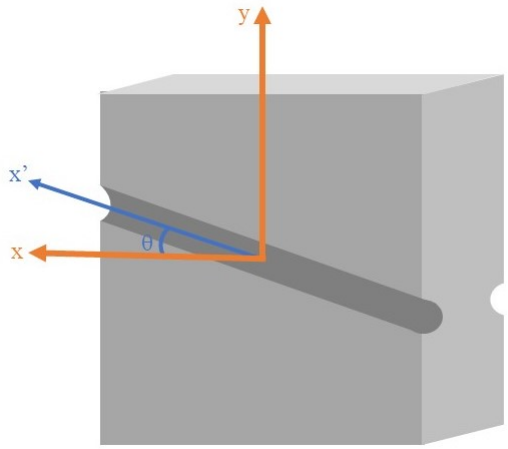

Figure 2.22: An illustration of the angle θ in a local neck.

The region of uniform stress and strain in a specimen ends at the ultimate tensile strength where necking is initiated. With 6xxx and 7xxx grade aluminium alloys the uniform strain and ultimate tensile strength achieved will vary depending on composition, previous forming processes and heat treatments. For a 6082 alloy aged to T6 Ryen et al. [35] found that the uniform strain was 0,059 mm/mm when the tensile test was performed at room temperature, and the ultimate tensile strength was 339,5 MPa. In the case of 7003 alloys aged to T6 Shah et al. [36] found that the uniform strain was approximately 0,09 mm/mm when the tensile test was performed at room temperature, and the ultimate tensile strength was around 400 MPa.

2.8.3 Strain aging

Under some circumstances usually ductile materials might experience plastic flow instabilities that can lead to early fracture without much local deformation. Strain aging is one such phenomena and is related to the hardening effect of solute atoms in the metal. For an alloy with available solute atoms, for example a wrought aluminium alloy in solid solution, the solute atoms will diffuse towards dislocations as this lowers the elastic energy of both their impact on the surrounding structure. This restricts the movement of the dislocation and is referred to as dislocation pinning by solutes. results in a concentration difference between the matrix and the area surrounding the dislocations. The concentration C around the dislocation is higher than the concentration, C_0, in the matrix. These clusters of solute atoms that form around the dislocations are called Cottrell spheres, and they are responsible for strain aging [37, 38].

The effect of strain aging can be observed during some mechanical tests, and can be both recognized from the test data and in some cases the sample. When a mobile dislocation is surrounded by the solute atoms a certain stress is required for it to move through and past the sphere. This stress is higher than the stress required to activate glide without solute

atoms present. When this new critical stress is reached it moves out of this concentration C and into the concentration C_0 of the matrix. The stress required to move through the matrix is lower compared to moving past the sphere. In a uni-axial tensile test using a constant strain rate this will show as a drop in the stress on the curve as the force required to elongate the sample suddenly drops. Strain aging can be both static and dynamic. The mechanism is the same for both cases, but they differ in whether the effect occur once before returning to "normal" plastic deformation or is repeated [39].

Static strain aging affects the yield point of the material and is for some metals and alloys observable in the elastic to plastic transition on a stress-strain curve. Plastic deformation is initiated as the applied stress becomes high enough for the dislocations to glide past the Cottrell spheres. As these dislocations move into the matrix which has a lot lower concentration of solute atoms the stress drops drastically, and this is observable in the stress-strain curve. However, the plastic deformation now occurring is not happening uniformly over the entire sample. Instead a thin band called a Portevin–Le Chatelier (PLC) band is formed. Only the dislocations in this region are gliding free of the Cottrell spheres. In the remaining part of the specimen the dislocations are still surrounded by the spheres, experiencing only elastic deformation [39, 38]. The PLC band also has a different strain rate as to compared to the rest of the specimen, and as the deformation continues the band is work hardened. On the stress-strain curve this is shown as a tiny increase in stress. Robinson et al. [40] found that in a 5182 grade alloy PLC bands tended to form at an angle of around 60° to the tensile axis [40].

At one point the stress required to further work harden the PLC band is equal to the stress required to move the dislocations of a new section out of their Cottrell spheres, and so the band expands. On the stress-strain curve this is again seen as a small drop in stress. As the strain increases the spread of the band continues until the entire specimen is covered and deformation is uniform, as seen in Figure 2.23, resulting in a serrated section of the stress-strain curve in the area of the yield point. Afterwards uniform plastic deformation follows as the stress required to deform the sample increases again as for a regular stress-strain curve. Here the dislocations are free to move outside the spheres. If the sample is unloaded during the plastic deformation after having experienced static strain aging and left for some time, the solute atoms will diffuse towards the dislocation again creating new Cottrell spheres that will cause dynamic strain if the test is restarted [39].

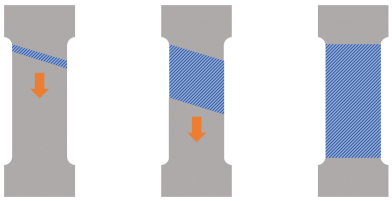

Figure 2.23: An illustration of the spread of a PLC band in a sample [40].

Dynamic strain aging differs from static strain aging in that it affects the entire plastic region of the stress-strain curve rather than just the transition between the plastic and elastic region. It is easily recognisable in a uniaxial tensile test as it leaves the entire curve serrated, and is due to new PLC bands forming rather than uniform deformation continuing after the first band has spread over the entire specimen. PLC bands are formed anew because the solute atoms diffuse back to the dislocations after they have moved into the matrix, forming new Cottrell spheres that the dislocations again need a higher stress to move past. As diffusion is both temperature and time dependent dynamic strain aging can occur in some materials at high temperatures or at low strain rates, as the solute atoms are able to diffuse after the dislocations as they glide, either due to an increased diffusion rate from the higher temperature or due to the atoms having enough time to diffuse after the dislocations as a result of the low strain rate, causing the dislocations to constantly move in and out of a concentration C. This continuous process of reoccurring PLC bands means the stress required to maintain a constant strain rate to vary, resulting in a serrated stress-strain curve [39].

As the mobile dislocations glide past the Cottrell spheres the strain rate changes, causing the strain rate sensitivity to be negative, as seen in from the N-shaped curve in Figure 2.24. The initial increase in stress corresponds to to the dislocation moving through concentration C, but at a certain strain the dislocations will move into a concentration C_0. The following curve corresponds to the stress required to deform the metal when the dislocations glide through the matrix, less affected by the high solute atom concentrations [39]. Regarding dynamic strain aging it is often not present during the entire tensile test, but occur at a critical strain [41]

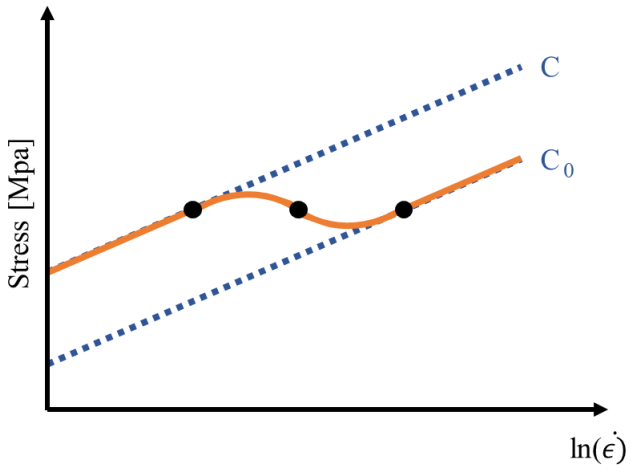

Figure 2.24: The N-shape of a curve as a result from changing strain rates.

As strain aging is the result of solute atoms in the matrix interfering with dislocations an increase in the solute content also increases the chance of strain aging occurring [38].

Zhiheng et al. [42] found that in Al-Cu alloys a high solute concentration and high dislocation density resulted in dynamic strain aging by conducting tensile tests at specimens in different stages of the aging process. They also found that these alloys did not experience strain aging when in a state of SSSS, assumingly because of the low dislocation density [42]. Some aluminium alloys can experience strain aging under certain conditions. Both Al-Si and Al-Mg alloys are susceptible to dynamic strain aging at room temperature for certain strain rates. Zhao et al. [43] confirmed that even low weight percentages of silicon in aluminium can cause dynamic strain aging in the material during uniaxial tensile testing, and additionally Xu et al. [41] found that dynamic strain aging can also affect Al-Mg alloys at room temperature at certain strain rates as shown in Figure 2.25. According to this figure the samples with the highest and lowest strain rates experienced less of the dynamic strain aging effect, while the samples stretched with the strain rates in between have more serrated curves due to dynamic strain aging [41].

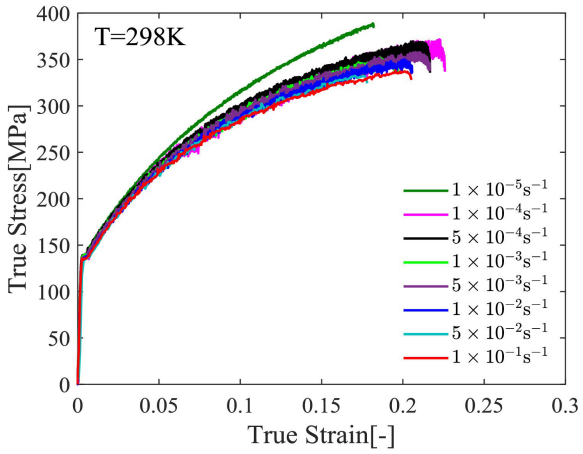

Figure 2.25: The true stress-strain curves of an Al-Mg alloy at 298 K for different strain rates [41].

2.8.4 Strain path change

Another type of plastic flow instability experienced by some usually ductile materials are strain path changes. This entails the direction of the strain in the specimen changing from the tensile direction to another direction during a tensile test. A specific example is a path change to the direction of the shear stress, 45°on the tensile axis. This plastic flow instability occur locally and result in a shear band forming. When such a strain path changes is recreated using various tensile test methods the strain path will in most cases lead to an increase in flow stress followed by a reduction in the strain hardening rate, compared to the equivalent amount of straining in proportional deformation [44]. However, in some special cases a softening occur and the material i weaker following an induced strain path change [44, 45].

2.9 Fracture

When a material is exposed to a high enough stress in a given direction it will fracture. A fracture starts with the nucleation of microcracks or voids which then grow until eventually fracture occur, separating the two surfaces. Different fractures can occur dependent on the specimen and these are often distinguishable macroscopically and/or microscopically from the shape of and around the fracture and the state of the fracture surface. Ductile and brittle fracture modes are two relevant fracture types for metals, and which occur on failure depends on the material in terms of both alloy and processing, temperature and testing method. The dominating fracture mechanism is related to if the metal is ductile, semibrittle or brittle, which in term is related to dislocation glide. For ductile metals there is little restriction to dislocation glide whilst in brittle metals most of the dislocations are immobile, allowing for little plastic deformation. In semibrittle metals the dislocations are mobile, but restricted to a limited amount of slip planes [24].

Generally there are three different modes of crack loading, mode I, mode II and mode III. Mode I crack loading is a tensile load perpendicular to the crack plane. Mode II is a sliding mode caused by a shear load parallel to the crack plane and perpendicular to the crack front. Mode III is a tearing mode caused by a shear load parallel to both the surface of the crack and the direction of the crack [24]. The fracture modes will not be covered further in this report, but is worth mentioning due to their known impact on fracture toughness on some materials, and due to this being relevant for further cited papers.

2.9.1 Ductile fracture

Ductile fractures occur as a result of void nucleation, and the growth and coalescence of these voids. This is illustrated for a ductile tensile specimen in Figure 2.26. Most alloys contain some level of dispersed phases varying in size from a few nanometers and up to several hundred micrometers. Nucleation of voids often occur around such particles, and depends on both the mechanical properties of the particle relative to the matrix and on its coherency to it. In the case of coherent, but brittle, particles they often break during the beginning of plastic deformation as they are not able to withstand the plastic strain of the ductile matrix. This breaking creates a void in or around the particle, and is most common with smaller particles. However, if the particle is brittle and with little coherency to the matrix interfacial separation occurs, and a void is nucleated on the interface between the particle and matrix. This is more common with larger particles as strong interfaces between matrix and particle here is unusual. As the particles are larger the voids nucleated during the interfacial separation are also larger compared to voids nucleated as a result of the breaking or separation of smaller particles [24].

The voids grow as the stress increases, and the metal separating the voids start undergoing necking on a microscopic scale. Eventually the voids grow together, or coalesce. Void growth at low growth rates or higher temperatures is caused by vacancy flows into the

void causing it to increase in size. However, at higher strain rates or room temperature the main cause for void growth include the displacement of matter due to dislocation emission [24, 46]. Lubarda et al. [46] suggests that the main mechanisms for void growth is the emission of prismatic dislocation loops and shear loops from the void surface.

When a great enough area of voids have coalesced this will act as the primary crack or fracture that will grow and eventually lead to failure. As the cross section area of the specimen is now smaller due to necking and the internal crack, this region will experience a higher stress. This leads to more voids being generated here and the crack grow further as it expands into these voids. In the case of cylindrical specimens of ductile metals, the crack will first nucleate and grow from the centre of the specimen and outwards normal to the tensile axis. However, as it reaches the outer edges of the specimen the elastic-plastic constraints change, favouring a plane of maximum shear at approximately 45° to the tensile axis [24]. Here the voids will grow and coalesce more rapidly as the cross section area now carrying the stress is severely reduced and the two specimen surfaces are quickly separated completely.

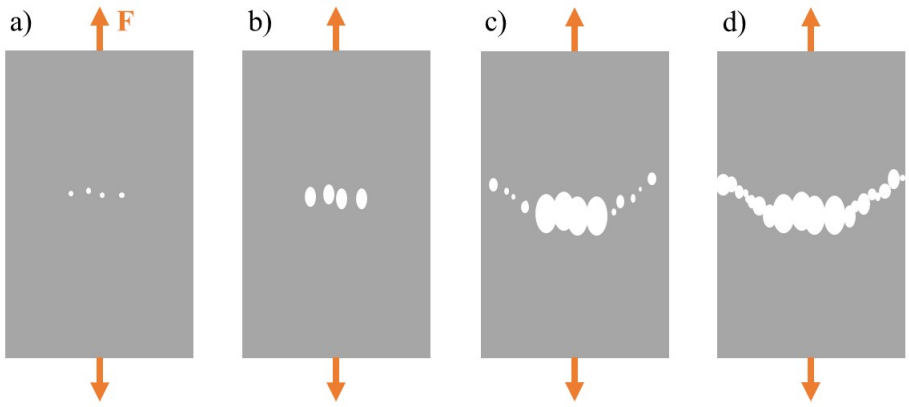

Figure 2.26: The a) nucleation of voids, b) void growth, c) coalescence of void and d) complete separation of surfaces in a ductile specimen under the tensile load F.

Ductile fractures can have quite distinct looks both macroscopically and microscopically. Specimens having experienced a ductile fracture will in most cases show signs of local plastic deformation prior to failure, usually in the form of necking, giving the fracture surface a reduced cross section area compared to the rest of the specimen. The surface will appear rough and non-reflective, and sometimes with visible dimples.

The dimpled surfaces of ductile fractures are very recognizable microscopically. These dimples are the result of voids that have nucleated and grown inside the specimen due to the high stresses. The size of the dimples will vary depending on the overall ductility of the metal and on the sizes of the initial voids nucleated. Voids nucleated from large

particles will be larger to begin with and have more potential for growth. These leave bigger dimples compared to smaller particles, and in alloys containing various different precipitates and particle sizes a large variation of dimple sizes may be seen. In the cases where particle separation was the cause of the voids a particle, or an imprint of a particle, can often be seen at the bottom of the dimple [24].

In an experiment analysing the fracture characteristics of a 7010 alloy exposed to both mode I and mode III fracture tests, Raju et al. [47] found that both resulted in a ductile fracture. They concluded with this being a result of void formation around brittle intermetallic particles followed by growth and coalescence. Figure 2.27 show the dimpled fracture surface of the mode I loaded specimen [47].

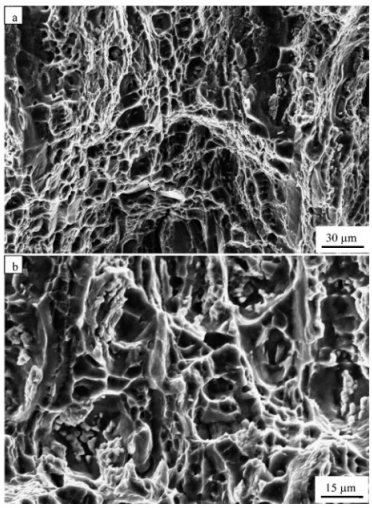

Figure 2.27: The fracture surface of a 7010 aluminium alloy [47].

2.9.2 Brittle fracture

Brittle fractures can be either transgranular or intergranular. Macroscopically both these fracture types yield a smooth and reflective fracture surface, but microscopically they are quite different. They are usually initiated similarly as to ductile fractures, through the initiation or previous existence of micro cracks or voids. However, compared to most ductile fractures the crack growth is a lot quicker and often at an angle normal to the tensile axis and with no necking having occurred [24].

Transgranular fractures happen along specific crystallographic planes by rupture of metallic bonds. With polycrystalline metals the crack will change direction at the grain boundary in order to continue along the same crystallographic plain, as adjacent grains will have somewhat different orientations. Figure 2.28 a) show a simplified illustration the propagation of a transgranular crack through a polycrystalline metal. This results in the highly reflective fracture surface as this change in direction creates smooth facets. In some cases the fracture might propagate along several parallel planes, and eventually grow together by shear or through a secondary crack. This phenomenon results in small lines or ripples

in the facets called river markings [24].

Intergranular fractures follow the grain boundaries in a metal. This is a low-energy fracture mode and is the result of the grain boundaries being more brittle than the crystal lattices. Figure 2.28 b) show a simplified illustration the propagation of a intergranular crack through a polycrystalline metal. On a microscopic level the fracture surface consist of the outline of the grains along where the fracture occurred, and, depending on the grain shape, will appear rougher than a transgranular fracture [24].

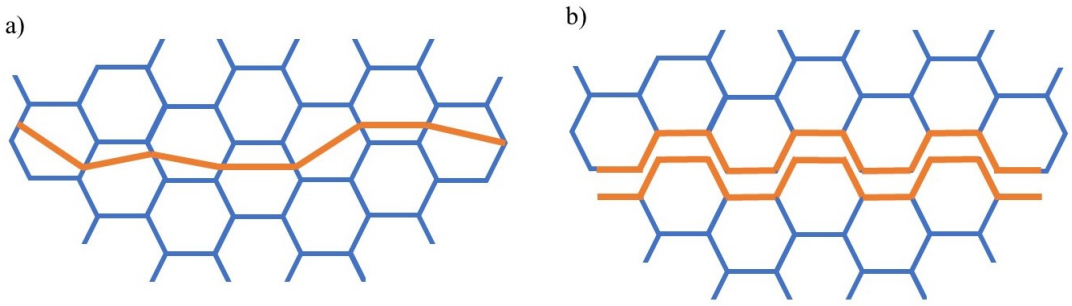

Figure 2.28: Crack propagation of a) a transgranulare fracture and b) an intergranular fracture.

Ludtka et al. [48] conducted a fracture tests on four different 7xxx aluminium alloys that varied in the volume fraction of strengthening precipitates as a result of different Mg and Zn contents. They were all aged to T6 and tensile tested to determine yield strengths between 496 MPa and 619 MPa. From the following fracture testing they found that the alloys with the lower yield strengths experienced transgranular fractures, but as the yield strength increased there was a transition to intergranular fracture. Figure 2.29 show secondary electron images of a) the fracture surface of the lowest yield strength alloy with a transgranular characteristic, and b) the fracture surface of the highest yield strength alloy with an intergranular characteristic [48].

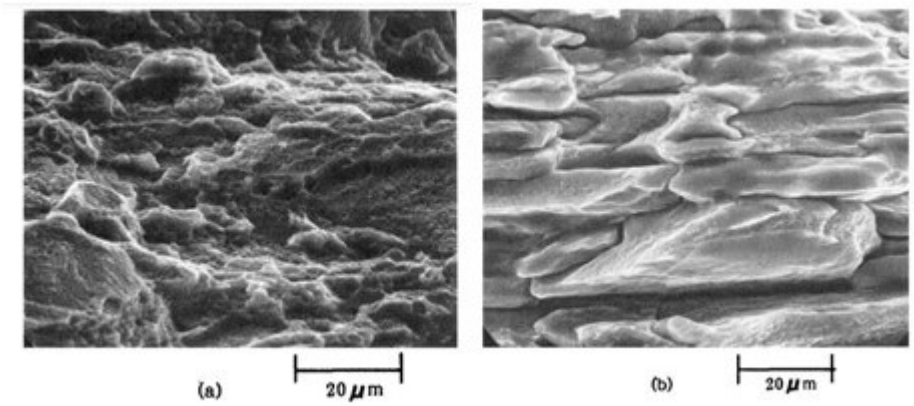

Figure 2.29: Secondary electron images showing a) the transgranular fracture of the low yield strength alloy and the b) intergranular fracture of the high yield point alloy [48].

2.9.3 Slant fractures

Slant fractures differ from ductile and brittle fractures on a macroscopic level as they happen along a specific angle in one or more directions across the specimen surface. They usually occur along plastic flow instabilities like PLC bands or shear bands, mentioned in Chapter 2.8, which is related to the angle of the fracture. Despite their characteristic appearance macroscopically, they will have a ductile or brittle character microscopically depending on the fracture mode [24, 49].

When viewed in profile using a light optical microscope under polarized light a ductile fracture will show as a smoother edge with a band of deformed grains or deformation in the grains near the fracture edge. This is due to the grains having sheared off as a form of ductile fracture. In comparison a brittle slant fracture viewed in profile in a light optical microscope under polarized will have a rougher edge consisting of smaller steps where the fracture has propagated along and across the grains and. Pedersen et al. [49] found these characteristic steps in a 7075 grade aluminium quasi-static tensile test specimen, as shown in Figure 2.30 [49].

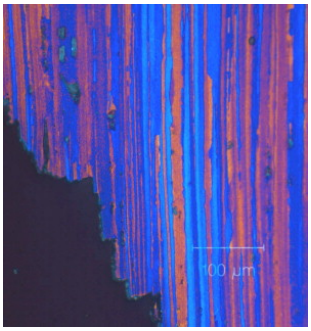

Figure 2.30: Slant fracture of a 7075 grade aluminium quasi-static tensile test specimen under polarized light in a light optical microscope [49].

These steps can also be visible at higher magnifications using a SEM. Here Pedersen et al. observed one specimen type from Figure 2.30 with a fracture surface that "consists of grain boundary facets which are decorated with small precipitates and narrow transgranular fracture with high density of dimples". He suggested the cause was intergranular crack growth along grain boundaries and precipitation free zones, and partly transgranular crack growth by void formation around particles observed in the surface using backscatter electron imaging. Figure 2.31 show an image of the surface of this specimen using secondary electron imaging to view topography and backscatter electron imaging to enhance atomic number contrast [49].

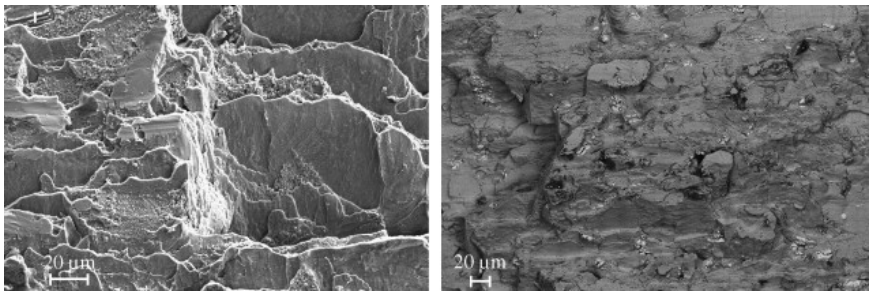

Figure 2.31: A secondary electron image, left, and a backscatter electron image, right, of the fracture surface of a 7075 grade aluminium quasi-static tensile test specimen [49].

Xu et al. [50] also investigated fractures in a 7075 alloy from tensile testing using specimens with different geometries. In most cases a brittle-ductile character was observed. A specimen that had a machined in central hole showed characteristics of the crack having propagated along grain boundaries and with the cross section of the grains being dimpled from potentially having separated due to void nucleation and growth around particles in the grain, before meeting the fracture at the grain boundaries. This is shown in Figure 2.32 a). The backscatter electron image also show particles embedded in the dimples [50].

A plane strain grooved specimen however showed less, although still some, ductile character and Xu et al. observed more a combination of intergranular fractures and transgranular fractures, but still with ductile crack propagation across some grains due to void nucleation around larger particles [50]. This is shown in Figure 2.32 b). Xu et al. stated that a potential reason for the intergranular fracture was that the grain boundaries, or areas around them, in 7075 grade aluminium are precipitation-free zones, making them weaker with fewer obstacles for for the cracks to meet [50].

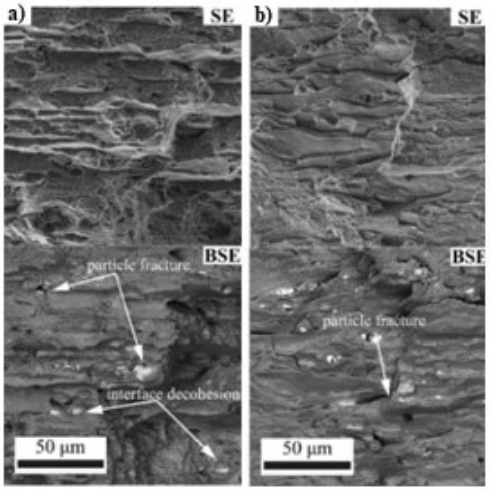

Figure 2.32: Secondary electron images and backscatter electron images of a) an intergranular-ductile fracture and b) an intergranular-transgranular fracture with some additional ductile characteristics [50].

Chapter 3

Material and method

3.1 Material

For the uni-axial tensile testing the specimens were taken from a 7108 massive extruded profile and a 7108 flat extruded profile with a thickness of 3 mm. The specimens for the incremental elongation testing were taken from flat extruded profiles of a 6082 alloy and a 7003 alloy. In addition to the mechanical testing an EBSD scan was done on a 6082 extruded round profile. A list of the materials used, specifying grade, geometry and compositions is given in Table 3.1.

Table 3.1: The chemical compositions in wt% of the alloys.

	Al	Mg	Zn	Si	Fe	Mn	Zr	Cr	Cu	Ti	V	B
7108 - massive	92,23	0,9	5,6	0,2	0,3	0,5	0,15	0,04	0,05	0,03	-	-
7108 - flat	93,95	0,74	4,94	0,05	0,14	0,03	0,145	-	0,005	-	-	-
7003 - flat	93,1	0,73	0,15	0,09	0,22	0,01	0,15	0	0,01	0,02	0,01	0,004
6082 - flat	97,4	0,65	0	0,91	0,21	0,52	0	0,16	0,01	0,02	0,02	0,004
6082 - round	96,95	0,75	-	1,2	0,24	0,6	-	0,18	0,08	-	-	-

3.2 Method

3.2.1 Sample geometries and aging process of the 7108 specimens for uni-axial tensile testing

All specimens used in the uni-axial tensile testing were cut along the extrusion directions. In the case of the massive extruded profile, plates of 6 mm thickness was first cut out of it as shown in Figure 3.1. Then three specimens were again taken from each of these plates, and separated into specimens cut from the edges of the plates and specimens cut from the middle. The geometry of these specimens is illustrated in Figure 3.2 a). From the flat extruded profile two different sample geometries were take, the main difference being the width of the specimens, as illustrated in Figure 3.2 b) and c), giving one square and one rectangular cross section.

In terms of aging the specimens from the 7108 massive extruded profile were naturally aged for 10 months following solutionizing. The specimens from the 7108 flat extruded profile were naturally aged for around 20 years following solutionizing.

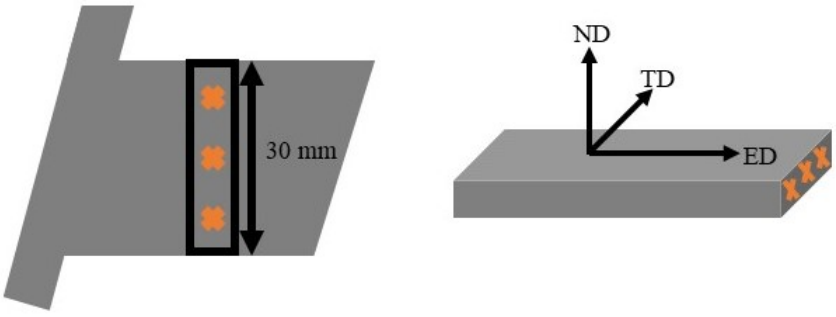

Figure 3.1: The cross section of the massive extruded profile and the profile of the plate cut from it. The square marks where the plates were cut from and the red crosses where the specimens were taken from. On the plate is shown the reference directions.

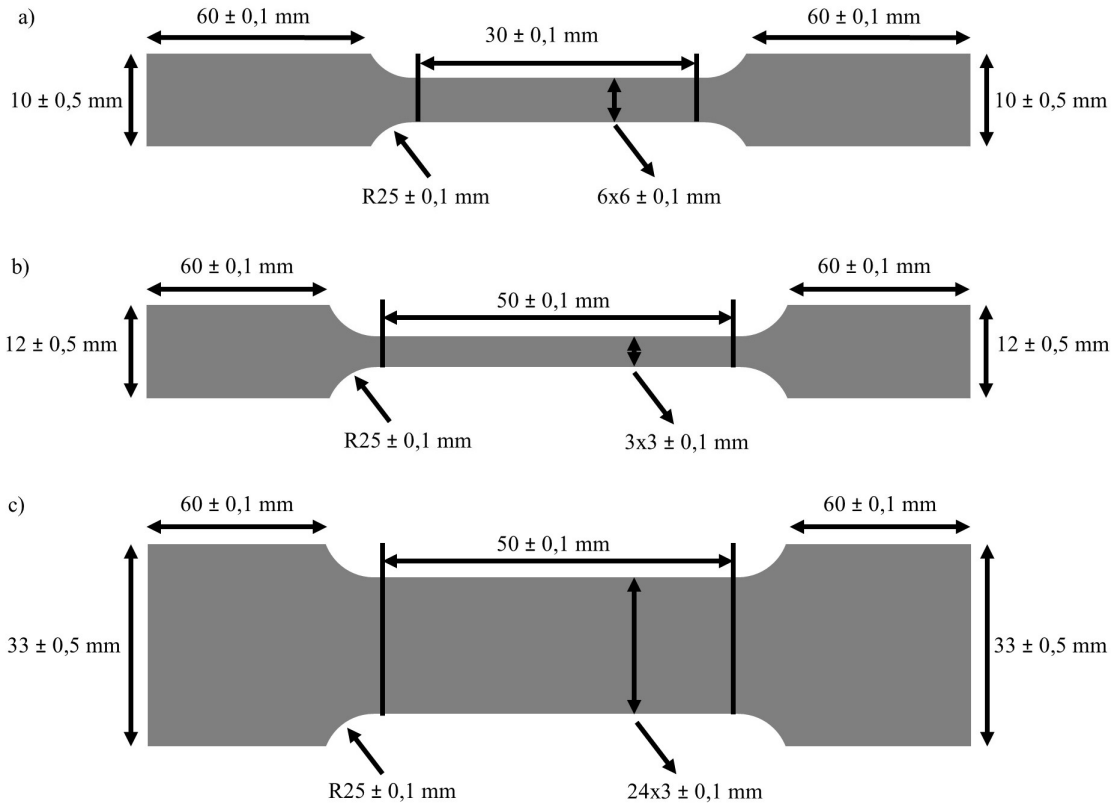

Figure 3.2: The tensile specimen geometries. a) is the geometry for the specimens of the massive extruded profile and b) and c) the geometries for the specimens from the flat extruded profile.

3.2.2 Uni-axial tensile testing of the 7108 specimens

Uni-axial tensile tests were performed on the different materials to determine their strength, tendencies of uniform and/or local plastic deformation and fracture types. An MTS-100 kN Tensile/Fatigue test machine was used for the experiments. All tests were conducted at room temperature using a strain rate of 0,0014 s^{-1}. Due to the greater cross section area of the rectangular specimen from the flat extruded profile, stronger load cells were used compared to on the rest of the specimens.

In the case of the specimens from the massive extruded profile three specimens taken from the middle of the plate cut from the profile and three specimens taken from the edges were tested and compared. The strain was measured using a 25 mm MTS extensiometer as seen in Figure 3.3 of the tensile test setup. The stress and strain data was retrieved from the machine computer and plotted as nominal stress-strain curves.

In the case of the specimens taken from the flat extruded profile three of each geometry were tested. Here the strain was also measured using a 25 mm MTS extensiometer, placed in the centre of the specimen as it was to short to cover the entire length. The stress and strain data was retrieved from the machine computer and plotted as nominal stress-strain

curves. Figure 3.3 show the setup for the rectangular specimen from the flat extruded profile. For the rectangular specimens the width and thickness were measured before and after the tensile tests in order to calculate r-values and theoretical θ angles. r-values were found using Equation 2.8 and the theoretical θ angles were found using Equation 2.14. The width and thickness data used in the calculations are given in Appendix B.

Figure 3.3: The setup for tensile testing with extensiometer for the rectangular sample.

3.2.3 Sample geometry and pre-treatments of the 6082 and 7003 specimens for incremental elongation testing

All specimens used in the incremental elongation testing were cut along the extrusion directions. The same geometry was used for both the 6082 and the 7003 specimens and is illustrated in Figure 3.4. The same geometries were also used for the tensile testing done on one of each specimen type.

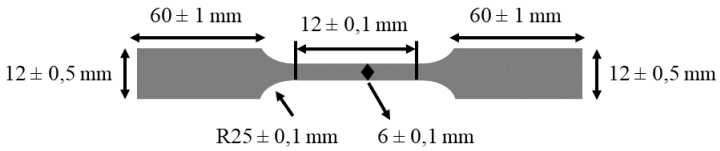

Figure 3.4: The sample geometry of the specimens used for incremental elongation testing.

Prior to the incremental elongation testing and tensile testing of the 6082 and 7003 specimens they were solutionized in salt baths and quenched in water right before the testing. The 6082 grade specimens were treated at 525°C for 30 minutes and the 7003 grade specimens were treated at 480°C for 40 minutes.

3.2.4 Incremental elongation testing of the 6082 and 7003 specimens

Incremental elongation tests were performed on the different alloys to attempt to enhance their formability, and to map out potential restrictions. An Instron-250 kN Tensile/Fatigue test machine was used for the experiments. The specimen setup is shown in Figure 3.5. Prior to the testing data sets were made that would instruct the machine of the incremental elongation it would perform on the sample. Specifically they specified the position of the loading cell per time for each step, and in the general case of incremental elongation consisted of a specific elongation done over a short time interval, less than a second, followed by 10 seconds of holding time with no elongation.

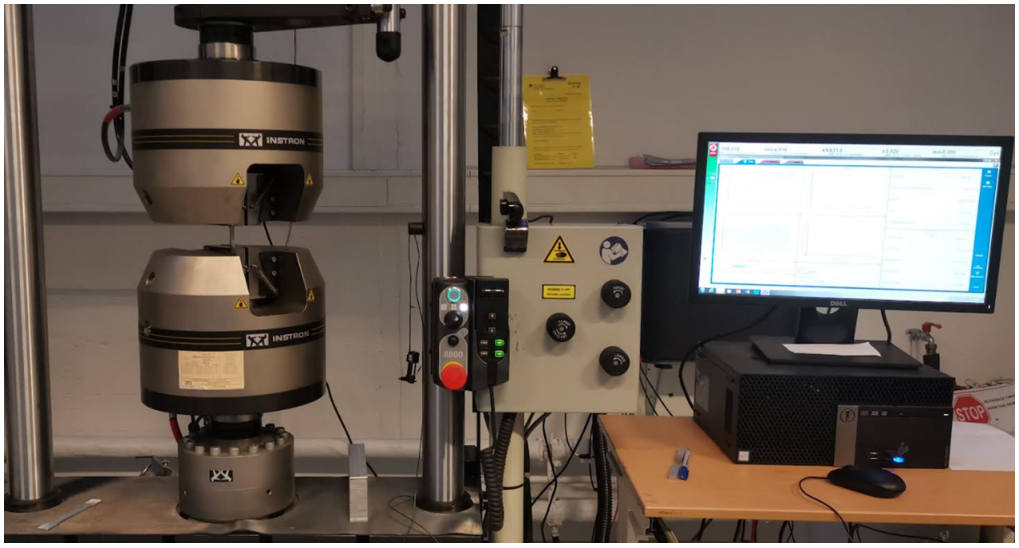

Figure 3.5: The setup for incremental elongation testing.

The values used to calculate the elongation time and position change for each data set is given in Table 3.2. It shows the position change relative to the length of the specimen making it increase with 1,25 % of the specimen length each elongation, the holding time between elongations, the maximum position of the loading cell relative to starting position (same as final maximum length of the sample) and the strain rate. The only varying parameter is the strain rate and the three different data sets generated from these values were used when testing both the 6082 and 7003 grade specimens. These data sets are listed in Appendix A.

Table 3.2: The values and parameters used to generate the data sets for the incremental elongation testing.

Position change [-]	1,0125
Holding time [s]	10
Max position [mm]	10,0565615
Strain rate [s^{-1}]	0,05
	0,07
	0,1

The load and position data collected from the machine computer is converted into stress and strain, and then each is plotted as a function of time. As the specimens were to short for an extensiometer the elongation of the specimens is based on the measured position from the machine and not the precise specimen elongation. This does not account for any position change caused by changes in the grip of the loading cells during testing.

For each of the specimen types a tensile test was also performed in order to be able to compare the strains achieved and the maximum stresses applied. As mentioned in the previous chapter these had the same geometry and pre-treatment as the specimens used for incremental elongation testing. The same method was used here as with the tensile testing from Chapter 3.2.2, but without the extensiometer as the specimens were to short. The strain is again based on the position of the loading cells which does not account for any position change caused by changes in the grip during testing.

3.2.5 Preparation for light optical microscopy imaging of tensile specimen fracture profiles

Light optical microscopy under polarized light was performed on the profile of the fracture surfaces of the 7108 specimens from the middle and edge of the massive extruded profile and the rectangular from the flat extruded profile. It was done in order to analyze and help determine the fracture mode of the specimens by studying the grains close to the fracture surface. The viewing direction relative to the sample coordinate system, depicted in Figure 3.6, depended on the direction of the slant fracture in the case of the specimens from the massive extruded profile. The middle specimens were viewed from the normal direction and the edge specimens were viewed from the transverse direction. The rectangular specimen was also viewed fro the transverse direction.

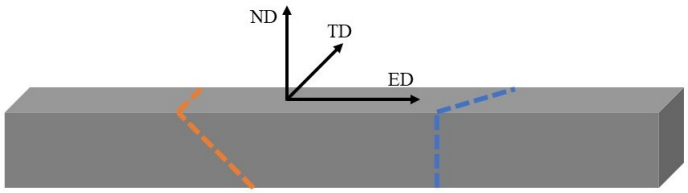

Figure 3.6: The direction of the fractures as compared to the reference system. The orange line show the slant fracture occurring across the ND-ED plane for the edge and rectangular specimens, and the blue line show the slant fracture occurring across the ED-TD plane for the middle specimen.

Prior to the microscope viewing the specimens were cast into epoxy, polished and anodized in order to ensure the grains would show up under polarized light. For the casting a two component quick drying epoxy resin was used. The casts were then gradually polished down to 1 µm using the Struers Tegramin-30 before being anodized. The specimens were anodized by inserting the samples into a container with fluoroboric acid (HBF_4) for 90 seconds at 20 Volts. They were then thoroughly washed and dried before the microscopy was performed.

3.2.6 SE imaging and BSE imaging of the fracture surfaces

The fracture surfaces of an edge and middle specimen from the massive extruded profile, square and rectangular specimen from the flat extruded profile and 7003 grade specimen from incremental elongation testing were analyzed using a Zeiss Ultra 55 FEG-SEM. The purpose was to study the topography of the fracture surface to help determine the fracture mode, and to see if particles could be found near dimples or other related areas. SE imaging was used to for viewing the topography, and BSE imaging was used to achieve atomic number contrast in order to distinguish particles from the matrix.

Prior to the electron microscopy a section containing the fracture was cut off in order for it to fit in the specimen holder. When placed in the holder the specimens were rotated for the fracture surface to be as level as possible. An acceleration voltage of 10 kV and a working distance of around 10 mm was used for all the specimens.

3.2.7 EDS analysis of particles found on the fracture surfaces

In order to help determine the chemical composition of the particles found using BSE imaging, an EDS analysis was done on a middle, edge, rectangular and 7003 specimen using a Bruker 125 eV EDS scanner attached to the SEM. For each of the specimens analysed in the SEM the particles were viewed at 10k x, and a point scan was done first of the matrix as a reference and then of three nearby particles. The resulting scans were indexed using the software QUANTAX ESPRIT 1.9 and then a quantitative analysis was

performed to determine the weight percentage of each element found in each point.

3.2.8 Preparing for and performing EBSD scans

EBSD scans were performed in the extrusion direction of the 7108 specimens taken from the massive extruded profile, one from the middle and two from each edge, the 7003 specimen and 6082 grade specimen from a round profile. The purpose was to get an overview of the texture in each of the specimens. Prior to the testing the specimens were gradually polished down to 1 µm using the Struers Tegramin-30 before being electropolished using the Struers TenuPol/LectroPol electro polishing equipment and an A2 solution at 20 eV for 15 seconds.

During the scan an acceleration voltage of 20 kV and a working distance around 26 mm was used for all the specimens. Primarily two different scan types were performed on the specimens from the massive extruded profile, one coarse (low resolution) and one fine (high resolution) scan. The coarse scans were done at 100 x and covered an area of 2,7 mm x 2,7 mm each. Four of these course scans were done per specimen and after indexing, using the program OIM Analysis, they were put together into one 4 mm x 4 mm inverse pole figure (IPF) map. Pole figures were also obtained from the coarse scans. The finer scans were done at 200 x. After indexing these were used for grain boundary imaging that show grain boundaries and sub-grain boundaries.

The scan of the 7003 grade specimen was done at 300 x. This was then indexed, and IPF maps and pole figures were created. The scans of the 6082 grade round specimen was done similarly as the course scans of the 7108 grade specimens, where four scans at 300x were taken, indexed and put together. The IPF maps and pole figures were then created.

Chapter 4

Results

4.1 Tensile testing of the 7108 specimens from the massive and flat extruded profiles

In the Chapters 4.1 through 4.5 the data from the tensile testing of the 7108 specimens and further analysis of the resulting fracture surfaces of chosen specimens are presented. The analysis include light optical microscopy of fracture profiles under polarized light, SE and BSE imaging of the fracture surface, EDS analysis of particles found in the fracture surfaces and resulting IPF maps and pole figures from EBSD scans done on the material of the massive extruded profile.

4.1.1 Tensile testing of the 7108 specimens from the middle and edge of the massive extruded profile

The results from the tensile tests of the 7108 aluminium specimens from the middle and edge of the massive extruded profile is presented in Figure 4.1 and Table 4.1. In the table is listed relevant values such as E-modulus, yield stress, peak stress, the strain at yield and the strain at beak of each specimen, while the figure offers a more visual comparison of the middle specimens and the edge specimens. The complete table showing the test results provided by the test program is listed in Appendix C.

From Figure 4.1 it can be observed a significant difference in yield stress and peak stress between the two specimen types, with the middle specimens having a yield stress and peak stress at around 270 MPa and 400 MPa. The edge specimens have yield stresses and peak stresses closer to 350 MPa and 490 MPa, and have quite similar strains at break at around 0,007. The middle specimens have more varied strains at break however, with 0,00081 mm/mm separating Middle 2 and Middle 3, also causing a somewhat greater variation in peak stress compared to the edge specimens.

The curves of both specimen types show little sign of local deformation, apart from Middle

3 which slopes gently downwards shortly before ending. For most of the specimens a break stress was therefore not listed in the complete table from Appendix C as it was the same as the peak stress. On Middle 2 a small dip at the end of the curve can also be observed. Some of the curves also appear a bit serrated although this is assumed to be noise from the machine. A the specimens experienced a slant fracture. The fractures of the middle specimens were across the ED-TD plane while for the edge specimens the fracture were across the ND-ED plane or a mix of both.

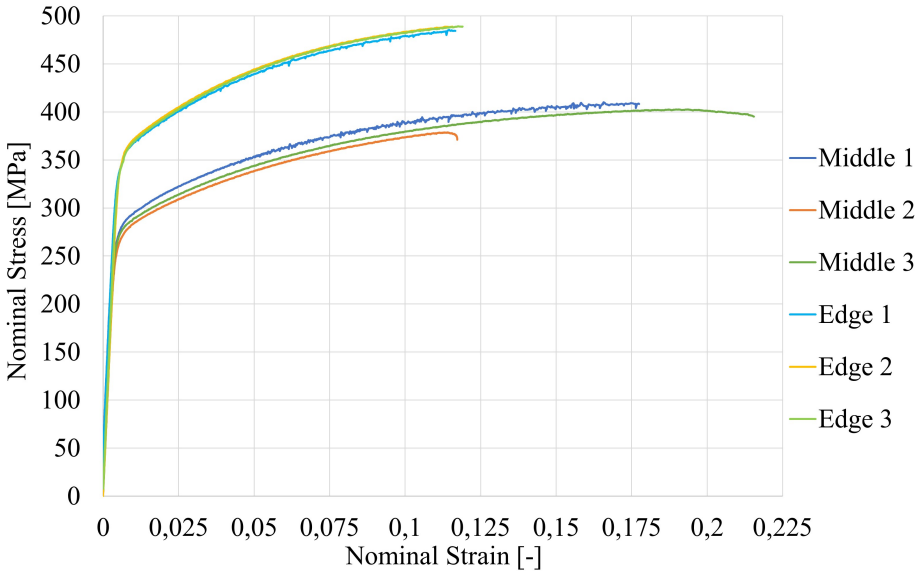

Figure 4.1: The nominal stress-strain curves of the middle specimens and the edge specimens from the 7108 massive extruded profile.

Table 4.1: The E-modulus, yield stress, peak stress, strain at break and yield strain obtained from the tensile tests of each of the middle and edge specimens from the 7108 massive extruded profile.

Specimen	Modulus [GPa]	Stress At Offset Yield [MPa]	Peak Stress [MPa]	Strain At Offset Yield [mm/mm]	Strain At Break [mm/mm]
Middle 1	69,227	268,2	378,8	0,00585	0,11726
Middle 2	71,079	272,8	410	0,00513	0,17748
Middle 3	70,359	275,4	402,7	0,00594	0,21549
Edge 1	70,182	348,5	485,5	0,00627	0,11662
Edge 2	69,54	358,2	488,9	0,0071	0,11564
Edge 3	73,594	348,1	489,2	0,00662	0,11902

4.1.2 Tensile testing of the square and rectangular 7108 specimens from the flat extruded profile

The results from the tensile tests of the square and rectangular 7108 grade aluminium specimens from the flat extruded profile is presented in Figure 4.2 and 4.3 and Table 4.2. In the table relevant values are listed such as E-modulus, yield stress, peak stress, the strain at yield and the strain at beak of each specimen. The complete table showing the test results provided by the test program is listed in Appendix C.

Both the table and the figures show a similar yield stresses and peak stresses at around 300 MPa and 400 MPa between the specimens, although there is a significant difference in strain at break with 0,03462 mm/mm separating the most elongated square and rectangular specimens. The square specimens experiencing the greatest elongation.

All specimens from the flat extruded profile experienced a slant fracture across the ND-ED plane of the flat profile. The r-values and theoretical θ angles for the rectangular specimens are presented in Table 2.14, and show that a local necking at an angle of between 10-20° should have occurred. For comparison Figure 4.4 show the fractures of Rectangular 1 and Rectangular 2.

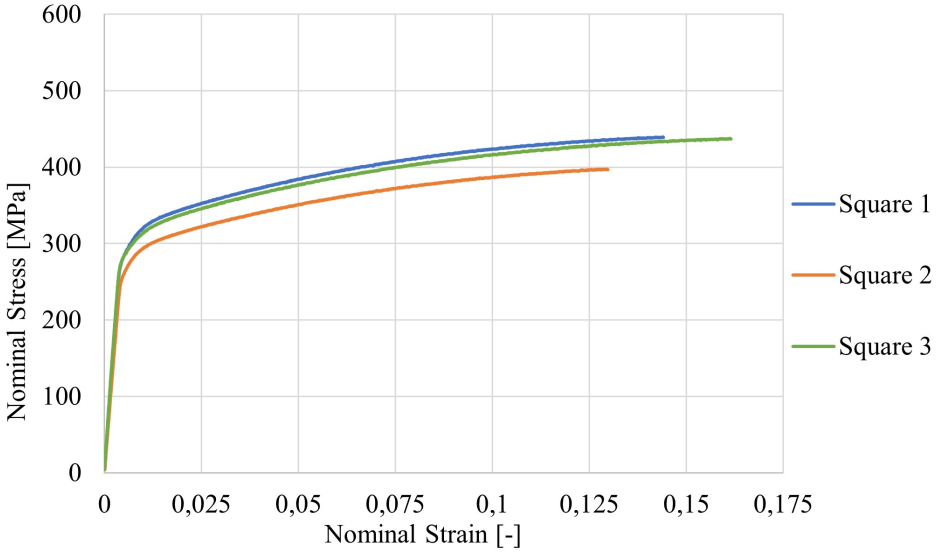

Figure 4.2: The nominal stress-strain curves of the square specimens from the 7108 flat extruded profile.

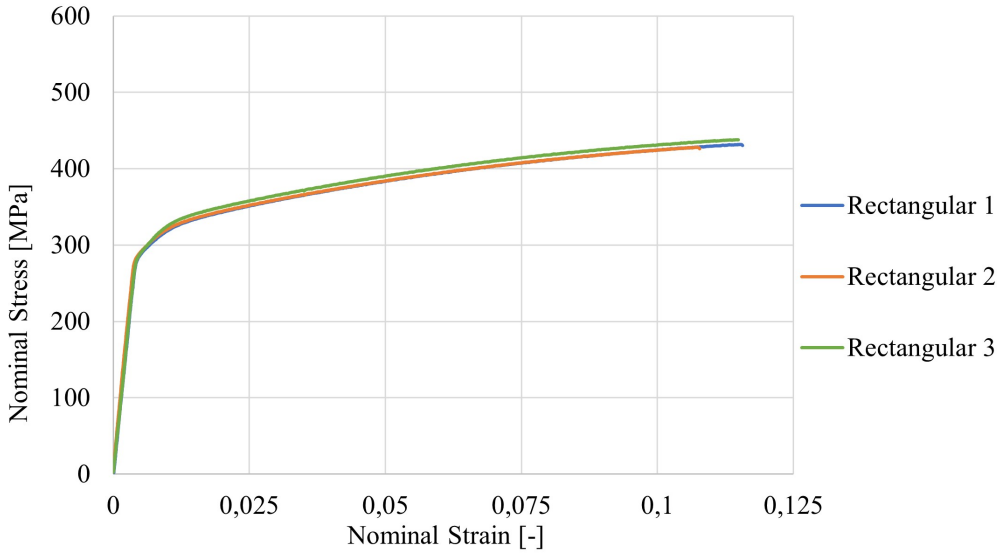

Figure 4.3: The nominal stress-strain curves of the rectangular specimens from the 7108 flat extruded profile.

Table 4.2: The E-modulus, yield stress, peak stress, strain at break and yield strain obtained from the tensile tests of each of the square and rectangular specimens from the 7108 flat extruded profile.

Specimen	Modulus [GPa]	Stress At Offset Yield [MPa]	Peak Stress [MPa]	Strain At Break [mm/mm]	Strain At Offset Yield [mm/mm]
3x3 Forsøk 1	71,578	293,8	439,9	0,15028	0,00605
3x3 Forsøk 2	62,468	273,4	397,3	0,12981	0,0064
3x3 Forsøk 3	70,904	292	437,7	0,13734	0,00602
3x24 Forsøk 1	69,833	298,1	431,8	0,11566	0,00632
3x24 Forsøk 2	74,069	298,1	428,1	0,10778	0,00595
3x24 Forsøk 3	70,162	300,4	438,3	0,11484	0,00628

Table 4.3: The r-values and theoretical θ angles of the rectangular specimens.

	r-values	θ [°]
Rectangular 1	0,33	18,52
Rectangular 2	0,18	10,45
Rectangular 3	0,35	19,45

Figure 4.4: The fractures of Rectangular 1 (left) and Rectangular 2 (right).

4.2 Light optical microscopy images of tensile specimen fracture profiles

The results from the light optical microscopy done on the fracture profiles of the tensile specimens are presented below. This includes images from one specimen from the edge specimen (Edge 1) from the 7108 massive extruded profile and one from the middle (Middle 1), and one from the rectangular specimens (Rectangular 3) of the flat extruded profile. The imaging was done on anodized surfaces in polarized light to enhance the grains.

4.2.1 Light optical microscopy images of the edge specimen from the 7108 massive extruded profile under polarized light

Figures 4.5 and 4.6 show the slant fracture under polarized light at 2,5 x and 5 x of an edge specimen. The edge of the fracture is fairly smooth, and the 5 x images reveals a slight upturned bend in on the grains at the fracture surface. The grains are fairly wide, with the larges measuring to over 150 µm. From the first image at 2,5 x the top of the specimen is seen. No local deformation is visible in this area, and the tip of the fracture has a small lip where the end of the grains have bent.

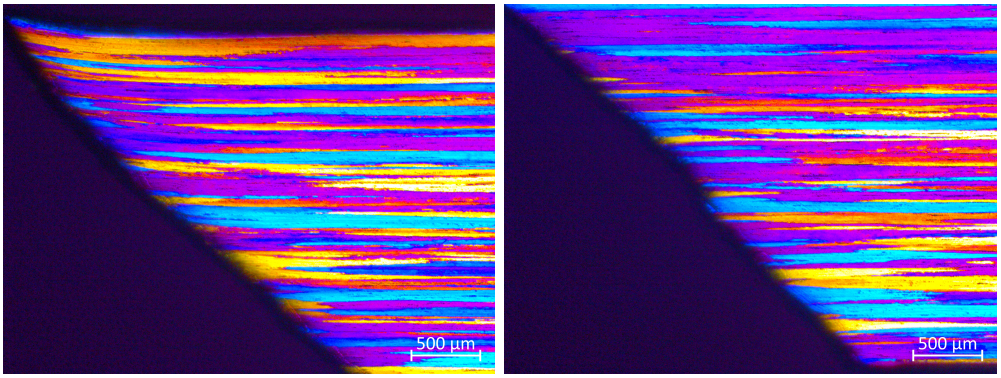

Figure 4.5: Light optical microscopy images of the edge specimen under polarized light at 2,5 x. The left image is taken of the top lip of the fracture while the right image is taken closer of the bottom.

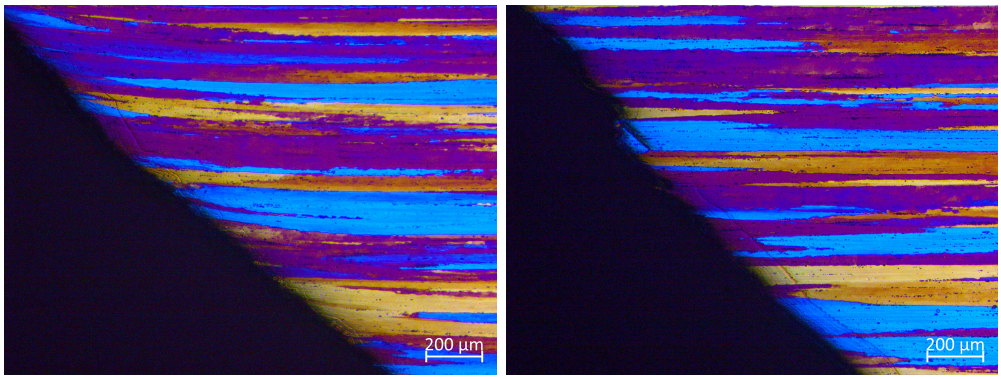

Figure 4.6: Light optical microscopy images of the edge specimen under polarized light at 5 x. The left image is taken closer to the top lip of the fracture while the right image is taken closer to the bottom.

4.2.2 Light optical microscopy images of the middle specimen from the 7108 massive extruded profile under polarized light

Figures 4.7 and 4.8 show the slant fracture under polarized light at 2,5 x and 5 x of a middle specimen. The edge of the fracture is not as smooth as for the edge specimen, especially at the bottom section of the fracture where small step-like irregularities can be seen. This is most prevalent in the third image of Figures 4.7 and 4.8.

In this lower area the grains do not appear to be deformed. However, the grains in the upper section of the fracture, both above and around the cleft, are bent following the deformation of the specimen. The grains here are significantly smaller than the ones observed for the edge specimen, where the largest seem to be no bigger than around 50 µm.

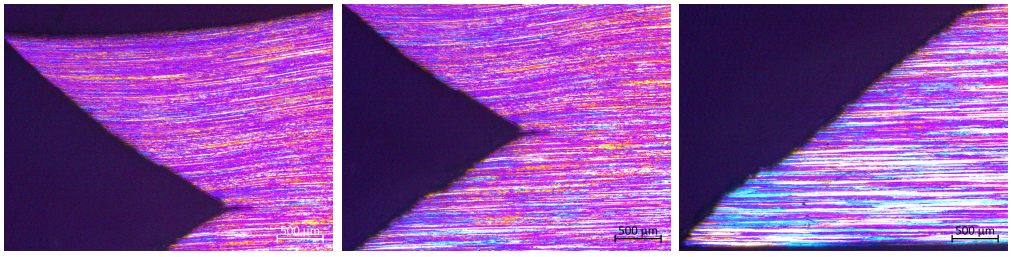

Figure 4.7: Light optical microscopy images of the middle specimen under polarized light at 2,5 x. The left image is taken of the top lip of the fracture, the middle of the cleft and the right image is taken closer of the bottom.

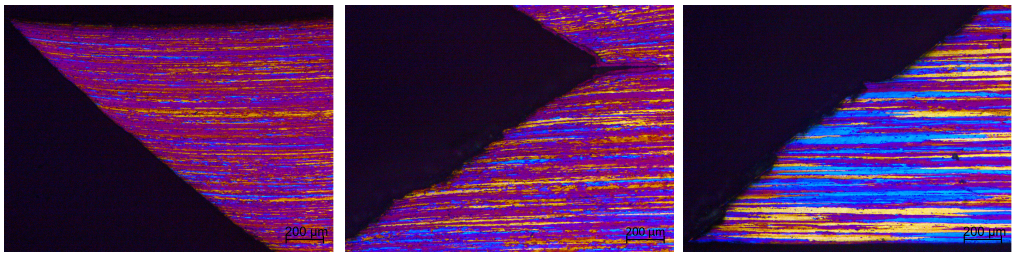

Figure 4.8: Light optical microscopy images of the middle specimen under polarized light at 5 x. The left image is taken of the top lip of the fracture, the middle of the cleft and the right image is taken closer of the bottom.

4.2.3 Light optical microscopy images of the rectangular specimen from the 7108 flat extruded profile under polarized light

Figure 4.9 show the slant fracture under polarized light at 2,5 x and 10 x of a rectangular specimen from the flat extruded profile. The edge of the fracture is also not as smooth as for the edge specimen, with small step-like irregularities visible along the edge. This is most prevalent in the second image at 10 x. However they are harder to distinguish due to poor prepping of the specimen, which somewhat obscures the lower section of the fracture profile.

The grains are also deformed around this cleft, and the grains in the upper region of the cleft seem to bend downward before straightening out. These grains are also only a few micrometer thick, although along the top and bottom of the profile there appears to be a thin region where the grains are not elongated as in the rest of the specimen, as seen in the 2,5 x image.

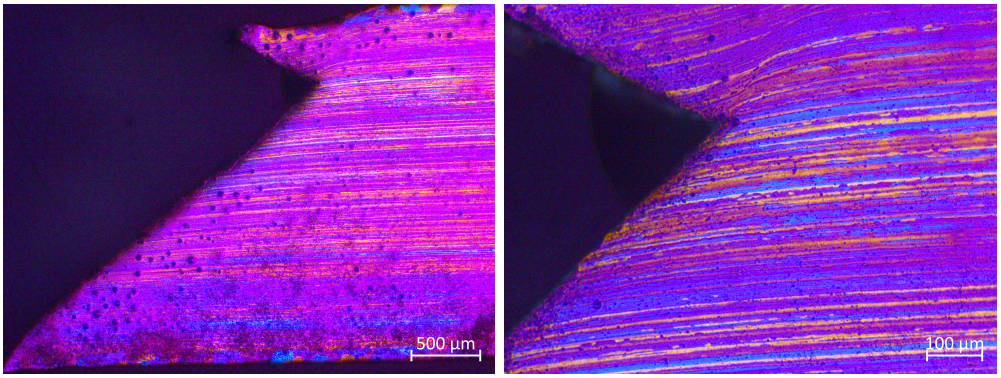

Figure 4.9: Light optical microscopy images of the rectangular specimen under polarized light at 2,5 x and 10 x. The left image at 2,5 x show an overview of the hole specimen area, and the right image at 10 x show the cleft.

4.3 Secondary electron imaging and backscatter electron imaging of fracture surfaces from the tensile specimens

The results from the SE imaging and BSE imaging of the fracture surfaces from the tensile specimens are presented below. These images cover both topographical characteristics of the fracture surfaces and particles found on the surfaces, enhanced by atomic number contrast. The scans were done on an edge (Edge 2) and a middle (Middle 2) specimen from the massive extruded profile and on a square (square 1) and rectangular (rectangular 1) specimen from the flat extruded profile.

4.3.1 SE and BSE imaging of fracture surface of the 7108 aluminium specimens from the edge of the massive extruded profile

The images taken of this fracture surface show a mostly dimpled surface with some flatter areas in between. The larger dimples are around 10 µm in diameter, but areas of smaller dimples, only a few micrometers wide or less, can also be seen. This is evident from the top two SE images in Figure 4.10 at 2k x and 5k x. The BSE images show that in most of the dimples there are one or more particles embedded there. Most of the particles are concentrated in and around the dimples, with fewer found on the flatter areas. The particles are lighter in color compared to the matrix indicating they consist of heavier elements. This is further covered in Chapter 4.4.

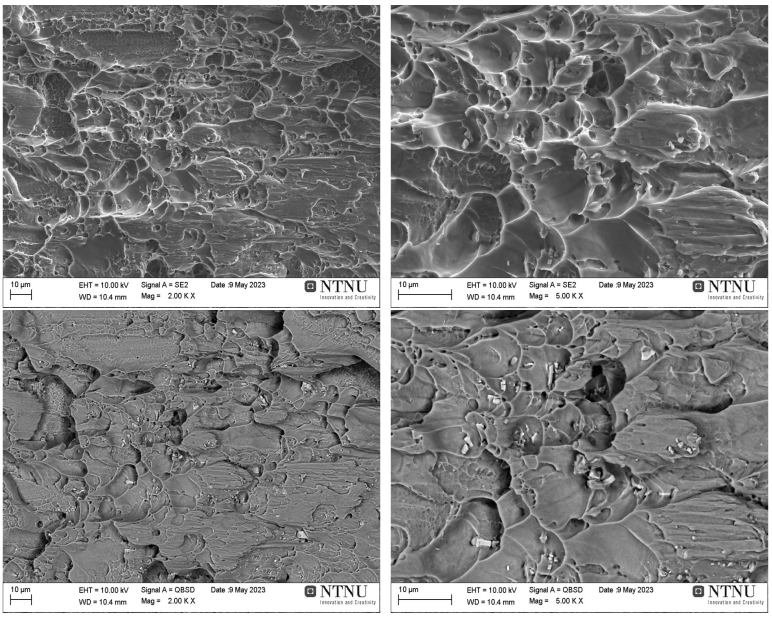

Figure 4.10: SE and BSE images of the fracture surface of the edge specimen at 2k x and 5k x.

4.3.2 SE and BSE imaging of fracture surface of the 7108 aluminium specimens from the middle of the massive extruded profile

The fracture surface of the middle specimen that was investigated in the SEM consisted of a more level section and a steeper section as the angle of this slant fracture was not perfectly even. Figure 4.11 gives an overview of the topography of the flatter section of the specimen, and show that the surface is a lot less dimpled compared to the edge specimen, with great regions that are flat and somewhat rippled.

However, the SE images from Figure 4.12 revile small dimpled areas in between the larger flat regions. These dimples are similar or smaller in size than the ones seen in Figure 4.10. As with the dimples in the edge specimen, particles with a lighter contrast where found in the bottom of these dimples as well. The BSE images also show that there are more particles in and around the dimpled areas compered to the flat areas.

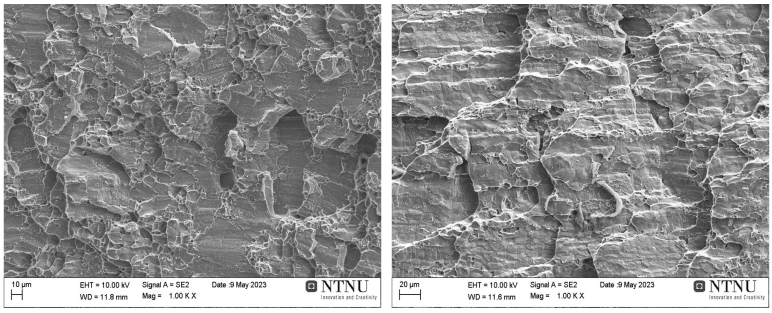

Figure 4.11: SE images of the level region of the fracture surface of the middle specimen at 1k x.

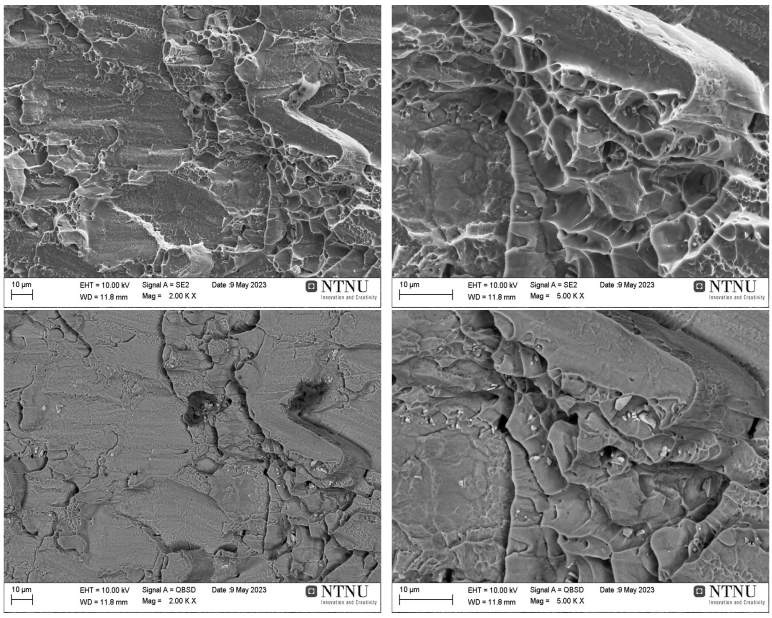

Figure 4.12: SE and BSE images of the level region of the fracture surface of the middle specimen at 2k x and 5k x.

The following images gives an overview of the steeper region of the fracture surface. Figure 4.13 show that the topography is here is similar to that of the flat region, and that particles can be seen in some areas here as well. One thing that was however not observed in the level region of the fracture surface was the small lines or ripples seen in the images in Figure 4.14. These are most prominent in the second image where the lines can clearly be seen going parallel to each other across the flat surfaces, with only a few µm separating the closest ones.

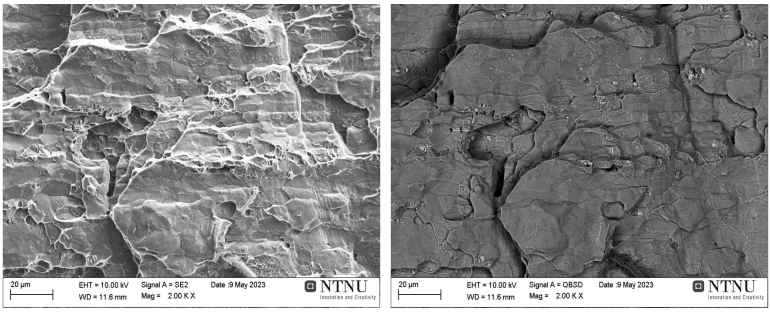

Figure 4.13: SE and BSE images of the steep region of the fracture surface of the middle specimen at 2k x.

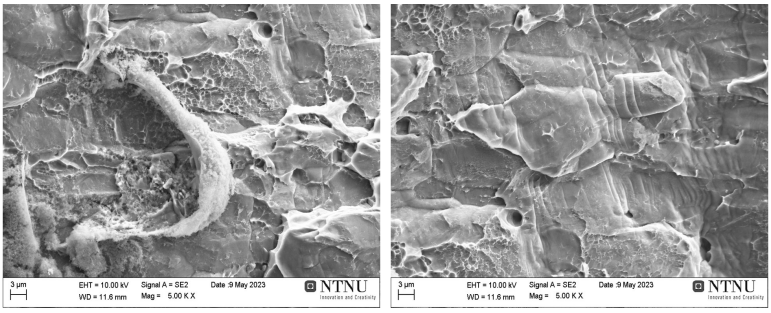

Figure 4.14: SE images of the steep region of the fracture surface of the middle specimen at 5k x.

4.3.3 SE and BSE imaging of fracture surface of the square 7108 aluminium specimens from the flat extruded profile

The SE images of the fracture surface of the square specimen show a very flat and step-like topography, as seen in Figure 4.15, with small dimpled areas scattered between and around some of the steps. These are more clearly observed in the SE images in Figure 4.16, and the BSE images show that particles embedded both in dimpled areas, but also along some of the steps.

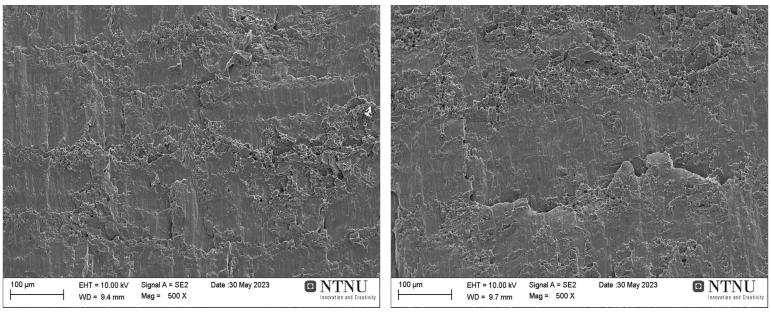

Figure 4.15: Secondary electron images of the fracture surface of the square specimen at 500 x.

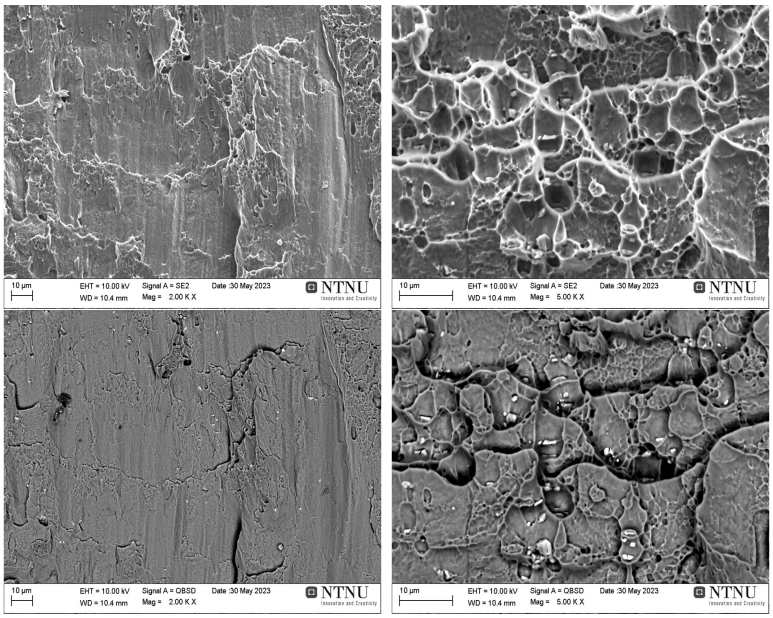

Figure 4.16: SE and BSE images of the fracture surface of the square specimen 2k x and 5k x.

4.3.4 SE and BSE imaging of fracture surface of the rectangular 7108 aluminium specimens from the flat extruded profile

The SE images of the fracture surface of the rectangular specimen show a very flat and step-like topography, as seen in Figure 4.17, with small dimpled areas scattered between and around some of the steps. These are more clearly observed in the SE images in Figure 4.18, and the BSE images show that particles embedded both in dimpled areas, but also along some of the steps. The fracture surface of this specimen have a fairly similar topography to the square specimen.

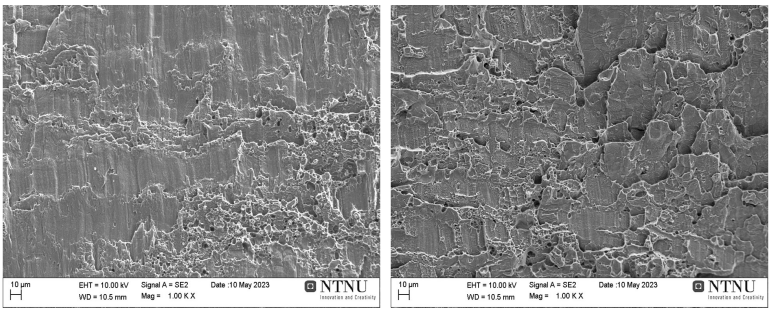

Figure 4.17: SE images of the fracture surface of the rectangular specimen at 1k x.

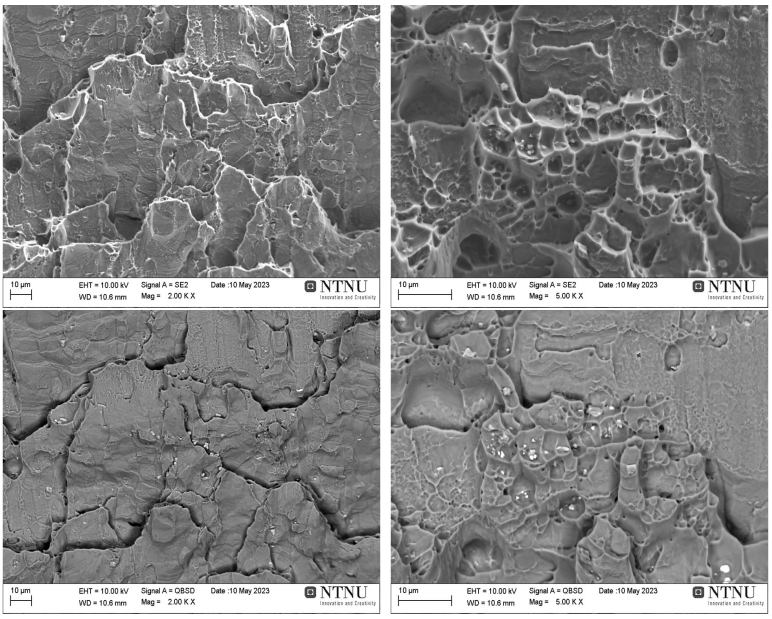

Figure 4.18: SE and BSE images of the fracture surface of the rectangular specimen at 2k x and 5k x.

4.4 EDS analysis of particles in the fracture surfaces the of tensile specimens

These EDS analyses are a further investigation of the particles observed in the fracture surfaces of the edge, middle and rectangular specimens in Chapter 4.3. The results from all the scans below are presented first with a BSE image at 10k x where the scanned points are marked. The first point is always of the matrix, while the following points are of the particles. The scan belonging to each point is then shown below, and at the end a table presents the weight percentages of all the elements found in each point. These are simplified tables where the most relevant data is listed. The complete tables containing all the values acquired from the EDS analyses are given in Appendix D.

4.4.1 EDS results from the fracture surface of the 7108 aluminium specimens from the edge of the massive extruded profile

Figure 4.19 shows the reference image for the scanned points on the fracture surface. Two different particle sizes where scanned, with the larger in point 4 being around 2 µmeter across and the smaller particles in point 2 and 3 being less than 1 µm. Figures 4.20 to 4.23 show the corresponding scans.

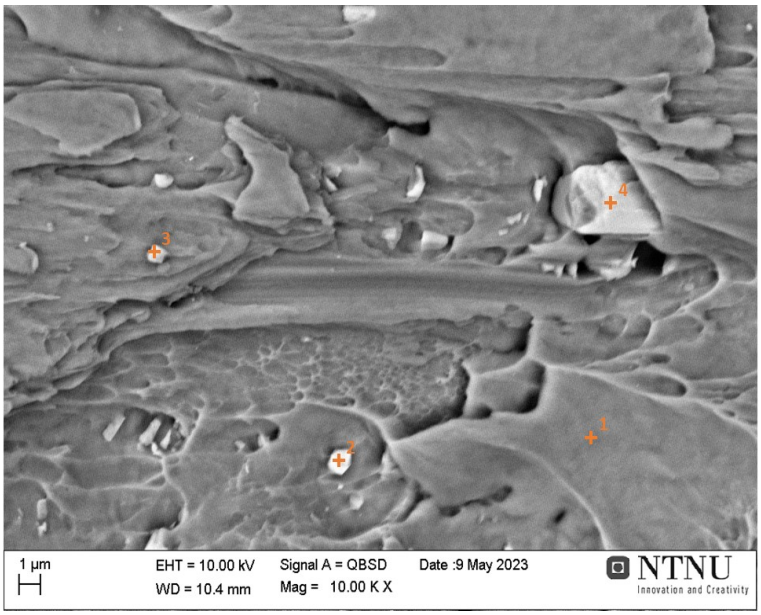

Figure 4.19: The reference image showing the 4 points scanned during the EDS analysis of the fracture surface of the edge specimen.

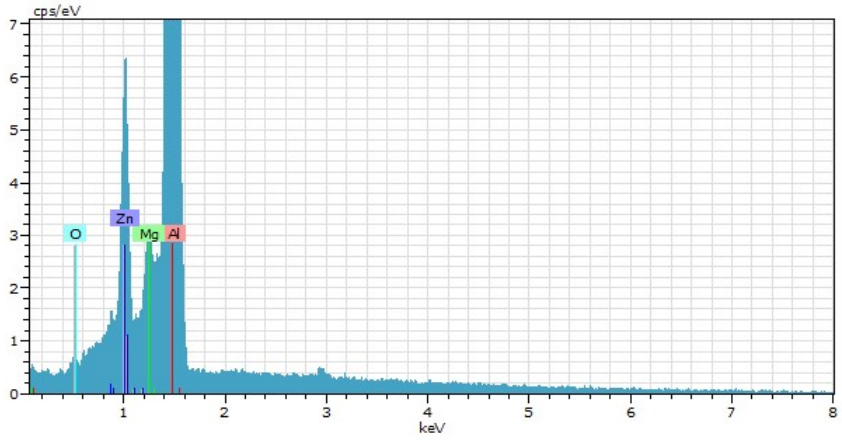

Figure 4.20: The EDS scan of point 1 in the edge specimen, corresponding to the matrix. The colored elements show the elements found in this point and what peaks they represent.

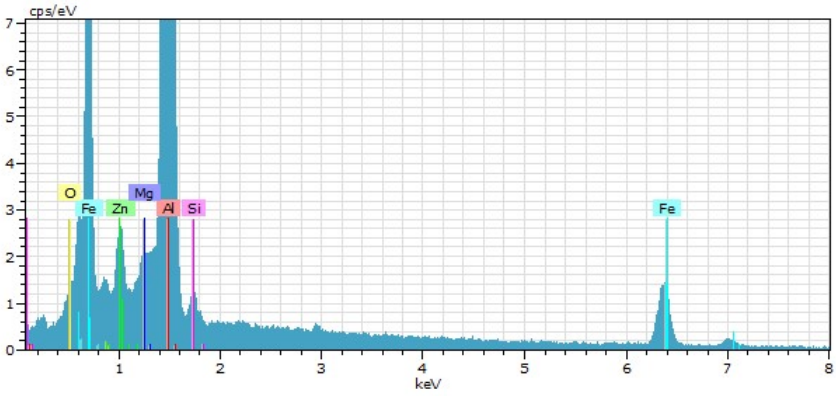

Figure 4.21: The EDS scan of point 2 in the edge specimen. The colored elements show the elements found in this point and what peaks they represent.

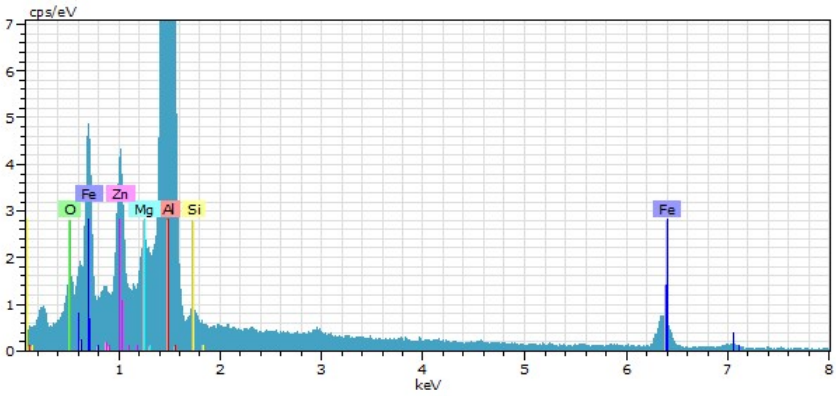

Figure 4.22: The EDS scan of point 3 in the edge specimen. The colored elements show the elements found in this point and what peaks they represent.

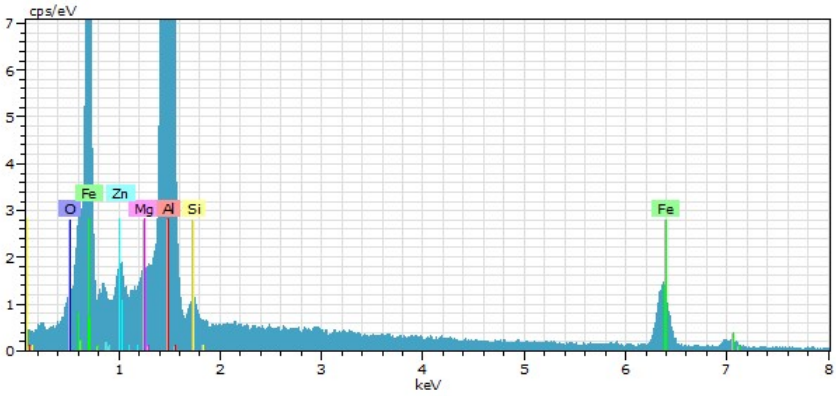

Figure 4.23: The EDS scan of point 4 in the edge specimen. The colored elements show the elements found in this point and what peaks they represent.

Table 4.4 summarizes what elements were found in each point, as well as the weight percentages of each element. Point 1, which was of the matrix, mainly contain Al, Zn, Mg

and O, with the highest content being of aluminium at 85,01 wt%. The particles in point 2-4 all contain these elements as well, but also larger amounts of Fe and some Si.

Table 4.4: Weight percentages of elements detected in the 4 points scanned in the EDS analysis of the edge specimen.

	1	2	3	4
Al [wt%]	85,01	66,39	77,48	57,92
Zn [wt%]	6,66	3,49	5,77	1,98
Mg [wt%]	1,72	1,16	1,52	0,84
Fe [wt%]	-	37,54	22,08	35,07
Si [wt%]	-	0,84	0,64	0,68
O [wt%]	0,31	1,18	1,79	0,89

4.4.2 EDS results from the fracture surface of the 7108 aluminium specimens from the middle of the massive extruded profile

Figure 4.24 shows the reference image for the scanned points on the fracture surface. Two different particle sizes where scanned, with the larger in point 4 being around 2 µmeter across and the smaller particles in point 2 and 3 being less than 1 µm. Figures 4.25 to 4.28 show the corresponding scans.

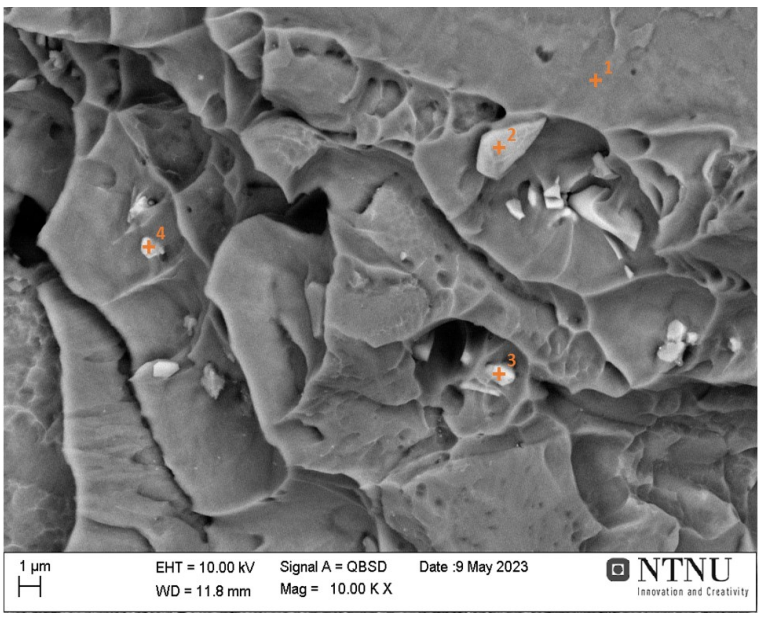

Figure 4.24: The reference image showing the 4 points scanned during the EDS analysis of the fracture surface of the middle specimen.

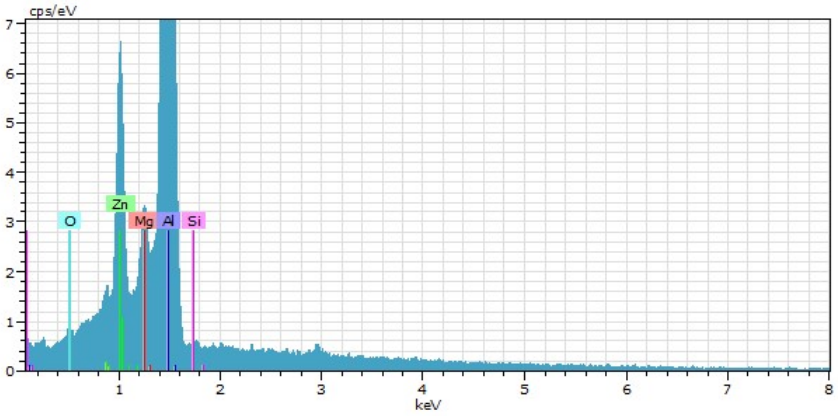

Figure 4.25: The EDS scan of point 1 in the middle specimen, corresponding to the matrix. The colored elements show the elements found in this point and what peaks they represent.

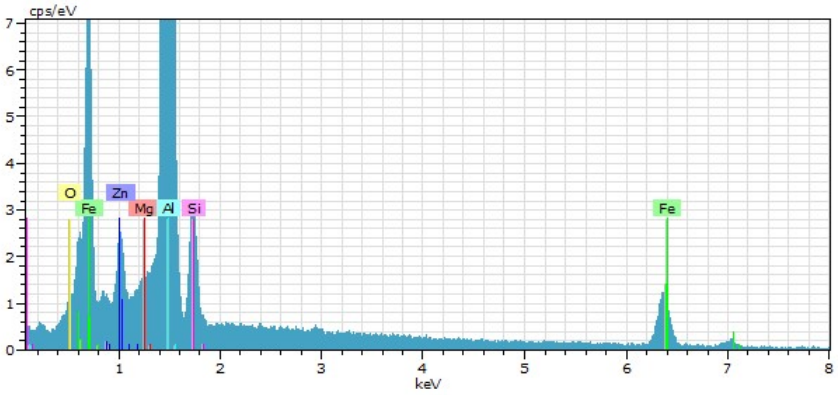

Figure 4.26: The EDS scan of point 2 in the middle specimen. The colored elements show the elements found in this point and what peaks they represent.

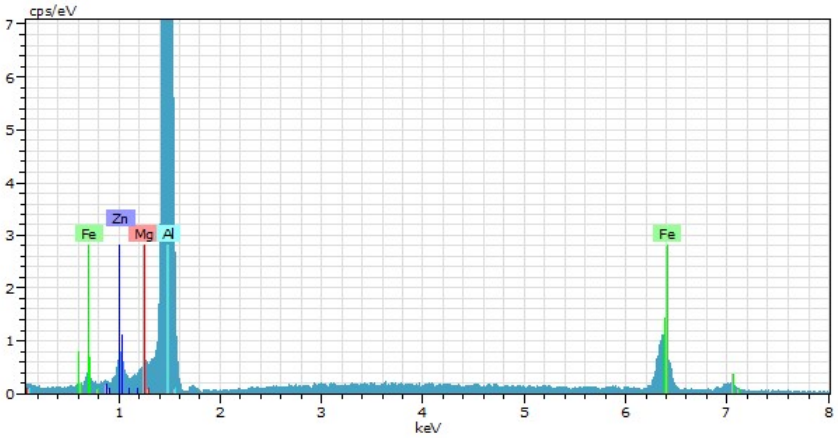

Figure 4.27: The EDS scan of point 3 in the middle specimen. The colored elements show the elements found in this point and what peaks they represent.

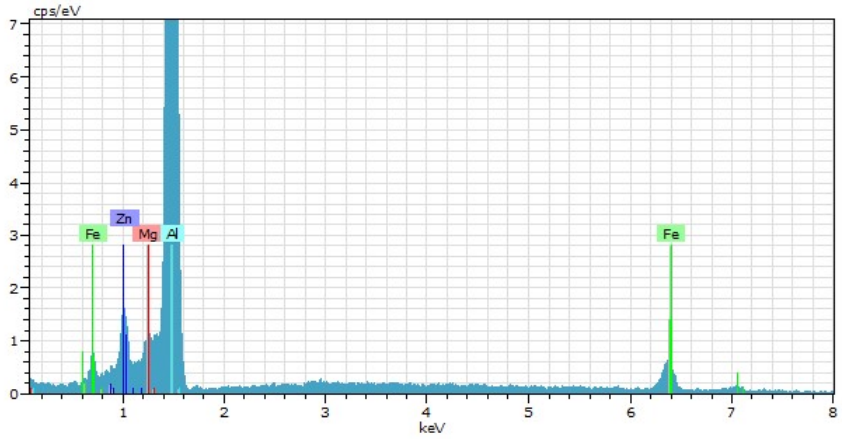

Figure 4.28: The EDS scan of point 4 in the middle specimen. The colored elements show the elements found in this point and what peaks they represent.

Table 4.5 summarizes what elements were found in each point, as well as the weight percentages of each element. Point 1, which was of the matrix, mainly contain Al, Zn, Mg, Si and O, with the highest content being of aluminium at 82,03 wt%. The particles in point 2-4 all contain Al, Zn and Mg as well as Fe, but only point 2 contain Si and O.

Table 4.5: Weight percentages of elements detected in the 4 points scanned in the EDS analysis of the middle specimen.

	1	2	3	4
Al [wt%]	82,03	56,06	58,67	74,53
Zn [wt%]	6,84	3,15	2,02	3,57
Mg [wt%]	1,7	0,75	0,56	1,11
Fe [wt%]	-	31,95	70,68	30,38
Si [wt%]	0,09	3,49	-	-
O [wt%]	0,57	0,83	-	-

4.4.3 EDS results from the fracture surface of the rectangular specimen from the 7108 aluminium flat extruded profile

Figure 4.29 shows the reference image for the scanned points on the fracture surface. Figures 4.25 to 4.28 show the corresponding scans.

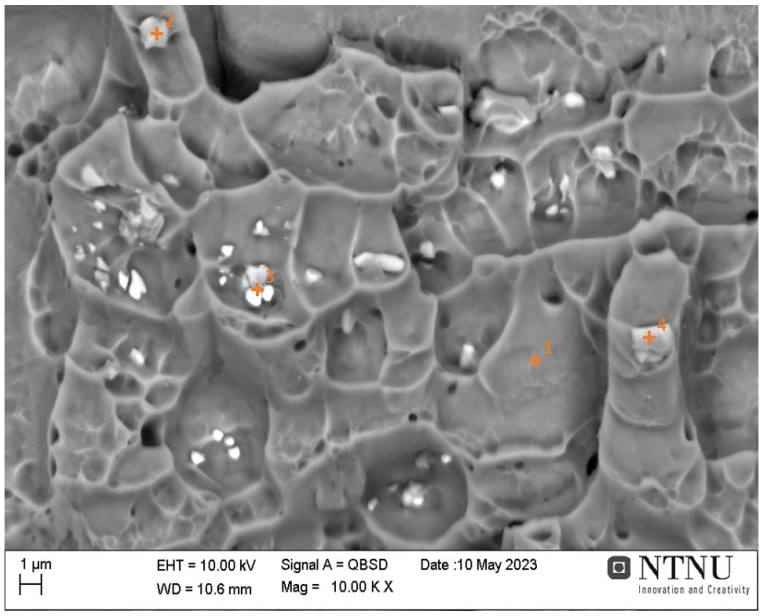

Figure 4.29: The reference image showing the 4 points scanned during the EDS analysis of the fracture surface of the rectangular specimen.

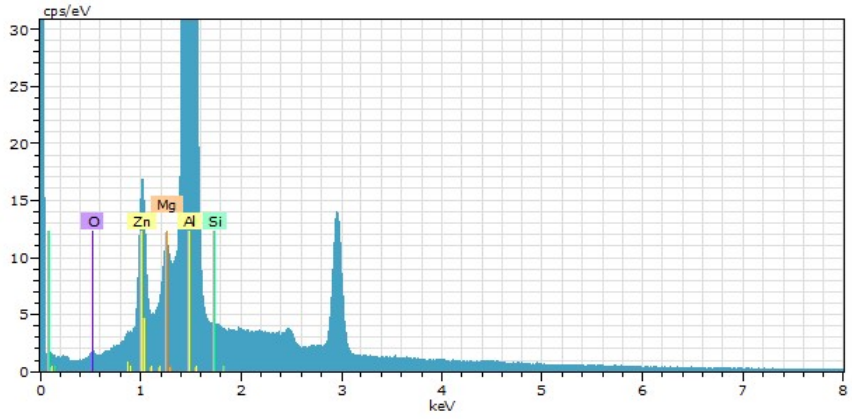

Figure 4.30: The EDS scan of point 1 in the rectangular specimen, corresponding to the matrix. The colored elements show the elements found in this point and what peaks they represent.

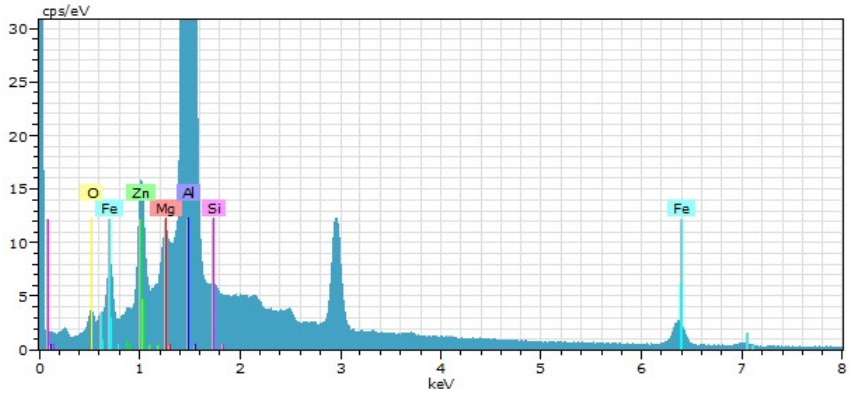

Figure 4.31: The EDS scan of point 2 in the rectangular specimen. The colored elements show the elements found in this point and what peaks they represent.

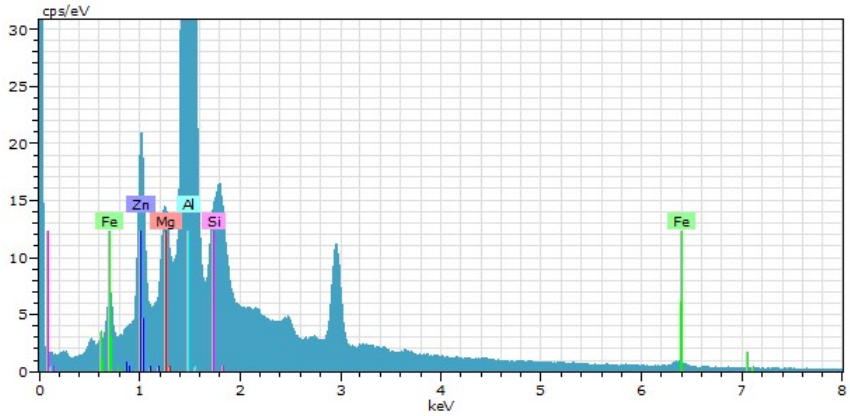

Figure 4.32: The EDS scan of point 3 in the rectangular specimen. The colored elements show the elements found in this point and what peaks they represent.

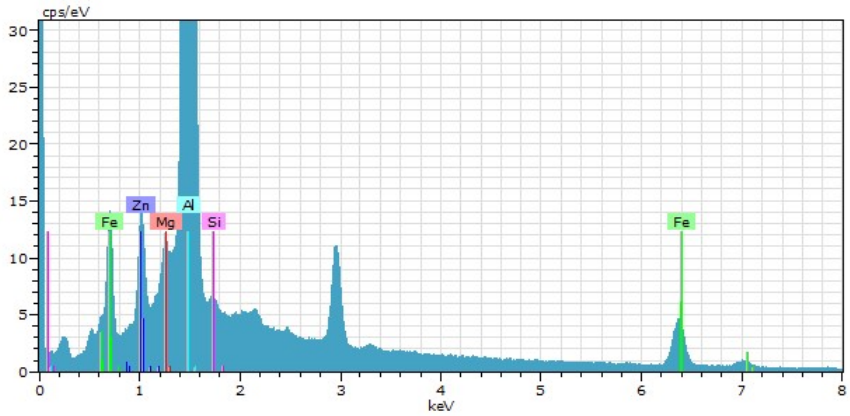

Figure 4.33: The EDS scan of point 4 in the rectangular specimen. The colored elements show the elements found in this point and what peaks they represent.

Table 4.6 summarizes what elements were found in each point, as well as the weight percentages of each element. Point 1, which was of the matrix, mainly contain Al, Zn,

Mg, Si and O, with the highest content being of aluminium at 59,52 wt%. The particles in point 2-4 all contain Al, Zn and Mg as well and Fe, but only point 2 contain O.

Table 4.6: Weight percentages of elements detected in the 4 points scanned in the EDS analysis of the 7108 grade narrow specimen.

	1	2	3	4
Al [wt%]	59,52	60,1	44,54	55,98
Zn [wt%]	2,47	2,81	2,99	2,04
Mg [wt%]	0,66	0,94	1,07	0,8
Fe [wt%]	-	12,25	2,34	19,12
Si [wt%]	0,66	1,13	3,66	0,87
O [wt%]	0,05	0,06	-	-

4.5 Inverse pole figure maps and pole figures of the 7108 massive extruded profile

The results of the EBSD analyses of the 7108 massive extruded profile are presented below, and covers a middle and two edge specimens taken along side eachother from the plate cut from the profile. They are first depicted in the form of course, low resolution IPF maps that show the distribution of the reflected planes in each of the scanned areas, with regards to the reference triangle in Figure 4.34. Following fine, high resolution IPF maps are presented. These maps show the grain sizes with high and low angle grain boundaries marked. For all IPF maps below the projection axis is the ND direction. Next the pole figures are presented, showing the reflections of the 001 and 111 planes. These pole figures are based on course, low resolution scans done of larger areas of each section of the sample.

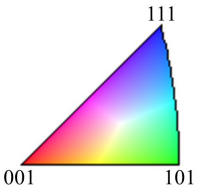

Figure 4.34: The color references for the IPFs.

4.5.1 The IPFs of the 7108 massive extruded profile

The low resolution IPFs in Figure 4.35 gives an overview of the variation in texture between the middle and edge specimens, and within the edge specimens themselves. While the middle IPF show a fairly even distribution of the colours throughout the image while for the edges there is a variation within each scan, indicating the texture is not even throughout the profile and probably not throughout the edge specimens.

Figure 4.36 show the variation in grain size between the three areas. The black lines represent grain boundaries with a rotation angle between 15° and 180°, the red boundaries with a rotation angle between 5° and 15° and the white boundaries with a rotation angle between 2° and 5°. The first and third images show that the grains here vary more in size and that some of the grains are longer and narrower, whilst others are small are quite small. The smaller grains are more circular and between 10-20 µm in diameter in each direction, while some of the larger grains are over 100 µm long and between 30-50 µm wide. The color of the images indicate the difference in the planes that are reflected in the edge maps and the middle maps, however these small areas are not very suitable for representing texture and this is better visualized in the pole figures below.

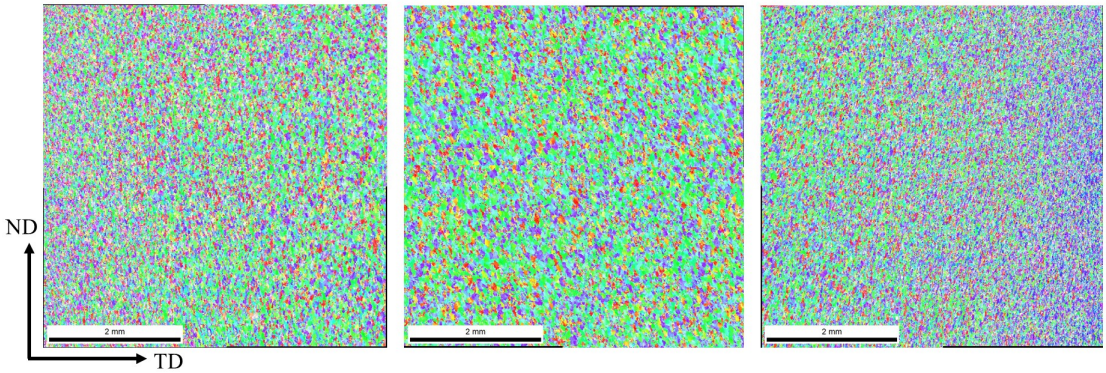

Figure 4.35: Low resolution IPF taken at 100x of the first edge (first image), middle (second image) and second edge (third image) specimens.

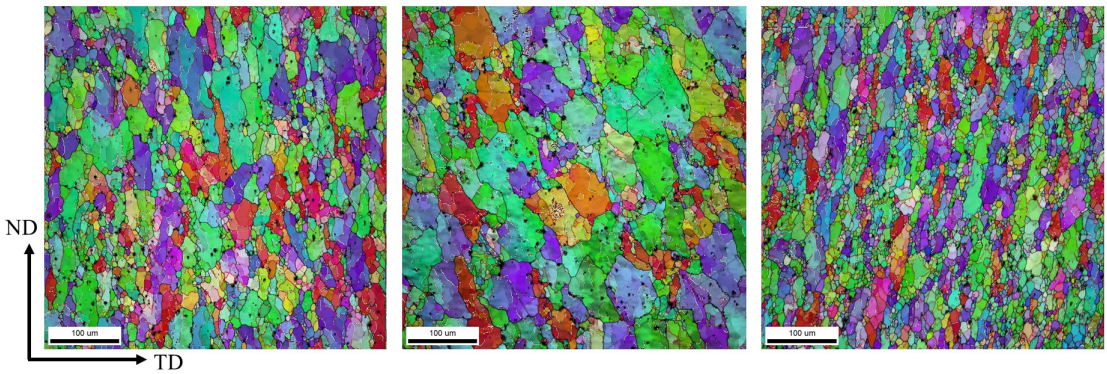

Figure 4.36: High resolution IPF with marked grain boundaries taken at 200x of the first edge (first image), middle (second image) and second edge (third image) specimens.

4.5.2 The PFs of the 7108 massive extruded profile

The pole figures of the middle and edge specimens from the massive extruded profile is presented below. Figure 4.38 show that the middle specimen is mostly axis-symmetric with little noise, due to the distinct orientations. Both the 111 and 001 pole figures show the projections of the ⟨111⟩ and ⟨001⟩ fibre components. In comparison the pole figures taken from the edges, seen in Figure 4.37 and Figure 4.39 indicate the presence of ⟨111⟩ and ⟨001⟩ fibre components, however these pole figures are noisier and less symmetric.

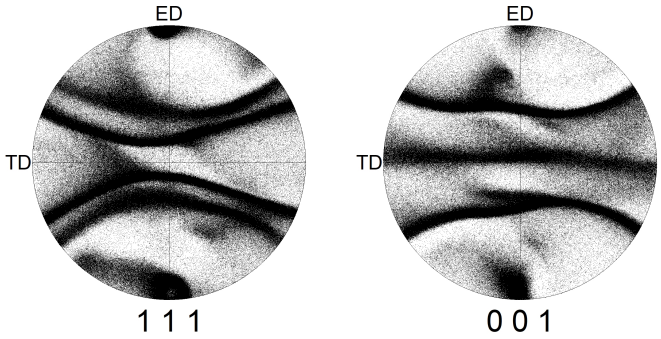

Figure 4.37: The 111 and 001 pole figures of the first edge.

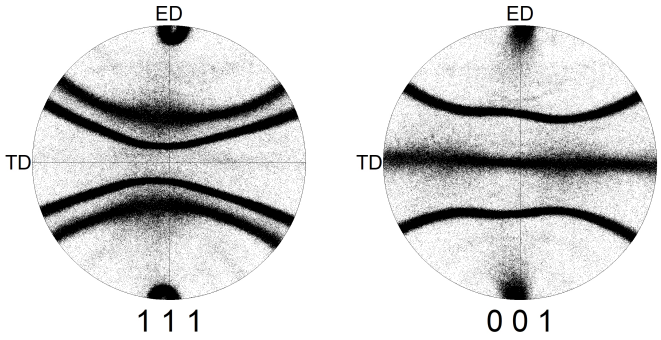

Figure 4.38: The 111 and 001 pole figures of the middle.

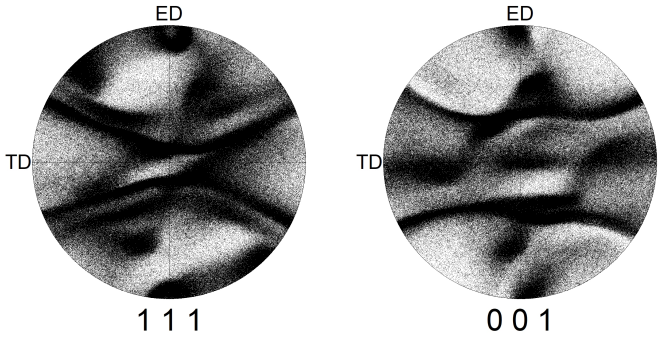

Figure 4.39: The 111 and 001 pole figures of the second edge.

4.6 Incremental elongation testing

In the chapters 4.6 through 4.9 the data from the incremental elongation of the 6082 and 7003 grade specimens and further analysis of the resulting fracture surfaces of chosen specimens are presented. The analysis were mainly done of the 7003 specimens and include SE and BSE imaging of the fracture surfaces, EDS analysis of particles found in the fracture surfaces and resulting IPF maps and pole figures from EBSD scans done on the material of the massive extruded profile.

4.6.1 Incremental elongation testing and tensile testing of the solutionized 6082 aluminium specimens

In the section below the results for the incremental elongation testing of three solutionized 6082 specimens done at the strain rates 0,05, 0,07 and 0,1 s^{-1} are presented graphically in the form of a stress-time curve and a strain-time curve, shown in Figure 4.40 and 4.41. A stress-strain curve from a tensile test done on a solutionized 6082 specimen is shown in Figure 4.42 for a comparison.

The stress-time curves show incremental steps as the specimens are elongated, with signs of various degrees of overshooting on each step. The overshooting increases with increasing stress and elongation. The slope of the curves also evens out as the stress and elongation increases, and the maximum stress reached is around 200 MPa, which is similar to peak stress of 208,1 MPa of the tensile specimen. Between 250 seconds and 350 seconds the stress starts to decrease drastically for all three specimens, however they do not fracture, but the stress incrementally decreases as the cross section area decreases as the result of slip along visible bands in the specimen surface.

The strain-time curve mainly show the elongation of the specimen. Other than for elongation there appear to be little difference between the three strain rates. The lowest strain rate at 0,05 s^{-1} results in the most strain, while the second lowest strain rate at 0,07 s^{-1} results in the least strain. However, in all cases these specimens achieve a greater strain then the tensile specimen. The uniform strain was equal to the strain at break at 0,119 mm/mm for the tensile specimen, compared to the total achieved strain 0,507 mm/mm which was the largest strain achieved in the incremental elongation testing of the 6082 specimens. The strain prior to the significant drop in stress, at around 300 seconds, seen in the stress-time curve is 0,436 mm/mm. The stress-strain curve is also serrated, with a short drop at the end.

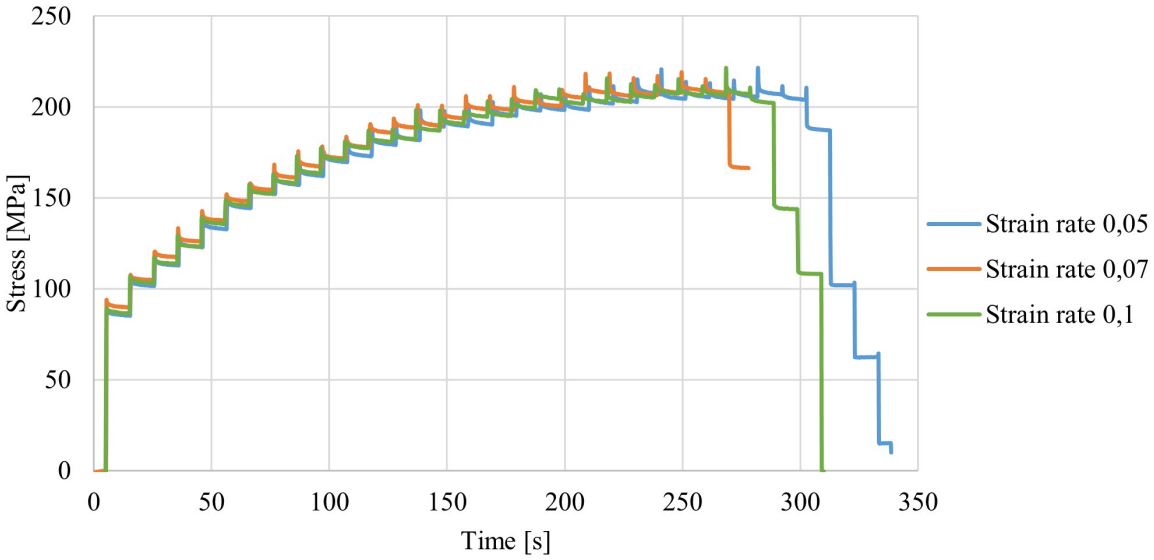

Figure 4.40: Nominal stress-time curve from the incremental elongation tests of the solutionized 6082 specimens at the strain rates 0,05, 0,07 and 0,1 s^{-1}.

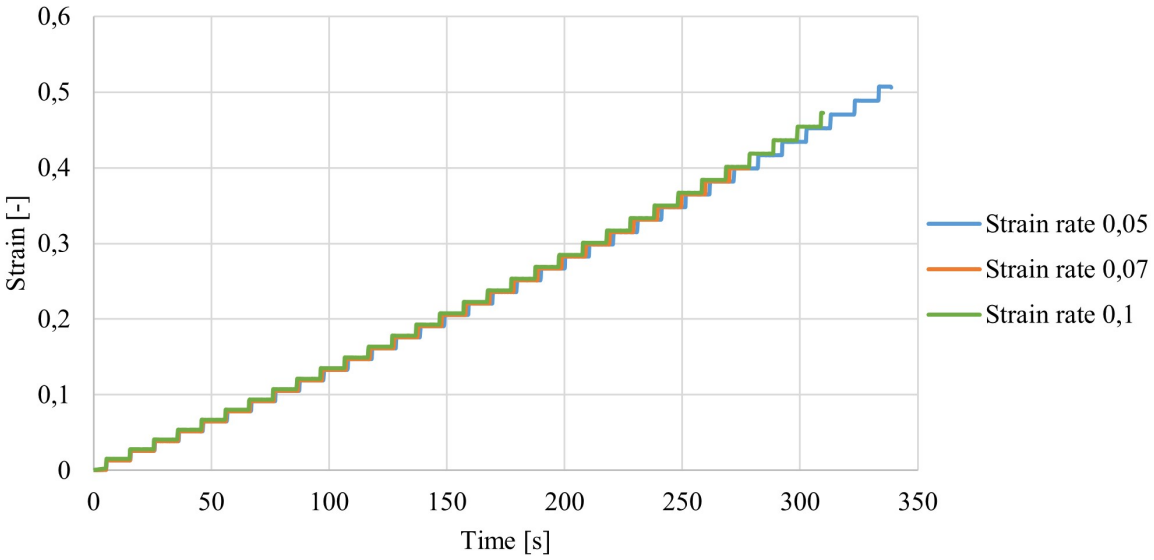

Figure 4.41: Nominal strain-time curve from the incremental elongation tests of the solutionized 6082 specimens at the strain rates 0,05, 0,07 and 0,1 s^{-1}.

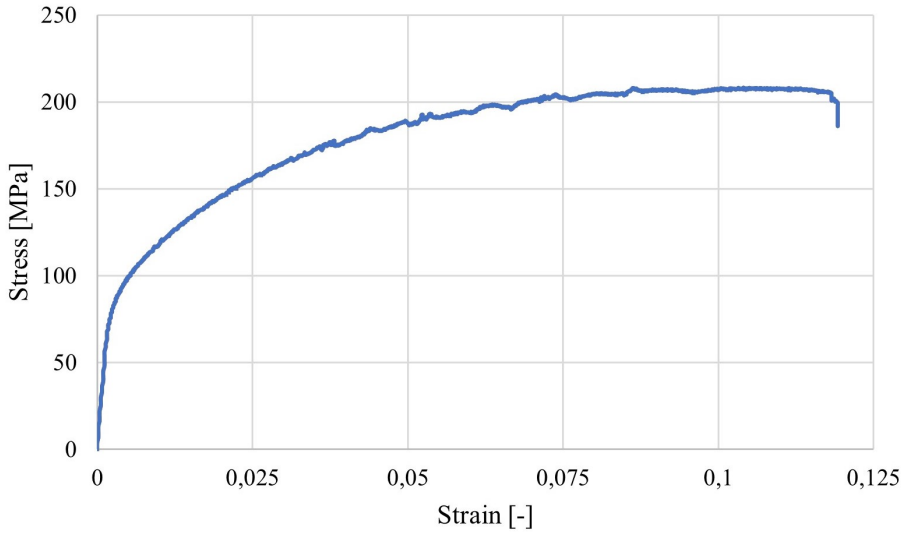

Figure 4.42: The nominal stress-strain curve of a solutionized 6082 specimen.

4.6.2 Incremental elongation testing and tensile testing of the solutionized 7003 aluminium specimens

In the section below the results for the incremental elongation testing of three solutionized 7003 specimens done at the strain rates 0,05, 0,07 and 0,1 s^{-1} are presented graphically in the form of a stress-time curve and a strain-time curve, shown in Figure 4.43 and 4.44. A stress-strain curve from a tensile test done on a solutionized 7003 specimen is shown in Figure 4.45 as a comparison.

Similar as to the 6082 specimens the stress-time curves for the 7003 specimens show incremental steps as the specimens are elongated, with signs of various degrees of overshooting on each step. The overshooting increases with increasing stress and elongation. The slope of the curves also evens out as the stress and elongation increases, and the maximum stress reached is a little under 200 MPa, which is similar to peak stress of the tensile specimen at 201,1 MPa. Between 350 seconds and 450 seconds the stress starts to decrease drastically for all three specimens, however they do not fracture, but the stress incrementally decreases as the cross section area decreases as the result of slip along visible bands in the specimen surface.

The strain-time curve mainly show the elongation of the specimen. Other than for elongation there appear to be little difference between the three strain rates. The highest strain rate at 0,1 s^{-1} results in the most strain and the lower strain rates gave similar results. However, in all cases the 7003 specimens also achieved a greater strain then the tensile specimen where the uniform strain was 0,1 mm/mm, compared to 0,750 mm/mm which was the largest strain achieved in the incremental elongation testing. The strain prior to the significant drop in stress, at around 400 seconds, seen in the stress-time curve is 0,546 mm/mm. The stress-strain curve is also serrated, and show a gradual reduction in stress

as the cross section area decreases as the result of slip along visible bands in the specimen surface, similar as what occurred during the incremental elongation testing.

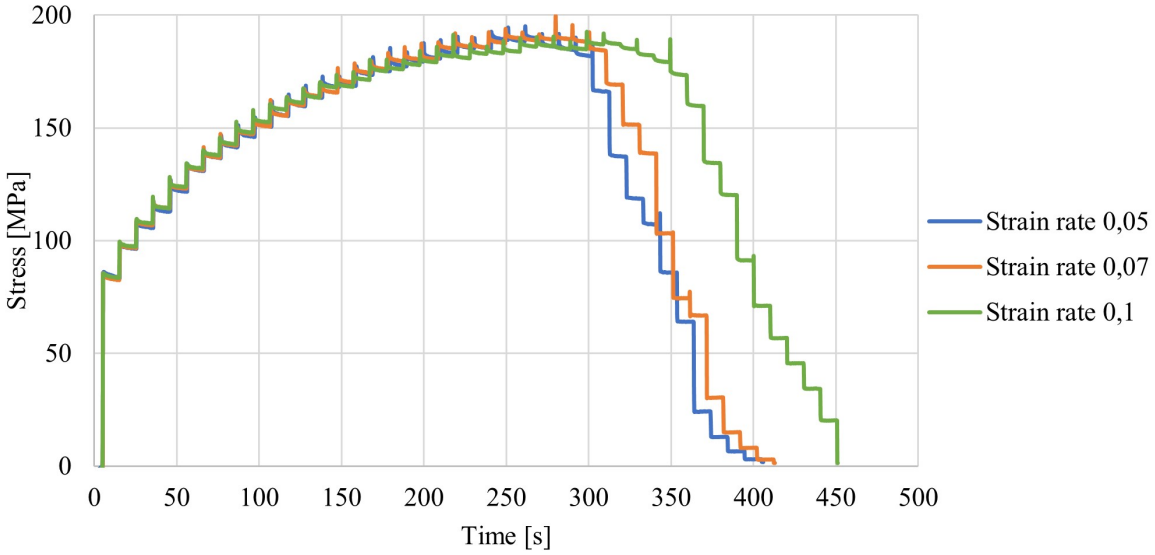

Figure 4.43: Nominal stress-time curve from the incremental elongation tests of the solutionized 7003 specimens at the strain rates 0,05, 0,07 and 0,1 s^{-1}.

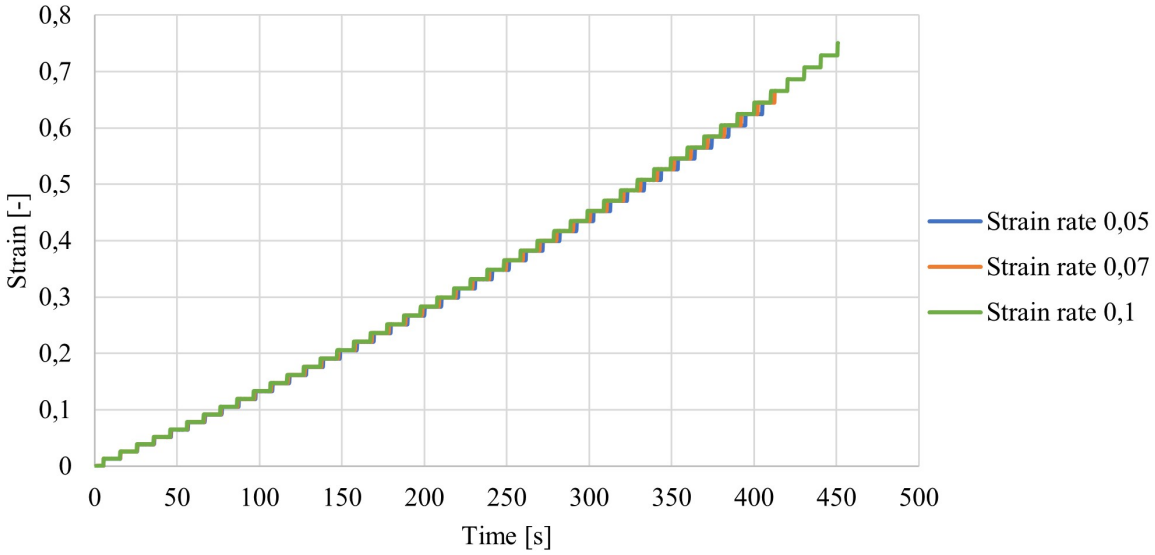

Figure 4.44: Nominal strain-time curve from the incremental elongation tests of the solutionized 7003 specimens at the strain rates 0,05, 0,07 and 0,1 s^{-1}.

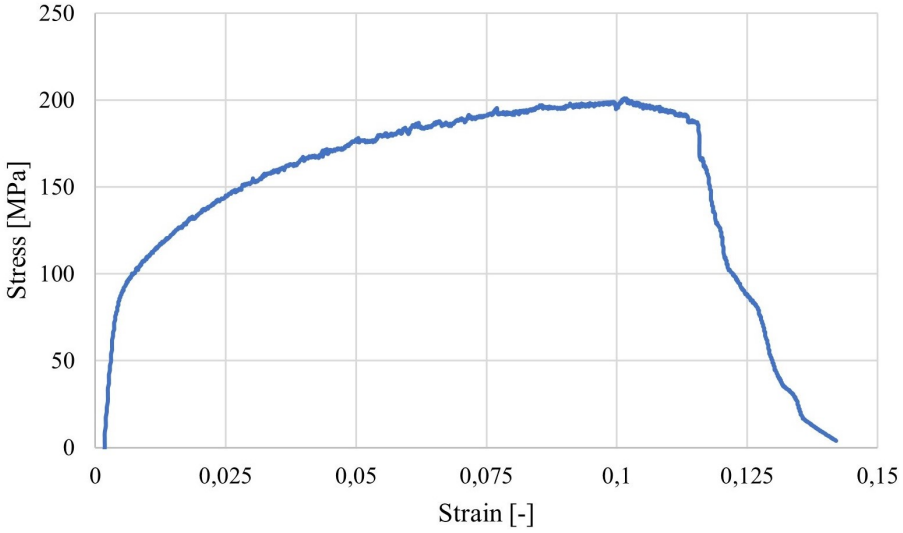

Figure 4.45: The nominal stress-strain curve of a solutionized 7003 specimen.

4.7 SE and BSE imaging of fracture surface of 7003 specimen from incremental tensile testing

The results from the SE and BSE imaging of the fracture surface of a 7003 specimen from the incremental elongation testing are presented below. These images cover both topographical characteristics of the fracture surfaces and particles found on the surfaces, enhanced by atomic number contrast.

Figure 4.46 presents an overview of the fracture surface using SE imaging at 100x. Across the surface two lines are visible, corresponding to two lines visible at the side of the specimen as well. The images in Figure 4.47 show more detailed images of the bands, as well as the dimpled areas around and between them.

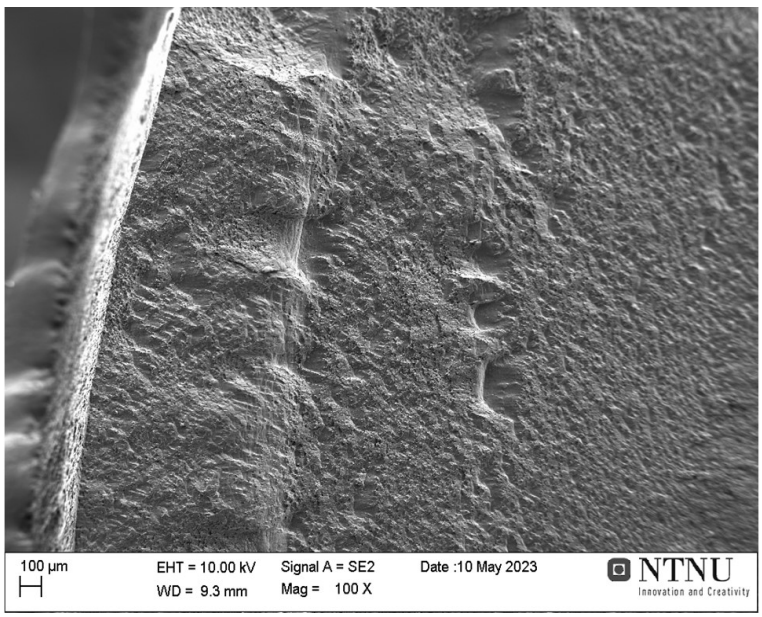

Figure 4.46: Secondary electron images of the fracture surface of the 7003 specimen at 100x.

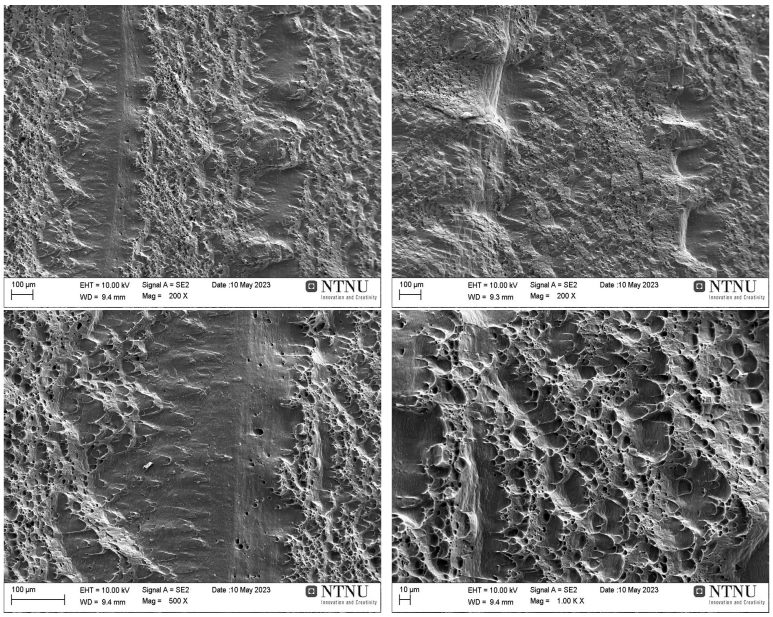

Figure 4.47: Secondary electron images of the lines and dimpled areas on the fracture surface of the 7003 specimen at 200x, 500x and 1k x.

The images taken around the bands show mostly dimples. They vary in sizes between 10 and 20 µm down to smaller dimples of only a few micrometers. This is evident from the top two SE images in Figure 4.48 at 5k x and 10k x. The BSE images show that in several of the dimples there are one or more particles embedded in the matrix there. The particles are lighter in color compared to the matrix indicating they consist of heavier elements. This is further covered in Chapter 4.8.

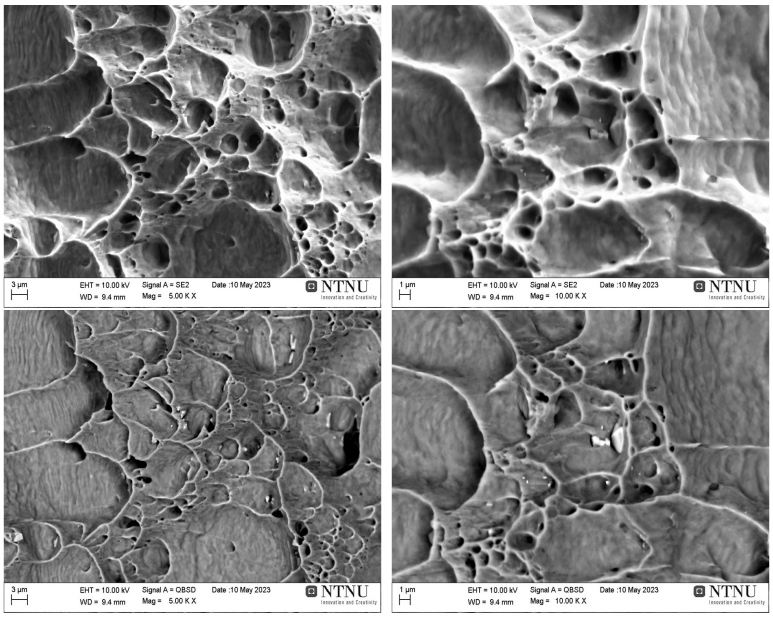

Figure 4.48: Secondary and backscatter electron images of the fracture surface 7003 specimen at 5k x and 10k x.

4.8 EDS analysis of particles in fracture surface of 7003 incremental elongation specimen

This EDS analysis is a further investigation of the particles observed in the fracture surfaces in Chapter 4.7. The results from the scans below are presented first with a BSE image at 10k x where the scanned points are marked. The first point is always of the matrix, while the following points are of the particles. The scan belonging to each point is then shown below, and at the end a table presents the weight percentages of all the elements found in each point.

Figure 4.49 shows the reference image for the scanned points on the fracture surface. Figures 4.50 to 4.53 show the corresponding scans.

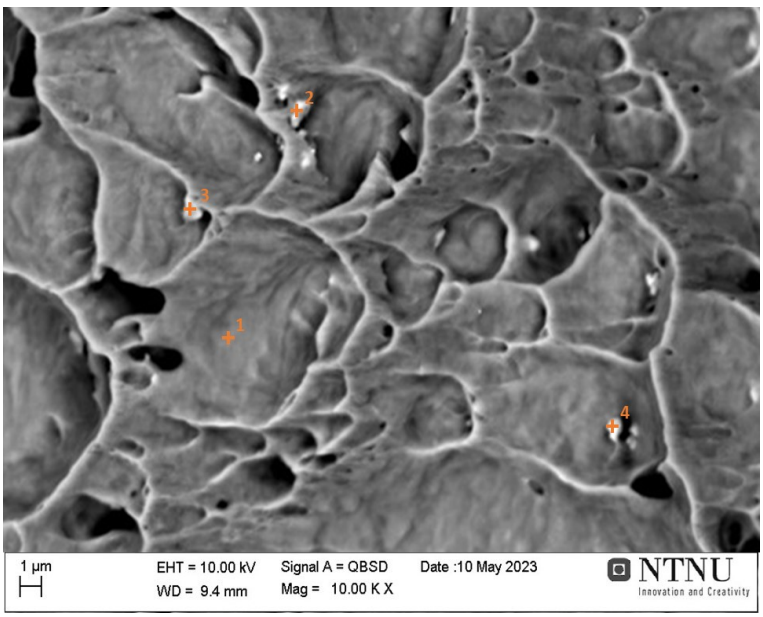

Figure 4.49: The reference image showing the 4 points scanned during the EDS analysis of the fracture surface of the 7003 specimen.

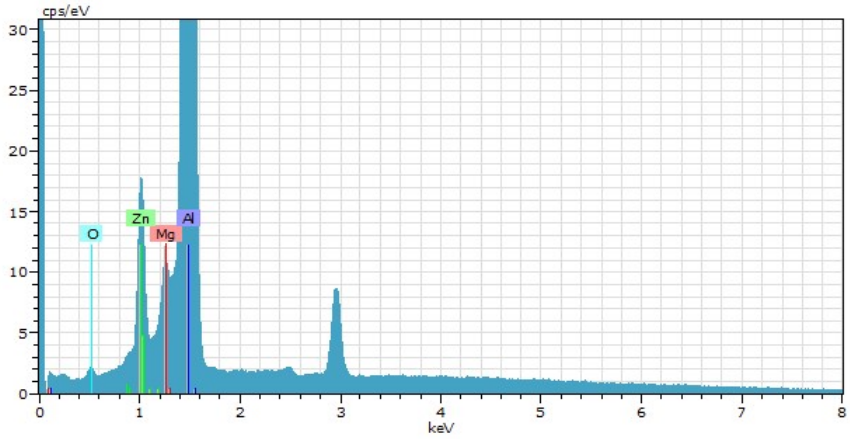

Figure 4.50: The EDS scan of point 1 in the 7003 specimen, corresponding to the matrix. The colored elements show the elements found in this point and what peaks they represent.

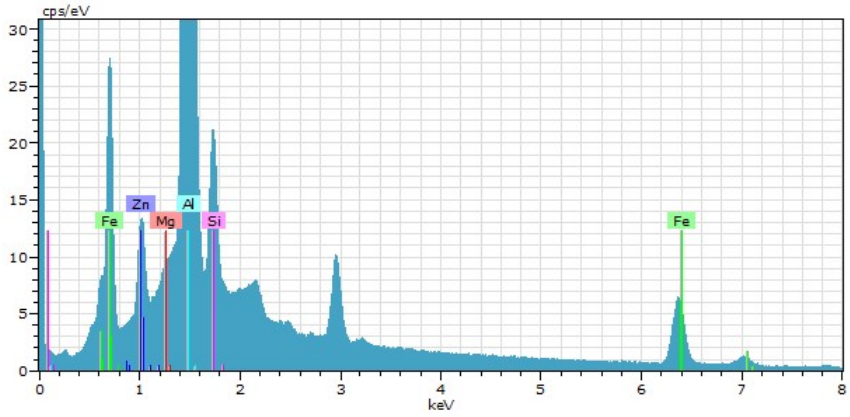

Figure 4.51: The EDS scan of point 2 in the 7003 specimen. The colored elements show the elements found in this point and what peaks they represent.

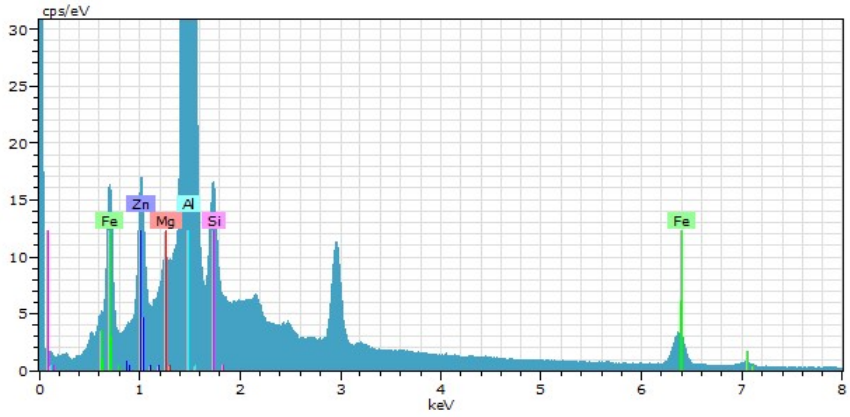

Figure 4.52: The EDS scan of point 3 in the 7003 specimen. The colored elements show the elements found in this point and what peaks they represent.

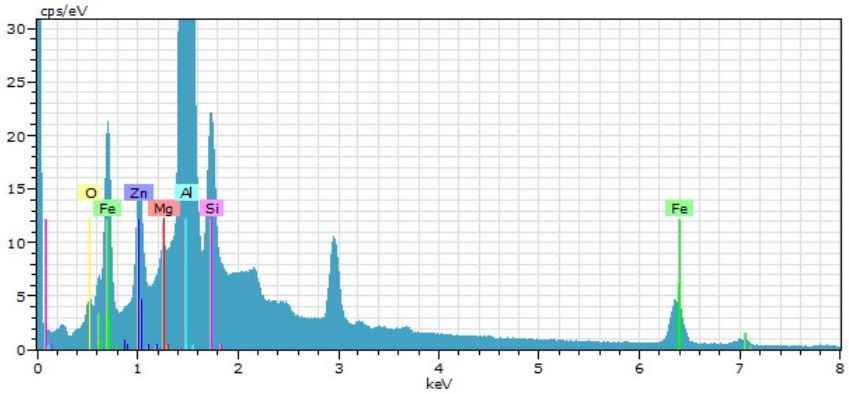

Figure 4.53: The EDS scan of point 4 in the 7003 specimen. The colored elements show the elements found in this point and what peaks they represent.

Table 4.7 summarizes what elements were found in each point, as well as the weight percentages of each element. Point 1, which was of the matrix, mainly contain Al, Zn, Mg and O, with the highest content being of aluminium at 60,19 wt%. The particles in point 2-4 all contain Al, Zn and Mg, but also larger weight percentages of Fe and Si. Of the particles only point 4 also contain O.

Table 4.7: Weight percentages of elements detected in the 4 points scanned in the EDS analysis of the 7003 specimen.

	1	2	3	4
Al [wt%]	60,19	48,53	50,63	48,34
Zn [wt%]	2,15	2,17	2,66	2,64
Mg [wt%]	0,62	0,57	0,63	0,61
Fe [wt%]	-	26,17	13,68	20
Si [wt%]	-	3,93	3,21	4,53
O [wt%]	0,11	-	-	0,16

Figure 4.54 shows the reference image for the scanned points on the fracture surface. Figures 4.55 to 4.58 show the corresponding scans.

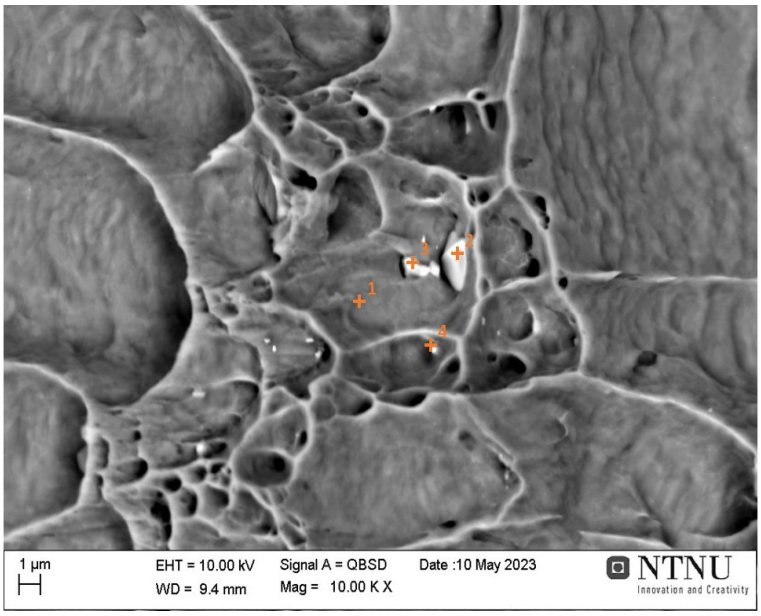

Figure 4.54: The reference image showing the 4 points scanned during the EDS analysis of the fracture surface of the 7003 specimen.

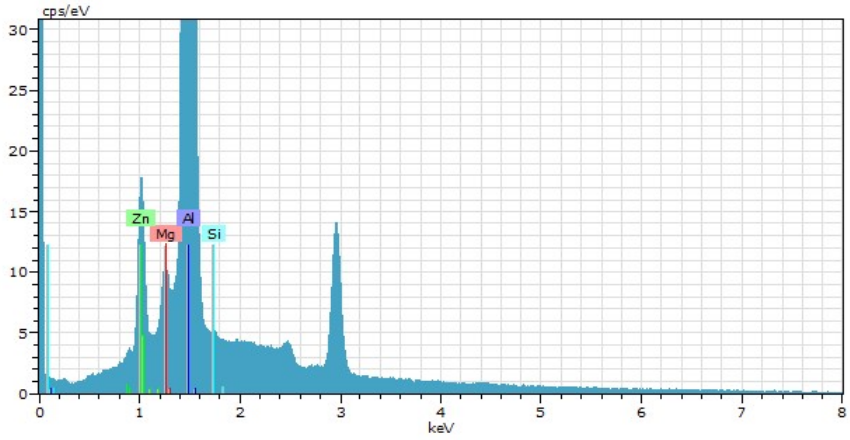

Figure 4.55: The EDS scan of point 1 in the 7003 specimen, corresponding to the matrix. The colored elements show the elements found in this point and what peaks they represent.

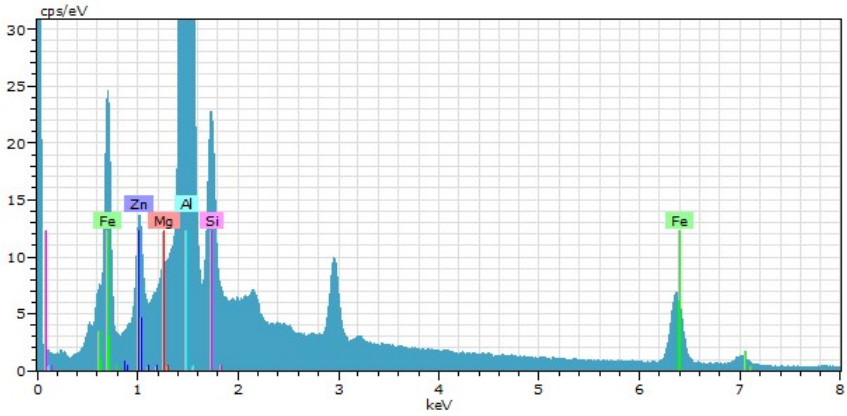

Figure 4.56: The EDS scan of point 2 in the 7003 specimen. The colored elements show the elements found in this point and what peaks they represent.

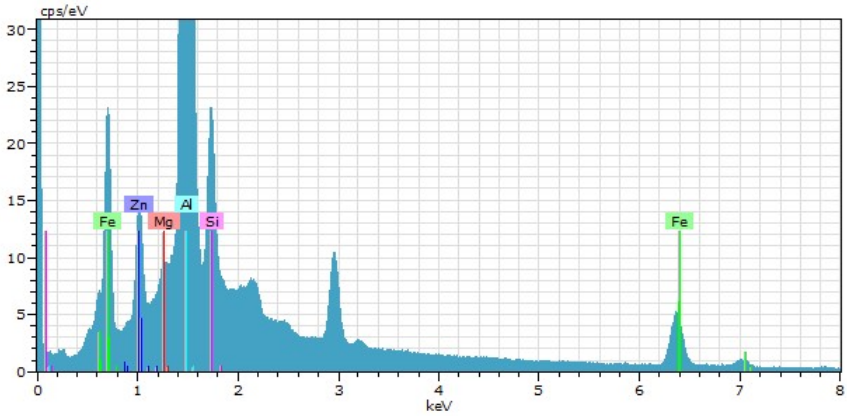

Figure 4.57: The EDS scan of point 3 in the 7003 specimen. The colored elements show the elements found in this point and what peaks they represent.

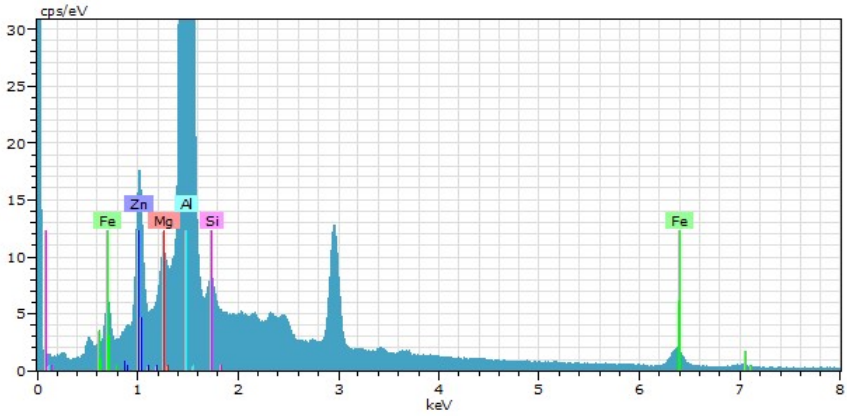

Figure 4.58: The EDS scan of point 4 in the 7003 specimen. The colored elements show the elements found in this point and what peaks they represent.

Table 4.8 summarizes what elements were found in each point, as well as the weight

percentages of each element. Point 1, which was of the matrix, mainly contain Al, Zn, Mg and Si, with the highest content being of aluminium at 54,47 wt%. The particles in point 2-4 all contain Al, Zn and Mg, but also Fe larger weight percentages of Si.

Table 4.8: Weight percentages of elements detected in the 4 points scanned in the EDS analysis of the 7003 specimen.

	1	2	3	4
Al [wt%]	54,47	45,25	49,01	53,05
Zn [wt%]	2,78	1,73	2,64	2,95
Mg [wt%]	0,78	0,4	0,63	0,77
Fe [wt%]	-	26,05	22,77	8,11
Si [wt%]	1,02	3,68	4,75	1,61
O [wt%]	-	-	-	-

4.9 Inverse pole figure maps and pole figures from material used in incremental elongation testing

The results of the EBSD analyses of the 6082 round extruded profile and the 7003 flat extruded profile are presented below. For each alloy they are first depicted in the form of IPF maps showing low resolution images of the distributions of grains and their orientation with respect to the reference triangle in Figure 4.34. For all IPF maps below the projection axis is the ND direction. Next the 111 and 001 pole figures are presented.

4.9.1 6082 round profile

The IPF map in Figure 4.59 show the distribution of reflected planes in the 8082 round extruded profile. The pole figures in Figure 4.60 show the specimen is axis-symmetric with both the $\langle 111 \rangle$ and $\langle 001 \rangle$ fibre components present.

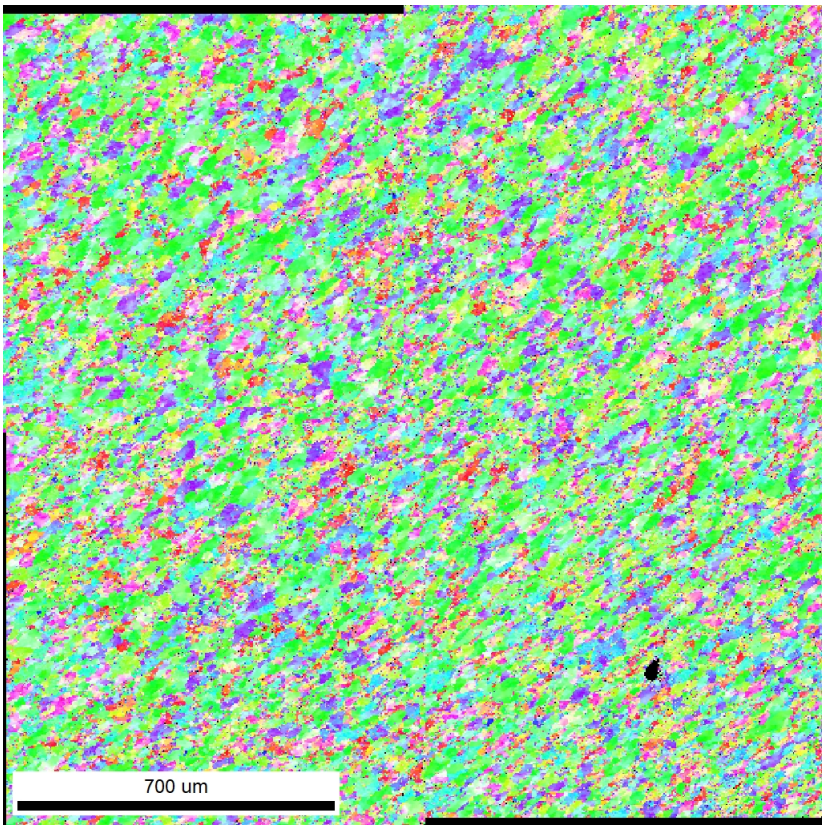

Figure 4.59: Low resolution IPF map of the 6082 round profile.

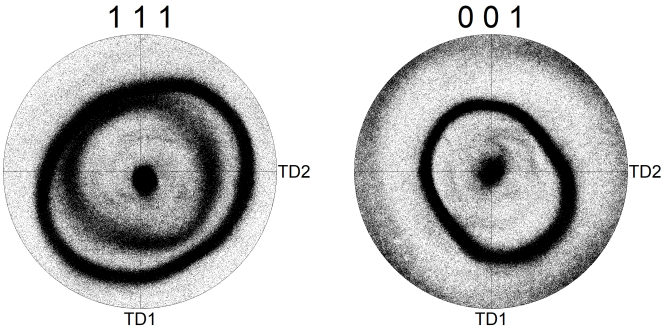

Figure 4.60: The axis-symmetric 111 and 001 pole figures of the 6082 round profile.

4.9.2 7003 flat extruded profile

The IPF map in Figure 4.61 show the distribution of reflected planes in the 7003 flat extruded profile. The pole figures in Figure 4.62 show that both the S and Brass texture components are present, with some lesser signs of Cu.

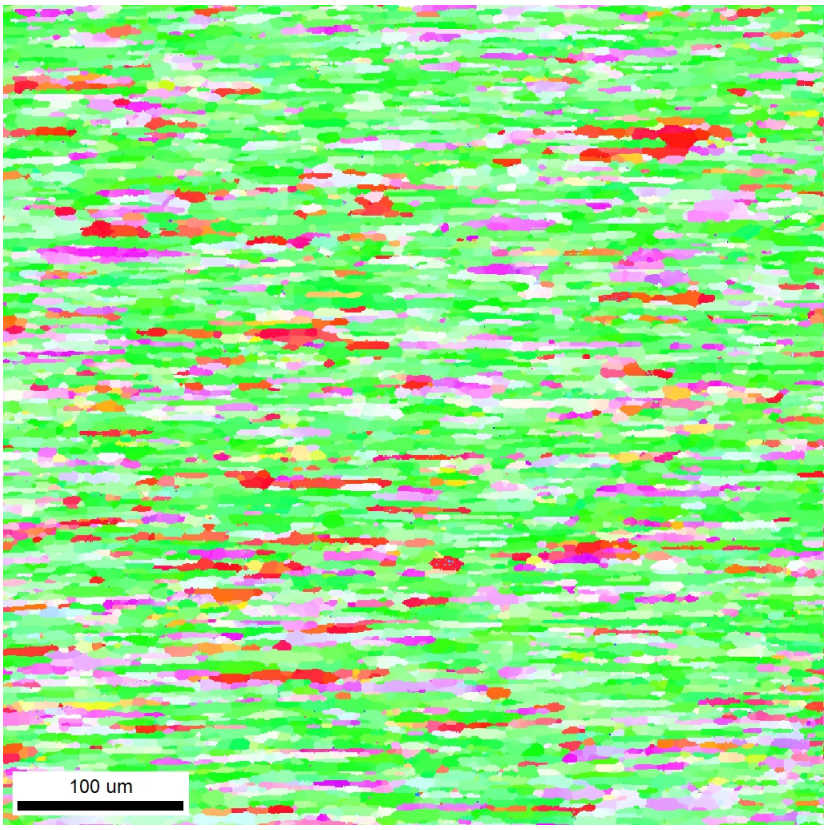

Figure 4.61: Low resolution IPF taken at 200x of the 7003 flat extruded profile.

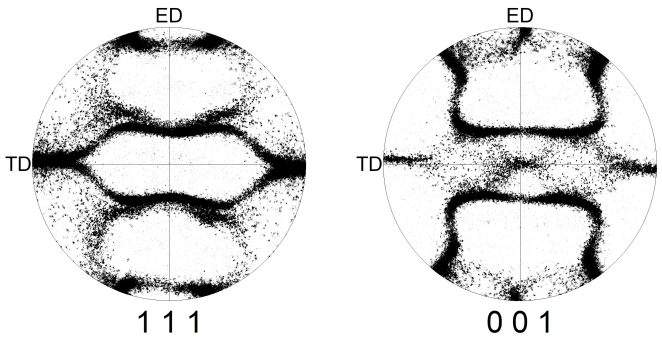

Figure 4.62: The 111 and 001 pole figures of the 7003 flat extruded profile.

Chapter 5

Discussion

This chapter of the report will discuss the results from the tensile tests and the incremental elongation tests. The main motives are to determine the potential fracture modes on a microscopic level, potential causes of the fractures and why they are slant fractures. The different specimens discussed in the tensile test chapter are the edge and middle specimens from the 7108 massive extruded profile and the square and rectangular specimens from the 7108 flat extruded profile. For the sake of simplicity they will also here be referred to as the edge, middle, square and rectangular specimens. The specimens discussed in the incremental elongation chapter will be referred to as the 7003 specimens and the 6082 specimens.

5.1 Identification of fracture modes in tensile specimens from 7108 massive extruded profile and flat extruded profile

All specimens from the tensile tests experienced some form of slant fracture, at approximately 45° to the tensile axis. The angle of the fractures were mainly along the ND-ED plane of the edge, square and rectangle specimens, and along the ED-TD plane of middle specimens. Microscopically the fracture surfaces of the different specimens also seemed to show somewhat different characteristics, which will be discussed in order to try to determine the fracture modes.

5.1.1 The fracture of edge specimens

From the light optical microscopy images in Figures 4.5 and 4.6 the profile of the fracture appear smooth and with few irregularities along the edge. Together with the thin region of deformation in the grains, emphasized for one grain in Figure 5.1, this indicate that the grains were sheared off due to a greater amount of dislocation activity in this region,

which is typical for ductile fractures. This could allow for both the creation and growth of voids, rather than crack growth along grain boundaries and crystal planes [24, 46].

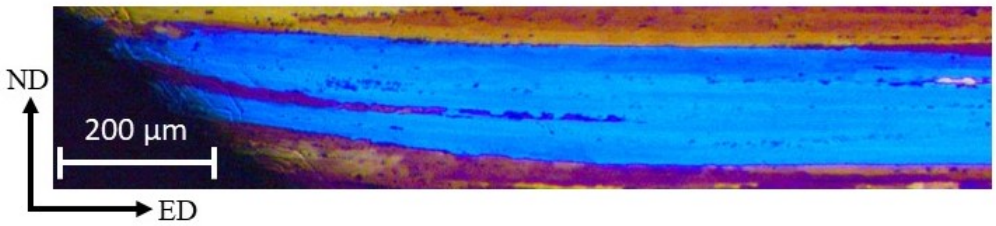

Figure 5.1: The deformed region of a grain near the edge of the fracture surface.

The suggestion that the fracture has a ductile characteristic is further supported by the SE images in Figure 4.10 that show a heavily dimpled surface at higher magnifications, likely caused by the nucleation and growth of voids. The BSE images in Figure 4.10 show that several dimples have particles embedded in them, and they are probably where voids were nucleated [24, 47]. These particles and their impact will be further discussed in Chapter 5.2. This is similar to what Raju et al. [47] observed in the 7010 fracture test specimens where the fracture surfaces appeared dimpled when using SE imaging, and these were ductile fractures.

The dimples in the surface vary in size with the larger ones being around 10 µm in diameter. Some of the flatter regions appear to be the bottoms of larger dimples, while others are surfaces where some form of deformation have occurred in the direction of the shear stress based on the shape and orientation of the irregularities in Figure 5.2. Overall this does indicate a ductile fracture mode.

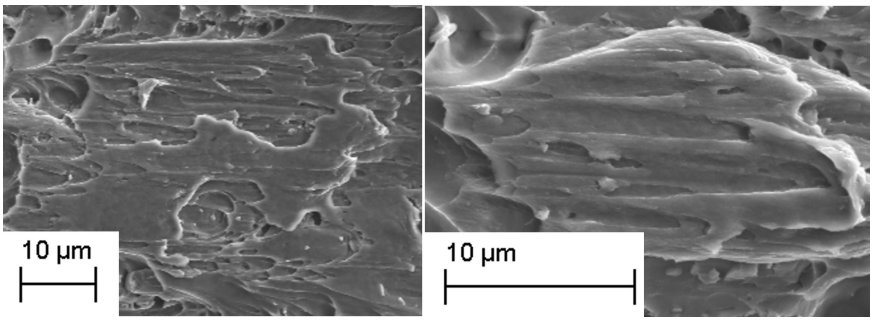

Figure 5.2: Flatter regions seen on the edge specimen fracture surface with irregularities in the surface.

Despite the apparent ductile character of the fracture surface there is no visible sign of diffuse necking in the specimens which is a common characteristic for ductile materials [33]. This is further observed in the nominal stress-strain curves from Figure 4.1. They show no sign of local deformation as they fracture at the ultimate tensile stress before necking is initiated [33]. This seems to be typical of the early slant ductile fractures, with

no visible necking and a fracture surface with a ductile characteristic.

5.1.2 The fracture of middle specimens

The fracture mode of the middle specimen is more difficult to determine accurately. Based on both the light optical microscopy images from Figures 4.7 and 4.8 and the SE images from Figures 4.11 to 4.14 the fracture lean towards having a brittle character [24, 49, 50]. However, weather the crack propagation was intergranular or transgranular is less obvious. The light optical microscopy images show small steps along the fracture's edge indicating some crack growth along the grain boundaries, as each step consists of one or more grains as seen in Figure 5.3. This is similar to what Pedersen et al. [49] observed in the 7075 specimen from Figure 2.31.

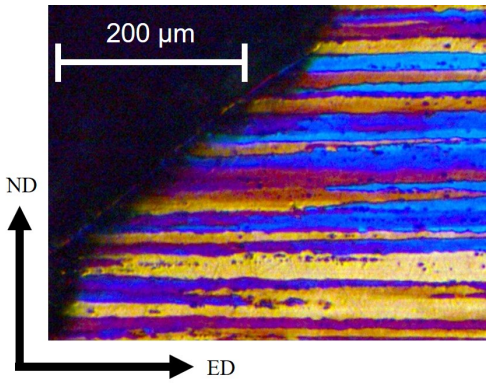

Figure 5.3: The steps seen at the fracture edge of a middle specimen.

Although the light microscopy images show similar characteristics to those of Pedersen et al. [49] the SE images are somewhat different. Pedersen et al. [49] observed intergranular fractures showing as grain boundary facets with dimpled surfaces in between where the grain cross sections had sheared off. Here however, the middle specimen show mostly flat, faceted areas, with some but few dimpled regions found in the more level part of the fracture surface. The steeper regions show even less signs of dimples, but in the second image in Figure 4.14 small ripples across the flat areas of the surface can be seen. These are similar to river lines sometimes observed along the facets of transgranular fractures where cracks have propagated parallel to each other before recombining through shear or a secondary crack, resulting in these types of markings [24].

The BSE images in Figure 4.12 and Figure 4.13 show particles embedded in the dimples found, but also protruding from the flatter areas. This is similar to what Pedersen et al. [49] observed, however the BSE image of his specimen show more particles than the images of the 7108 middle specimen. Xu et al. [50] reported a case where he described one of the fracture surfaces to show both intergranular and transgranular cracks in addition to some areas containing dimples, seen in Figure 2.32 b). However the fracture surface of the middle specimen show little resemblance to this image as well, with fewer and smaller

regions containing dimples. This could indicate a more brittle character for the middle specimen compared to those analyzed by Pedersen et al. [49] and Xu et al. [50], although it should be taken into consideration that they both studied a 7075 grade alloy and not 7108.

A potential fracture mode for these specimens is a mixed one, consisting of intergranular crack propagation along grain boundaries and then transgranular cracks across the grain cross sections, rather than shear. Since some dimpled areas where found it is posible that both transgranular crack propagation and shear is responsible for breaking off the grains, although this is uncertain. Another suggestion could be that the voids that nucleated and grew in these regions became the points of crack initiation that later propagated as transgranular and intergranular cracks.

As with the edge specimen the middle specimen also show little signs of local deformation on a macroscopic level, although some greater degree of deformation is observed around the fracture area in the first image in Figure 4.7. Only the specimen Middle 1 from the stress-strain curves in Figure 4.1 show some indication of local deformation where the curve slopes somewhat down before fracture [33]. This was however not visibly evident in the corresponding specimen.

Finally it is worth doing a quick comparison of the light optical microscopy images of the edge and middle specimen in terms of visible grain size. As seen in Figure 5.4, all relative to the scale bar below, the grains in the edge specimen, a), are noticeably larger compared to those of the middle specimen, b) and c). These are both smaller and had variation within the specimen compared to the edge specimen, however the seemingly thin grains seen in b) could be due to poor preparation of the specimen. The size difference could be related to the direction of the crack and where the specimens were taken from the plate. The edge specimen was taken from further towards the edge of the plate cut from the massive extruded profile. During extrusion the edges of the profile likely deformed differently compared to the middle of the profile, leaving the outer sections with flatter grains and the middle with more axis symmetric grains along the normal and transverse directions [25, 26].

Since the edge specimen fractured with the slant fracture angle across the ND-ED plane, see Figure 3.6 for reference, and the transverse direction would be a region where the grains are wider parallel to the normal direction, this could be the cause of why the grains are seen as larger here than in the middle specimen. In comparison the middle specimen is taken from an area with supposedly more axis-symmetric grains, meaning the orientation of the fracture is irrelevant for how the grain size is perceived. The IPF maps in Figure 4.36 that show the grain boundaries indicate some elongated grains closer to the edges, but also a lot of smaller grains, although these are of such small regions that they do not say much about the hole surface of the edge specimens. However, the only way to confirm this for both specimens would be to analyse them from the other direction as well.

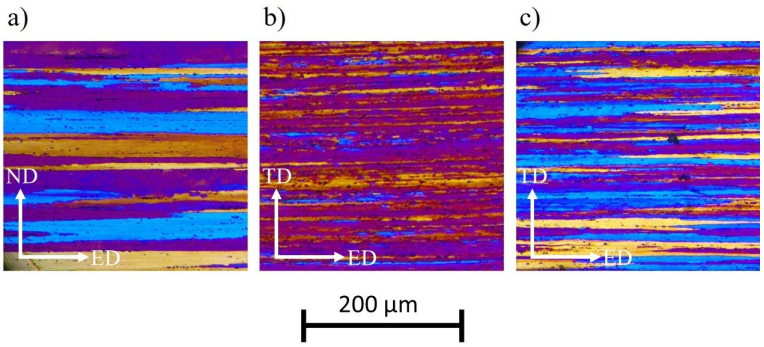

Figure 5.4: The variation in grain size between a) the edge specimen at 5 x and b-c) middle specimen at 5 x.

5.1.3 The fracture of the square and rectangular specimens

Similarly to that of the middle specimen the rectangular one show some signs of steps along the fracture profile in the light optical microscopy images from Figure 4.9. However, this is not as evident partially due to the poor anodizing, and the character of the fracture would more accurately be determined using the SEM images. Then it can also be compared to the square specimen which was not studied using light optical microscopy.

Based on the images in Figures 4.15 and 4.17 the fracture surfaces of both the square and rectangular specimens seem to consist of large, smooth facets resembling steps covering large regions, with dimples covering separate areas or surrounding some of the step-like structures. What can be observed from Figures 4.15, 4.16, 4.17 and 4.18 is similar to what Pedersen et al. [49] found on the fracture surface of the 7075 specimens, which he suggested was an intergranular fracture with sheared off grains resulting in a brittle-ductile character.

With the square and rectangular specimens being taken from a flat extruded profile these microscopic steps can be said to resemble the assumed grain shape of the specimen, as the shape tends to resemble the macroscopic shape of the profile [25]. This further validates the suggestion of this being an intergranular fracture with some ductile character. The BSE image in Figure 5.5 show particles lining one of the steps of the rectangular specimen. A potential reason for this could be that the cross section of this step is dimpled and that these particles are where voids were nucleated, leading to void growth and eventually coalescence [24, 49, 50]. Another suggestion is that these regions are grain boundaries and that these particles have formed along them in some areas, eventually initiating a micro crack that further led to crack growth. However the theory does point more to the first suggestion.

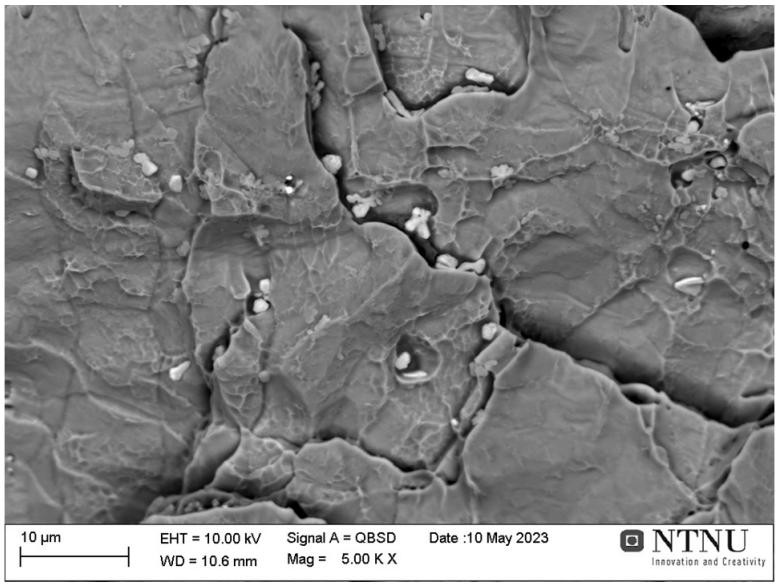

Figure 5.5: A BSE image of particles along the step-like structure of the fracture surface of the rectangular specimen.

Apart from the microscopic appearance of the square and rectangular specimens they show no visible signs of diffuse necking having occurred. This is further confirmed when viewing the nominal stress-strain curves as there is no evidence of a region of local plastic deformation [33]. It was also suspected that due to its geometry, the rectangular specimens might develop a local neck. The theoretical θ angles that were calculated for the specimens were however not observable in practise as the fractures were all fairly straight across the surface. However they still indicate that the material is anisotropic [30, 34].

5.2 Discussion around potential causes for slant fractures in specimens from the 7108 massive extruded profile and flat extruded profile

Regarding why the slant fractures occurred it is relevant to considered both what initiated the voids or cracks to begin with, eventually causing failure, and why these voids and cracks grew across the 45° angle seen in all the tensile specimens. Based on the BSE images from all the specimens, seen in Chapter 4.3, particle inclusions seem to have had a role in most of the fracture modes observed. This has already been alluded to in the previous chapter, and will be discussed further here. The second part of this chapter will focus more on the occurrence of slant fractures in all the specimens before any necking is initiated.

5.2.1 The potential effect of particles

As particles can be seen embedded in dimples and along grain steps in the BSE images because of the atomic number contrast, these likely were the causes of the formation of micro voids and/or cracks. Both Pedersen et al. [49] and Xu et al. [50] seemingly arrived at the conclusion that the particles observed in their BSE images functioned as nucleation sites for voids, at least in the dimpled regions. Raju et al. [47] made the same observation in an experiment with fracture testing of a 7010 grade alloy, that brittle intermetallic particles were the basis for void nucleation and growth. As voids also can function as micro cracks that further propagate intergranularly or transgranurarly they likely played an important role for both the ductile and brittle fracture modes in the specimens [24].

Following the discovery of the particles in the fracture surfaces of the tensile specimens an EDS analysis was done on particles found in the edge, middle and rectangular specimens. The objective was to try and determine what elements they contained in order to identify the types of particles. Already the size implies these are constituent particles rather than dispersoids which are the second largest particles expected to exist in this alloy, but are rarely bigger than a few hundred nanometers [6, 13]. The particles found on the fracture surfaces however are between 1 and 10 µm in diameter, closer to the scale of constituent particles [6, 28]. This corresponds with the results from the EDS analysis as significant amounts of iron were detected in all the particles scanned, iron typically being the main contaminant causing the precipitation of constituent particles [6, 28]. In comparison iron was not detected in the matrix in any of the specimens.

With the particles observed there are still a noticeable size variation, as pointed out in Chapter 4.4. Figure 5.6 show an example of the different particle sizes found in the edge specimen. Ii et al. [28] observed two different constituent particles occurring in an Al-10Zn-2.5Mg-2.5Cu alloy, and these responded differently to extrusion. Prior to extrusion one type had broken into smaller pieces while the other type mostly maintained its size. A similar situation could explain the size variations in the particles found in the tensile

specimens, as they even resemble the ones Ii et al. [28] observed in size. That alloy did however contain more copper than the 7108 grade alloys. Liao et al. [29] concluded that the addition of copper to an Al-8Zn-1.6Mg-0.4Zr-0.03Fe alloy seemingly had little effect on the size of precipitated particles, but how it effects the properties of the constituent particles is however uncertain. Therefore it can not be said that two different types of constituents were found here. It does however offer a suggestion of a possible cause that could be investigated further. Mind that particles might also have broken during the formation of voids as this can include the breaking of particles, leading to the size variations [24]. If there are some constituents that break more easily these could have a greater effect on extruded profiles as voids might already be nucleated at their breaking during extrusion.

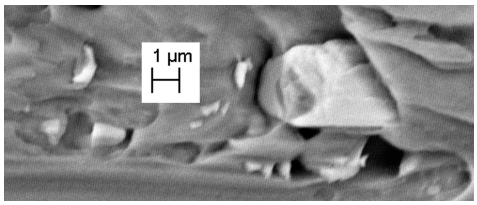

Figure 5.6: A BSE image from the edge specimen showing a larger particle surrounded by smaller particles relative to the scale bar.

While the size of the particles seen in the BSE images corresponds well to the scale of the larger dimples, there are dimples with diameters smaller than those of the smaller constituent particles. They could potentially have nucleated around dispersoids as these are the second largest precipitates expected to be in this alloy, although this has not been confirmed as no particles on this scale were identified and scanned using EDS.

When considering the fractures of the middle specimens both Pedersen et al. [49] and Xu et al. [50] pointed out that low solute concentration around the grain boundaries where the cause of the crack propagation along their 7075 grade specimens resulting in an intergranular-ductile fracture. Fourmeau et al. [22] discovered PFZs around high and low angle grain boundaries in an artificially aged 7075 grade alloy further substantiating Pedersen et al. and Xu et al.'s explanations. However as these alloys were artificially aged they can not be directly compared with the 7108 grade specimens as these were naturally aged, which help prevent or limit PFZs [21]. Mansouri et al. [23] found that the quenching rate prior to natural aging of an Al-0.71Mg-0.95Si-0.25Mn-0.2Fe alloy likely led to PFZs occurring in the air cooled specimens as precipitates were observed on the grain boundaries. This specimen also experienced a much higher localized strain around the grain boundaries during mechanical testing compared to the water quenched one, indicating that PFZs might occur in some naturally aged alloys as well.

The 7108 grade massive extruded profile was water quenched after solutionizing, however due to its thickness it is reasonable to assume that it had a lower cooling rate in the middle compared around the edges. This could have lead to the occurrence PFZs around grain

boundaries in the middle of the profile, which might explain the different fracture modes observed in the middle and edge specimens. As the edge specimens then would have had little or no PFZs there would be no softening around grain boundaries, and the main fracture mode would be ductile rather than a brittle one, consisting of void nucleation on particles followed by growth and coalescence. In comparison the middle specimens would have PFZs around grain boundaries, softening these areas and leading to intergranular fracture, with some ductile and transgranular characteristics observed as well. As some alloys experiencing PFZs get precipitates along grain boundaries, interfacial separation of such particles could also be the cause of void and/or crack nucleation [23]. Therefore the cause of crack initiation leading to fracture is less certain for the middle specimens and both constituent particles, grain boundary precipitates and the general softening of the grain boundaries might play a part. If it is the case that the middle specimens had PFZs along the grain boundaries this likely interfered with the potential effect the texture might have had on the deformation prior to fracture. Had PFZs not been present the specimens might have experienced some degree of necking prior to fracture as the hypothesis suggest, and potentially making the deformation and fracture modes more affected by texture.

5.2.2 The occurrence of slant fractures

Considering the fact that all the specimens experienced slant fractures points to some form of local plastic instability occurring in them during testing. In the Introduction it is mentioned that last year Gopal [3] investigated the cause of these slant fractures in a 7003 alloy, and could exclude strain aging and the formation of PLC bands as he tested the specimens at low temperatures and slant fractures still occurred [2]. It is therefore unlikely that PLC is the cause in these 7108 grade specimens as well. Because of the 45° angle of the fractures, along the direction of the maximum shear stress, a shear band might have formed due to a strain path change. In comparison Robinson et al. [40] found that PLC bands tend to form at around a 60 °angle, which was also the case for the angle of the fractures in the incremental elongation specimens where dynamic strain aging is in fact suspected.

Following a strain path change some materials experience an increase in flow stress while others experience a softening along this band [44, 45]. As fracture occurred in the specimens prior to necking it is possible that these experienced a softening. If that is the case this softening then led to an early fracture in the edge specimens and a ductile characteristic observable microscopically. However, in the middle specimens this softening combined with the PFZs around the grain boundaries led to an early brittle fracture. As previously alluded to, these specimens might not have failed prior to necking if not for the PFZs, and had this been the case instead the differences in texture between the middle and edge specimens could have helped explain it.

Geometry also had little effect on necking. With the rectangular specimens the aim was to see if a local neck developed. The theoretical θ angles calculated from the r-values of

each specimen showed that a local neck at between 10-20° should have developed, however the fractures showed little indication of having happened at an angle. It is possible that a local neck would have occurred had a diffuse neck first been initiated, but as the specimens fractured prior to this it is possible that the strains in the specimens were not great enough for a local neck to develop.

The results of the EBSD analysis of the 7003 specimens previously used by Gopal [3], and used here for incremental elongation testing, confirmed that they had a rolling texture as seen in Figure 4.62, where the pole figures show the typical texture components for rolled plates or flat extruded profiles [30]. The results from the EBSD analysis showed that the middle specimens had an axis-symmetric texture while the textures of edge specimens were a bit more complicated. With the edges it appears that there is some texture variation within the specimens, as is especially clear in Figure 5.7 where there is a distinct transition from a more green to a blue color. This can also be why the pole figures of the edges both show signs of the ⟨111⟩ and ⟨001⟩ fibre components typical of an axis-symmetric texture, but with indications of some different components. The additional noise seen in the pole figures could be due to more random textures or the occurrence of a shear texture, however the patterns are not distinct enough in order to determine this, likely do to the area scanned with this potential other texture being quite small compared to the total scanned area.

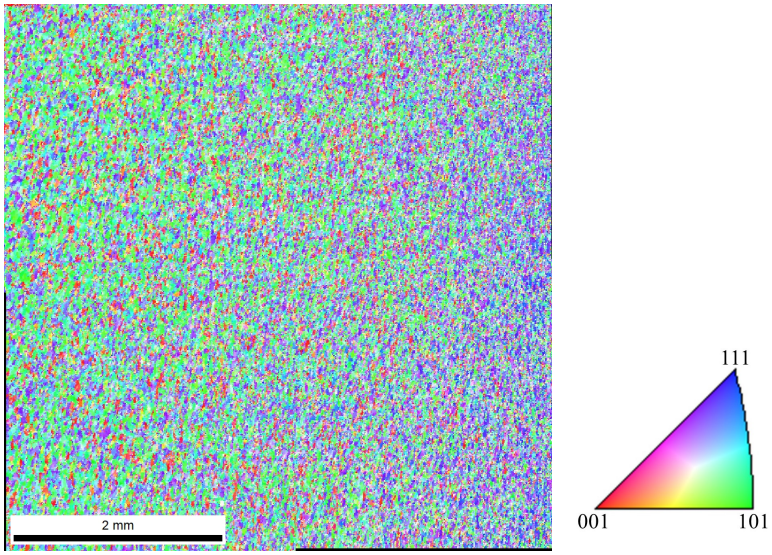

Figure 5.7: The IPF map of the second edge from the EBSD scans showing the variation in texture throughout the image. The projection axis is the ND direction and the coloring is according to the reference triangle.

This differs somewhat from the expected rolling texture, but the edge specimens still behaved as expected based on the hypothesis, allthough the potential effect of these texture differences were likely not observed in the tensile tests due to the PFZs. However, as the edge specimens appeared to have had a fairly axis-symmetric texture and yet experienced a slant ductile fracture like the 7003 specimens from the flat extruded profile that Gopal

[3] investigated, this could indicate that texture does not play a significant role in the occurrence of these slant ductile fractures. Since the alloys compositions were different and the texture of the 7108 edge specimens not entirely axis-symmetric the effect of texture on the slant fracture prior to necking still should still not be ruled out.

A difference was observed between the edge specimens and the middle specimens in terms of strength, with the middle specimens having significantly lower yield strengths and ultimate tensile strengths. This could be because of the differences in texture, with texture strengthening leading to a higher strength in the edge specimens, however the EBSD scans showed that both specimens had a fairly axis-symmetric texture. It is therefore more likely to be related to the precipitates. Zhang et al. [20] investigated the effect of cooling rate on the size and volume fraction of η' particles in 7150 and 7055 grade aluminium alloys. It was observed that size increased and volume fraction decreased with decreasing cooling rates. This was however for artificially aged alloys, whilst with naturally aged these hardening phases are not precipitated. It could however still have a coarsening effect on the existing particles, or the slow cooling rate could cause the equilibrium phase, η, to be precipitated. This would leave less solute available to form GP-zones, and with the GP-zones contributing more to strengthening than the η particles this leads to a weakening effect in the middle specimen. In addition to this, if the η particles were precipitated on the grain boundaries this could lead to PFZs around them, further substantiating the suggestion that the brittle fracture observed in the middle specimen was due to PFZs around the grain boundaries.

5.3 The achievements and limitations of incremental elongation testing

In terms of considering the strains achieved with incremental elongation testing, the uniform strain of the solutionized tensile tested specimens and the T6 aged specimens found in literature will be compared to the strain prior to the significant drop in stress for the incrementally elongated specimens. For simplicity this will also be referred to as uniform strain. The incremental elongation testing of the 6082 specimens achieved the highest uniform strain of approximately 44% at a strain rate of 0,05 s^{-1}. This is 25% more than the uniform strain achieved in the tensile test with the solutionized 6082 specimen, which is significant even considering the elongation is measured by the machine and not an extensiometre. The 6082 specimens aged to T6 and tensile tested by Ryen et al. [35] achieved 6% uniform strain, meaning the incremental elongation testing resulted in 38% more strain in comparison.

Similar results were achieved for the 7003 specimens with the greatest uniform strain of 55% being achieved at the highest strain rate, 0,1 s^{-1}. This is 45% greater than the uniform strain achieved in the tensile test with the solutionized 7003 specimen. Shah et al. [36] achieved a uniform strain of 9% in a 7003 specimen aged to T6 meaning the incremental

elongation testing resulted in 46% more strain in comparison. When comparing the stress-time curves with the stress-strain curves of the solutionized specimens for both alloys the maximum stress in the incremental elongation tests appear to be similar to that achieved in the tensile tests with the solutionized specimens, which is around 200 MPa for both the 6082 and 7003 specimens. The maximum stress here is however much lower than the ultimate tensile strength of the T6 aged 6082 and 7003 material at 339,5 and 400 MPa respectively, indicating that the strengthening effect of the incremental stretching is more similar to the strengthening of solutionized tensile test specimens [35, 36]. The stress-time curves also show a small overshooting of the stress for each increment before evening out, creating a small spike at the beginning of each stress step.

Although the strain achieved in the incremental elongation testing is high, one limitation is the apparent plastic flow instabilities occurring in the specimens resulting in the formation of thin bands, seen across the specimen surfaces, and eventually slant fracture. After the previous cyclical and incremental elongation testing done on the 6082 specimens it was concluded that this was likely due to dynamic strain aging leading to the formation of and fracture along PLC bands [4]. This is probably still the case, also for the 7003 specimens. The increase in strain rates was an attempt to avoid dynamic strain aging, but a high enough rate was not reached due to the limitation of the machine [39].

At the end of the stress-time curves the stress per increment suddenly drops significantly before eventually reaching zero at fracture. When observing the specimens at this point in the curve the stress reduction occur simultaneously as sudden slip along the bands that have spread across the surface. These bands form at an angle of about 60° to the tensile axis, similar as what Robinson et al. [40] observed when investigating strain aging. Towards the end a fracture starts spreading bit by bit before separating the two surfaces entirely. The result is a slant fracture surrounded by a somewhat reduced area due to slip along the PLC bands, leaving the surface rough and uneven.

However it is the stress-strain curves that mostly help confirm dynamic strain aging as the cause of this instability. These curves are serrated, with a small dip at the end for the 6082 specimen and with the stress sinking gradually to zero for the 7003 specimen. The serrated curves are characteristic of dynamic strain aging. Zhao et al. [43] confirmed that the addition of silicon can cause dynamic strain aging in some aluminium alloys under uni-axial tensile testing and Xu et al. [41] confirmed it could occur in some Al-Mg alloys at room temperature as well. Zhiheng et al. [42] found that Al-Cu alloys with higher solute concentrations in the matrix and higher dislocation densities increased the chance of strain aging. As both the 6082 and 7003 specimens are solutionized this leads to a high (super saturated) solute content. The overshooting seen in the stress-time curves are likely also connected to dynamic strain aging, with the initial overshoot of each step potentially being the stress required to form a PLC band followed by a sudden drop as the PLC spreads across the surface [41].

5.4 The resulting fractures after incremental elongation testing

The incremental elongation testing resulted in the specimens experiencing slant fractures. In the previous project work [4] the 6082 specimens were found to have a ductile character based on the heavily dimpled fracture surface observed using SE imaging, as seen in Figure 5.8. The SE images from that report are attached in Appendix E. For the 7003 specimen investigated in the SEM most of the surface was covered in dimples apart from where two PLC bands can be seen going across the surface. The dimples, as discussed in the previous chapters about the 7108 specimens, are characteristic of a ductile fracture mode [24, 47]. The BSE images from Figure 4.48 show particles embedded in the bottom of several of the dimples, suggesting that voids nucleated around these particles which then grew and coalesced, eventually leading to fracture. Raju et al. [47] observed the same cause for void nucleation in a fracture test of a 7010 alloy.

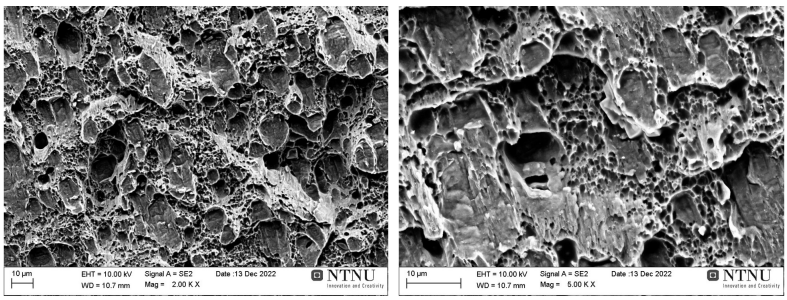

Figure 5.8: The SE images of a 6082 fracture surface after incremental elongation testing.

In comparison to the particles found in the 7108 specimens these appear to be significantly smaller, with the largest ones being around 1 µm, and the smaller being only a fraction of that size. Figure 5.9 show the variation in particle size relative to the scale bar. An EDS analysis was done of the particles, both larger and smaller. All particles scanned were found to contain a significant amount of iron compared to the matrix which contained no iron, suggesting these are constituent particles [6, 28]. Weather their sizes are due to them being smaller in nature in this alloy, or breaking of the particles during extrusion or the incremental elongation testing is difficult to determine. However these particles appear to be smaller than what the found literature suggest. The EDS analysis done on particles found in the 6082 specimens from the project work [4] also suggested that these were constituent particles, as they contained significant amounts of iron compared to the matrix. The EDS scans and table of weight percentage content is given in Appendix E.

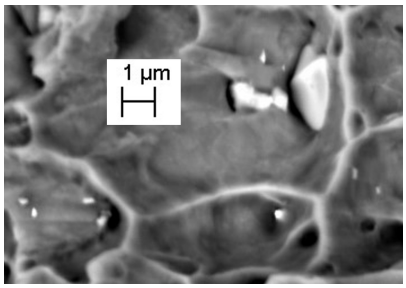

Figure 5.9: A BSE image from the 7003 specimen showing a larger particle surrounded by smaller particles relative to the scale bar.

As all the 6082 specimens and the 7003 specimens from the incremental elongation testing all experienced a strain of at least 40% it would be relevant to consider the possible damage evolution in the specimens. The SE imaging of the fracture surfaces show clear signs of voids nucleating, growing and coalescing, resulting in dimpled fracture surfaces. It is however unknown how the damage is throughout the entire specimen, or if the main damage is located in and around the PLC band where the fracture eventually occurred. If voids have been nucleated throughout the specimen then this would also be a significant limitation to the method of incremental stretching.

The EBSD scans and subsequent pole figures of the 7003 specimens show they had flat grains and rolling texture as expected. However, what potential effect texture might have had on the incremental elongation results is unknown as no 7003 specimens with different textures were tested for comparison. The same goes for the 6082 specimens, but here the texture findings say little about the specimens at all as they were from a round axis-symmetric profile, and technically only relevant for a different project.

Chapter 6

Conclusion

The tensile tests of the 7108 grade specimens led to slant fractures with no necking prior to failure in all specimens. Based on the different characteristics in the fracture surfaces of the edge, middle, square and rectangular specimens they experienced different fracture modes. The edge specimen had a ductile fracture mode based on the dimpled surface, and the middle specimen had a brittle fracture mode with signs of both intergranular, transgranular and ductile characteristics. The square and rectangular specimens had a mainly brittle fracture mode with transgranular crack propagation along the grain boundaries and ductile shear across the grains.

For the edge specimens constituent particles are assumed to be the basis for the initiation of the fractures with voids nucleating at these particles due to them cracking or separating from the matrix. These voids then grow and coalesce into cracks that eventually separate the two surfaces. For the middle specimens voids or microcracks are suspected to be initiated due to either nucleation of voids at constituent particles and/or grain boundary precipitates leading to transgranular and intergranular cracks propagating from these particles. With the rectangular specimens the particles have a combined effect of the ones mentioned above. Size and composition helped categorize these particles as constituent particles. They were quite large and EDS analysis found they contained high amounts of iron compared to the matrix where no iron was detected.

The hypothesis was that texture was related to the occurrence of the early slant ductile fractures. It was assumed that the edge specimens would have a rolling texture and that these would not experience any necking. In comparison the middle specimens would have a more axis-symmetric texture and in these necking would occur. The pole figures acquired from the EBSD scans showed that the middle specimens had a more axis-symmetric texture with both $\langle 111 \rangle$ and $\langle 001 \rangle$ fibre components present. The edge specimens also appeared to have some of these components, but also a more random, non-symmetric texture that seemingly also resulted in early slant ductile fractures with a ductile characteristic. However neither experienced any necking during tensile testing. This was the prediction for the edge specimens had they had a rolling texture, but since the texture was closer to

axis-symmetric this puts into question the effect of texture on the effect on necking. It is suggested that for the middle specimens it is due to a weakening or softening from PFZs around grain boundaries leading to early transgranular fractures.

The presence of these early slant fractures in the middle specimens is likely due to PFZs around grain boundaries, which made it difficult to determine the effect of texture on the fractures. As dynamic strain aging has previously been ruled out as the cause of these slant fractures some other form of local plastic instability could be the cause. Due to the lack of necking and the angle of the fracture it could be a strain path change leading to a softening along the direction of the maximum shear stress, creating a shear band that the cracks or voids propagate along. However this must be investigated further as it is merely an assumption.

For the incremental elongation testing both the 6082 and the 7003 specimens achieved significant strains compared to the solutionized tensile tested specimens and the T6 tensile tested specimens found in literature. With the 6082 grade specimens the largest uniform strain of 44% was achieved at the lowest strain rate, 0,05 s^{-1}, compared to 6% achieved at T6. With the 7003 specimens the largest strain of 55% was achieved at the highest strain rate, 0,1 s^{-1}, compared to 9% achieved at T6.

A severe limitation to this method was however the occurrence of dynamic strain aging, which lead to uneven strain in the specimens, a rough and uneven surface due to the PLC bands and eventually a slant fracture. These bands and fractures were assumed to be due to dynamic strain aging as it also occurred in the solutionized tensile tested specimens, and coincides with the condition of the surface. One of the aims for increasing the strain rate was to see if a high enough strain rate could be achieved as to to avoid dynamic strain aging, but it was not.

Chapter 7

Future work

Regarding the slant fractures of the 7108 grade tensile test specimens there are several areas where future work would be useful to potentially identify the cause. As the investigation of the potential role of texture in the slant fractures might have been disrupted due to PFZs in the middle specimen, this could be examined further.

In the case of PFZs having affected the results presented in this report, further research on the effect of texture should be conducted where the occurrence off PFZs are eliminated by for example ensuring equal cooling rates in the different textured specimens, or choosing materials taken from flat extruded profiles and round axis-symmetric profiles and comparing those. It could also be relevant to look at other textures, for example from a cast or recrystallized material. Tensile tests should be performed on the different textured materials and the stress-strain curves compared. SE imaging and BSE imaging should also be done on the surfaces again as was done here.

The potential occurrence of a shear band should also be investigated further. This could be done using digital image correlation (DIC) during tensile testing to map out the strain in the material. The results could indicate weather a shear band forms or not, and if so when in the test it is initiated and how it behaves.

The effect of cooling rate after solutionizing could be tested for 7108 grade aluminium alloys to see if this evokes PFZs along grain boundaries. If this reveals PFZs alone grain boundaries as suspected this could help confirm that PFZs were the reason for early fracture in the middle specimen. This is however a somewhat different topic. It is also possible to look into the potential of there being two types of constituent particles, and if they behave differently during for example extrusion. This is however also somewhat unrelated.

For the incremental elongation testing further investigation could be carried out to see if dynamic strain aging can be avoided, preferably without increasing temperature or using very low strain rates. It is possible to see if there are testing methods allowing for even higher strain rates. Specimens could also be tested at different stages in the aging process

(after solutionizing) to see if a lower solute content prevents or limits dynamic strain aging, while still allowing for a greater elongation than what is achieved from tensile testing.

The behaviour of the PLC bands could also be investigated. This can be done using DIC as well during the incremental elongation testing to map out the strain in the material. The results could indicate the amount of PLC bands actually in the specimen (is there one or more), when they are initiated and how they behave in response to the incremental elongation.

In terms of damage evolution in the specimens it is unknown if voids are present mainly in and around the fracture surfaces or throughout the specimens. This could be important to investigate in terms of further understanding the potential limitations or possibilities of incremental stretching. Methods for investigating this could be polishing the lengthwise cross section of a specimen after testing and study the surface in a SEM to see if voids can be observed. X-ray tomography is another option for mapping out potential internal voids.

An investigation on the effect of texture on the incremental elongation testing could also be relevant, as only specimens taken from flat extruded profiles were used here. Both specimens with axis-symmetric textures and random textures could be tested and compared.

Bibliography

[1] C. E. Software, "Age-hardening wrought al-alloys." Granta Design Limited, 2009.

[2] S. Shah, A. Gopal, E. Thronsen, C. Hatzoglou, and B. Holmedal, "Precipitation, mechanical properties and early slant ductile fracture in cyclic and naturally aged al-zn-mg(-cu) alloys," *Materials and design*, vol. 222, p. 111026, 2022.

[3] A. Gopal, "Cyclic ageing of aluminium alloys," 2022.

[4] M. R. Sørlie, "Enhanced formability in tension by deformation induced precipitation," 2022.

[5] W. D. Callister, "Materials science and engineering," 2015.

[6] "Fundamentals of aluminium metallurgy : production, processing and applications," 2011.

[7] B. Holmestad, "Strengthening mechanisms." Forelesningsnotater, September 2021. Forelesningsnotater for NTNU TMT4222.

[8] W. F. Hosford, *Mechanical Behavior of Materials*. Cambridge: Cambridge University Press, 2005.

[9] M. Ahmadi, E. Povoden-Karadeniz, K. Öksüz, A. Falahati, and E. Kozeschnik, "A model for precipitation strengthening in multi-particle systems," *Computational Materials Science*, vol. 91, pp. 173–186, 2014.

[10] E. Kozeschnik, "Modeling solid-state precipitation," 2013.

[11] D. A. Porter, "Phase transformations in metals and alloys," 2009.

[12] N.-E. 515:2017, "Aluminium and aluminium alloys Wrought products Temper designations," standard, Standard Norge, Lysaker, Norge, 2022.

[13] H. Hallem, B. Forbord, and K. Marthinsen, "Development of aluminium alloys with ultimate recrystallisation resistance," *Materials science forum*, vol. 539-543, pp. 167–172, 2007.

[14] T. Saito, C. D. Marioara, S. J. Andersen, W. Lefebvre, and R. Holmestad, "Aberration-corrected haadf-stem investigations of precipitate structures in al-mg-si

alloys with low cu additions," *Philosophical magazine (Abingdon, England)*, vol. 94, no. 5, pp. 520–531, 2014.

[15] R. Vissers, M. van Huis, J. Jansen, H. Zandbergen, C. Marioara, and S. Andersen, "The crystal structure of the beta-prime phase in al–mg–si alloys," *Acta materialia*, vol. 55, no. 11, pp. 3815–3823, 2007.

[16] X. Chen, E. A. Mørtsell, J. K. Sunde, O. Minho, C. D. Marioara, R. Holmestad, and E. Kobayashi, "Enhanced mechanical properties in 6082 aluminum alloy processed by cyclic deformation," *Metals (Basel)*, vol. 11, no. 11, p. 1735, 2021.

[17] A. Lervik, C. Marioara, M. Kadanik, J. Walmsley, B. Milkereit, and R. Holmestad, "Precipitation in an extruded aa7003 aluminium alloy: Observations of 6xxx-type hardening phases," *Materials and design*, vol. 186, p. 108204, 2020.

[18] A. Lervik, E. Thronsen, J. Friis, C. Marioara, S. Wenner, A. Bendo, K. Matsuda, R. Holmestad, and S. Andersen, "Atomic structure of solute clusters in al–zn–mg alloys," *Acta materialia*, vol. 205, p. 116574, 2021.

[19] C. D. Marioara, W. Lefebvre, S. J. Andersen, and J. Friis, "Atomic structure of hardening precipitates in an al–mg–zn–cu alloy determined by haadf-stem and first-principles calculations: relation to eta-mgzn2," *Journal of materials science*, vol. 48, no. 10, pp. 3638–3651, 2013.

[20] Y. Zhang, D. Pelliccia, B. Milkereit, N. Kirby, M. J. Starink, and P. A. Rometsch, "Analysis of age hardening precipitates of al-zn-mg-cu alloys in a wide range of quenching rates using small angle x-ray scattering," *Materials and Design*, vol. 142, pp. 259–267, 2018.

[21] D. E. Laughlin and K. Hono, "Physical metallurgy of light alloys," in *Physical Metallurgy*, vol. 1, pp. 2009–2156, The Netherlands: Elsevier, 2014.

[22] M. Fourmeau, C. D. Marioara, T. Borvik, A. Benallal, and O. S. Hopperstad, "A study of the influence of precipitate-free zones on the strain localization and failure of the aluminium alloy aa7075-t651," *PHILOSOPHICAL MAGAZINE*, vol. 95, pp. 3278–3304, OCT 23 2015. 4th International Symposium on Instabilities Across the Scales, Paris, FRANCE, JUN 04-06, 2014.

[23] M. M. Arani, X. Wang, N. C. Parson, and W. J. Poole, "Quantification of plastic strain in the precipitate free zone of naturally aged al-mg-si alloys," in *LIGHT METALS 2022* (D. Eskin, ed.), Minerals Metals & Materials Series, pp. 241–244, Minerals Metals & Mat Soc, 2022. Light Metals Symposia at the The-Minerals-Metals-Materials-Society (TMS) Annual Meeting, Anaheim, CA, FEB 27-MAR 03, 2022.

[24] M. A. Meyers, "Mechanical behavior of materials," 2009.

[25] A. Bhaduri, "Mechanical properties and working of metals and alloys," 2018.

[26] K. Kleveland, "Formprosesser for materialer." Forelesningsnotater, January 2020. Forelesningsnotater for NTNU TMAK2008.

[27] F. J. Humphreys, "Recrystallization and related annealing phenomena," 2004.

[28] Y. Ii, P. Li, G. Zhao, X. Liu, and J. Cui, "The constituents in al–10zn–2.5mg–2.5cu aluminum alloy," *Materials science and engineering. A, Structural materials : properties, microstructure and processing*, vol. 397, no. 1, pp. 204–208, 2005.

[29] Y. guo Liao, X. qi Han, M. xia Zeng, and M. Jin, "Influence of cu on microstructure and tensile properties of 7xxx series aluminum alloy," *Materials and Design*, vol. 66, pp. 581–586, 2015. Lightweight Materials and Structural Solutions for Transport Applications.

[30] S. Suwas, "Crystallographic texture of materials," 2014.

[31] P. Rist, "The influence of transient change in strain rate on subgrain size during deformation by torsion of aa6063," 2016.

[32] J. Hjelen, "Scanning elektron-mikroskopi," 1989.

[33] "Tensile testing," 2004.

[34] B. Holmestad, "Localized necking." Forelesningsnotater, January 2022. Forelesningsnotater for NTNU TMT4266.

[35] O. Ryen, B. Holmedal, K. Marthinsen, and T. Furu, "Precipitation, strength and work hardening of age hardened aluminium alloys," in *36TH RISO INTERNATIONAL SYMPOSIUM ON MATERIALS SCIENCE*, vol. 89 of *IOP Conference Series-Materials Science and Engineering*, Tech Univ Denmark, Dept Wind Energy; Sect Mat Sci & Adv Characterizat, 2015. 36th Riso International Symposium on Materials Science, Riso, DENMARK, SEP 07-11, 2015.

[36] S. Shah, E. Thronsen, C. Hatzoglou, S. Wenner, C. D. Marioara, R. Holmestad, and B. Holmedal, "Effect of cyclic ageing on the early-stage clustering in al–zn–mg(-cu) alloys," *Materials science and engineering. A, Structural materials : properties, microstructure and processing*, vol. 846, p. 143280, 2022.

[37] A. H. Cottrell, "Dislocations and plastic flow in crystals," 1953.

[38] A. Yilmaz, "The portevin-le chatelier effect: a review of experimental findings," *Science and technology of advanced materials*, vol. 12, no. 6, pp. 063001–063001, 2011.

[39] "Multiscale modelling in sheet metal forming," 2016.

[40] J. Robinson and M. Shaw, "Observations on deformation characteristics and microstructure in an almg alloy during serrated flow," *Materials science and engineering. A, Structural materials : properties, microstructure and processing*, vol. A174, no. 1, pp. 1–7, 1994.

[41] J. Xu, B. Holmedal, O. S. Hopperstad, T. Mánik, and K. Marthinsen, "Dynamic strain ageing in an almg alloy at different strain rates and temperatures: Experiments and constitutive modelling," *International journal of plasticity*, vol. 151, p. 103215, 2022.

[42] Z. Hu, Y. Qi, X. Nie, H. Zhang, and H. Zhu, "The portevin-le chatelier (plc) effect in an al-cu aluminum alloy fabricated by selective laser melting," *Materials characterization*, vol. 178, p. 111198, 2021.

[43] Q. Zhao and B. Holmedal, "The effect of silicon on the strengthening and work hardening of aluminum at room temperature," *Materials science and engineering. A, Structural materials : properties, microstructure and processing*, vol. 563, pp. 147–151, 2013.

[44] Y. An, "Strain path change effects on stretch formability of 6082 aluminium alloy," *Materials science and technology*, vol. 17, no. 3, pp. 258–263, 2001.

[45] G. Vincze, E. Rauch, J. Gracio, F. Barlat, and A. Lopes, "A comparison of the mechanical behaviour of an aa1050 and a low carbon steel deformed upon strain reversal," *Acta Materialia*, vol. 53, no. 4, pp. 1005–1013, 2005.

[46] V. Lubarda, M. Schneider, D. Kalantar, B. Remington, and M. Meyers, "Void growth by dislocation emission," *Acta materialia*, vol. 52, no. 6, pp. 1397–1408, 2004.

[47] K. Raju, A. Mukhopadhyay, and S. Kamat, "Effect of mixed mode i/iii loading on fracture toughness of 7010 aluminium alloy," *MATERIALS SCIENCE AND TECHNOLOGY*, vol. 22, no. 1, pp. 91–96, 2006.

[48] G. LUDTKA and D. LAUGHLIN, "The influence of microstructure and strength on the fracture mode and toughness of 7xxx series aluminum-alloys," *METALLURGICAL TRANSACTIONS A-PHYSICAL METALLURGY AND MATERIALS SCIENCE*, vol. 13, no. 3, pp. 411–425, 1982.

[49] K. O. Pedersen, T. Borvik, and O. S. Hopperstad, "Fracture mechanisms of aluminium alloy aa7075-t651 under various loading conditions," *MATERIALS and DESIGN*, vol. 32, pp. 97–107, JAN 2011.

[50] T. Xu, F. Li, X. Wang, and G. Zhang, "Characterization of anisotropic fracture behavior of 7075-t6 aluminum alloy sheet under various stress states," *JOURNAL OF MATERIALS ENGINEERING AND PERFORMANCE*, vol. 32, pp. 3230–3252, APR 2023.

Appendix A

The data sets created for the incremental elongation testing are listed below in Table 7.1 for each of the strain rates.

Table 7.1: The data sets used for the incremental elongation testing for the strain rates 0,05, 0,07 and 0,1 s^{-1}.

	Strain rate: 0,05 s^{-s}		Strain rate: 0,07 s^{-s}		Strain rate: 0,1 $^{-s}$
Time [s]	Elongation fraction [mm/mm]	Time [s]	Elongation fraction [mm/mm]	Time [s]	Elongation fraction [mm/mm]
0,24691358	0,01491564	0,17636684	0,01491564	0,12345679	0,01491564
10,2469136	0,01491564	10,1763668	0,01491564	10,1234568	0,01491564
10,4938272	0,03001772	10,3527337	0,03001772	10,2469136	0,03001772
20,4938272	0,03001772	20,3527337	0,03001772	20,2469136	0,03001772
20,7407407	0,04530857	20,5291005	0,04530857	20,3703704	0,04530857
30,7407407	0,04530857	30,5291005	0,04530857	30,3703704	0,04530857
30,9876543	0,06079056	30,7054674	0,06079056	30,4938272	0,06079056
40,9876543	0,06079056	40,7054674	0,06079056	40,4938272	0,06079056
41,2345679	0,07646608	40,8818342	0,07646608	40,617284	0,07646608
51,2345679	0,07646608	50,8818342	0,07646608	50,617284	0,07646608
51,4814815	0,09233754	51,0582011	0,09233754	50,7407407	0,09233754
61,4814815	0,09233754	61,0582011	0,09233754	60,7407407	0,09233754
61,7283951	0,1084074	61,2345679	0,1084074	60,8641975	0,1084074
71,7283951	0,1084074	71,2345679	0,1084074	70,8641975	0,1084074
71,9753086	0,12467812	71,4109347	0,12467812	70,9876543	0,12467812
81,9753086	0,12467812	81,4109347	0,12467812	80,9876543	0,12467812
82,2222222	0,14115224	81,5873016	0,14115224	81,1111111	0,14115224
92,2222222	0,14115224	91,5873016	0,14115224	91,1111111	0,14115224
92,4691358	0,15783227	91,7636684	0,15783227	91,2345679	0,15783227

307,407407	0,538888
307,654321	0,56053974
317,654321	0,56053974
317,901235	0,58246212
327,901235	0,58246212
328,148148	0,60465853
338,148148	0,60465853
338,395062	0,6271324
348,395062	0,6271324
348,641975	0,64988719
358,641975	0,64988719
358,888889	0,67292641
368,888889	0,67292641
369,135803	0,69625363
379,135803	0,69625363
379,382716	0,71987243
389,382716	0,71987243
389,62963	0,74378647
399,62963	0,74378647
399,876543	0,76799944
409,876543	0,76799944
410,123457	0,79251507
420,123457	0,79251507
420,37037	0,81733714
430,37037	0,81733714
430,617284	0,84246949
440,617284	0,84246949
440,864198	0,86791599
450,864198	0,86791599
451,111111	0,89368058
461,111111	0,89368058
461,358025	0,91976722
471,358025	0,91976722
471,604938	0,94617995
481,604938	0,94617995
481,851852	0,97292283
491,851852	0,97292283
492,098765	1
502,098765	1

305,291005	0,538888
305,467372	0,56053974
315,467372	0,56053974
315,643739	0,58246212
325,643739	0,58246212
325,820106	0,60465853
335,820106	0,60465853
335,996473	0,6271324
345,996473	0,6271324
346,17284	0,64988719
356,17284	0,64988719
356,349206	0,67292641
366,349206	0,67292641
366,525573	0,69625363
376,525573	0,69625363
376,70194	0,71987243
386,70194	0,71987243
386,878307	0,74378647
396,878307	0,74378647
397,054674	0,76799944
407,054674	0,76799944
407,231041	0,79251507
417,231041	0,79251507
417,407407	0,81733714
427,407407	0,81733714
427,583774	0,84246949
437,583774	0,84246949
437,760141	0,86791599
447,760141	0,86791599
447,936508	0,89368058
457,936508	0,89368058
458,112875	0,91976722
468,112875	0,91976722
468,289242	0,94617995
478,289242	0,94617995
478,465609	0,97292283
488,465609	0,97292283
488,641975	1
498,641975	1

303,703704	0,538888
303,827161	0,56053974
313,827161	0,56053974
313,950617	0,58246212
323,950617	0,58246212
324,074074	0,60465853
334,074074	0,60465853
334,197531	0,6271324
344,197531	0,6271324
344,320988	0,64988719
354,320988	0,64988719
354,444444	0,67292641
364,444444	0,67292641
364,567901	0,69625363
374,567901	0,69625363
374,691358	0,71987243
384,691358	0,71987243
384,814815	0,74378647
394,814815	0,74378647
394,938272	0,76799944
404,938272	0,76799944
405,061728	0,79251507
415,061728	0,79251507
415,185185	0,81733714
425,185185	0,81733714
425,308642	0,84246949
435,308642	0,84246949
435,432099	0,86791599
445,432099	0,86791599
445,555556	0,89368058
455,555556	0,89368058
455,679012	0,91976722
465,679012	0,91976722
465,802469	0,94617995
475,802469	0,94617995
475,925926	0,97292283
485,925926	0,97292283
486,049383	1
496,049383	1

307,407407	0,538888
307,654321	0,56053974
317,654321	0,56053974
317,901235	0,58246212
327,901235	0,58246212
328,148148	0,60465853
338,148148	0,60465853
338,395062	0,6271324
348,395062	0,6271324
348,641975	0,64988719
358,641975	0,64988719
358,888889	0,67292641
368,888889	0,67292641
369,135803	0,69625363
379,135803	0,69625363
379,382716	0,71987243
389,382716	0,71987243
389,62963	0,74378647
399,62963	0,74378647
399,876543	0,76799944
409,876543	0,76799944
410,123457	0,79251507
420,123457	0,79251507
420,37037	0,81733714
430,37037	0,81733714
430,617284	0,84246949
440,617284	0,84246949
440,864198	0,86791599
450,864198	0,86791599
451,111111	0,89368058
461,111111	0,89368058
461,358025	0,91976722
471,358025	0,91976722
471,604938	0,94617995
481,604938	0,94617995
481,851852	0,97292283
491,851852	0,97292283
492,098765	1
502,098765	1

305,291005	0,538888
305,467372	0,56053974
315,467372	0,56053974
315,643739	0,58246212
325,643739	0,58246212
325,820106	0,60465853
335,820106	0,60465853
335,996473	0,6271324
345,996473	0,6271324
346,17284	0,64988719
356,17284	0,64988719
356,349206	0,67292641
366,349206	0,67292641
366,525573	0,69625363
376,525573	0,69625363
376,70194	0,71987243
386,70194	0,71987243
386,878307	0,74378647
396,878307	0,74378647
397,054674	0,76799944
407,054674	0,76799944
407,231041	0,79251507
417,231041	0,79251507
417,407407	0,81733714
427,407407	0,81733714
427,583774	0,84246949
437,583774	0,84246949
437,760141	0,86791599
447,760141	0,86791599
447,936508	0,89368058
457,936508	0,89368058
458,112875	0,91976722
468,112875	0,91976722
468,289242	0,94617995
478,289242	0,94617995
478,465609	0,97292283
488,465609	0,97292283
488,641975	1
498,641975	1

303,703704	0,538888
303,827161	0,56053974
313,827161	0,56053974
313,950617	0,58246212
323,950617	0,58246212
324,074074	0,60465853
334,074074	0,60465853
334,197531	0,6271324
344,197531	0,6271324
344,320988	0,64988719
354,320988	0,64988719
354,444444	0,67292641
364,444444	0,67292641
364,567901	0,69625363
374,567901	0,69625363
374,691358	0,71987243
384,691358	0,71987243
384,814815	0,74378647
394,814815	0,74378647
394,938272	0,76799944
404,938272	0,76799944
405,061728	0,79251507
415,061728	0,79251507
415,185185	0,81733714
425,185185	0,81733714
425,308642	0,84246949
435,308642	0,84246949
435,432099	0,86791599
445,432099	0,86791599
445,555556	0,89368058
455,555556	0,89368058
455,679012	0,91976722
465,679012	0,91976722
465,802469	0,94617995
475,802469	0,94617995
475,925926	0,97292283
485,925926	0,97292283
486,049383	1
496,049383	1

Appendix B

The width and thicknesses of the rectangular specimens before and after tensile testing are listed in Table 7.2. These were used to calculate the r-value and the theoretical θ angles for each of the three specimens.

Table 7.2: The thickness and width of the and width of the rectangular specimens before tensile testing (w_0 t_0) and after tensile testing (w and t).

	w_0	t_0	w	t
Rectangular 1	24,1	2,91	23,59	2,73
Rectangular 2	24	2,94	23,61	2,69
Rectangular 3	24,08	2,9	23,48	2,7

Appendix C

The raw data collected from the tensile testing program is listed below in Tables 7.3 and 7.4 for the specimens from the 7108 massive and flat extruded profiles.

Table 7.3: The raw data collected from the tensile testing program for the middle and edge specimens.

Sample	t_0	w_0	Strain Rate	Area	Modulus	Stress At Offset Yield	Peak Load	Peak Stress	Strain At Break	Strain At Offset Yield
I. D.	mm	mm	mm/ min	mm^2	GPa	MPa	kN	MPa	%	mm/ mm
Middle 1	6	6,1	2	36,6	69,227	268,2	13,863	378,8	****	0,00585
Middle 2	6,06	6,08	2	36,84	71,079	272,8	15,107	410	****	0,00513
Middle 3	6,06	6,13	2	37,15	70,359	275,4	14,958	402,7	21,5	0,00594
Edge 1	6,06	6,1	2	36,97	70,182	348,5	17,948	485,5	11,7	0,00627
Edge 2	6,07	6,14	2	37,27	69,54	358,2	18,22	488,9	****	0,0071
Edge 3	6,05	6,08	2	36,78	73,594	348,1	17,996	489,2	****	0,00662

Table 7.4: The raw data collected from the tensile testing program for the square and rectangular specimens.

Sample	t_0	w_0	Strain Rate	Area	Modulus	Stress At Offset Yield	Peak Load	Peak Stress	Strain At Break	Strain At Offset Yield
I. D.	mm	mm	mm/ min	mm^2	GPa	MPa	kN	MPa	%	mm/ mm
Square 1	3,02	2,93	2	8,85	71,578	293,8	3,892	439,9	14,6	0,00605
Square 2	3,12	3,11	2	9,7	62,468	273,4	3,855	397,3	****	0,0064
Square 3	2,99	2,92	2	8,73	70,904	292	3,821	437,7	16,1	0,00602
Rectangular 1	2,91	24,1	2	70,13	69,833	298,1	30,285	431,8	****	0,00632
Rectangular 2	2,94	24,01	2	70,59	74,069	298,1	30,219	428,1	****	0,00595
Rectangular 3	2,9	24,08	2	69,83	70,162	300,4	30,605	438,3	11,5	0,00628

Appendix D

The detected weight percentages, atom percent and the weight percent error from point 1-4 of the EDS analysis of the fracture surface of the 7108 edge specimen.

Table 7.5: Weight percentages, atom percent and the error from the point 1 of EDS analysis of the 7108 edge specimen.

El AN Series	unn. C [wt%]	norm. C [wt%]	Atom. C [wt%]	Error (1 Sigma) [wt%]
Al 13 K-series	85,01	90,73	94,25	3,84
Zn 30 L-series	6,66	7,1	3,04	0,44
Mg 12 K-series	1,72	1,84	2,12	0,12
O 8 K-series	0,31	0,33	0,58	0,12
Total	93,7	100	100	

Table 7.6: Weight percentages, atom percent and the error from the point 2 of EDS analysis of the 7108 edge specimen.

El AN Series	unn. C [wt%]	norm. C [wt%]	Atom. C [wt%]	Error (1 Sigma) [wt%]
Al 13 K-series	66,39	60,03	73,73	3
Zn 30 L-series	3,49	3,16	1,6	0,25
Mg 12 K-series	1,16	1,05	1,43	0,09
Fe 26 K-series	37,54	33,94	20,14	1,8
Si 14 K-series	0,84	0,76	0,89	0,07
O 8 K-series	1,18	1,07	2,21	0,26
Total	110,61	100	100	

Table 7.7: Weight percentages, atom percent and the error from the point 3 of EDS analysis of the 7108 edge specimen.

El AN Series	unn. C [wt%]	norm. C [wt%]	Atom. C [wt%]	Error (1 Sigma) [wt%]
Al 13 K-series	77,46	70,9	80,83	3,5
Zn 30 L-series	5,77	5,28	2,49	0,39
Mg 12 K-series	1,52	1,39	1,76	0,11
Fe 26 K-series	22,08	20,21	11,13	1,13
Si 14 K-series	0,64	0,58	0,64	0,06
O 8 K-series	1,79	1,64	3,15	0,36
Total	109,26	100	100	

Table 7.8: Weight percentages, atom percent and the error from the point 4 of EDS analysis of the 7108 edge specimen.

El AN Series	unn. C [wt%]	norm. C [wt%]	Atom. C [wt%]	Error (1 Sigma) [wt%]
Al 13 K-series	57,92	59,48	73,53	2,62
Zn 30 L-series	1,98	2,04	1,04	0,16
Mg 12 K-series	0,84	0,86	1,18	0,07
Fe 26 K-series	35,07	36,01	21,51	1,69
Si 14 K-series	0,68	0,7	0,83	0,06
O 8 K-series	0,89	0,86	1,18	0,07
Total	97,38	100	100	

The detected weight percentages, atom percent and the weight percent error from point 1-4 of the EDS analysis of the fracture surface of the 7108 middle specimen.

Table 7.9: Weight percentages, atom percent and the error from point 1 of the EDS analysis of the 7108 middle specimen.

El AN Series	unn. C [wt%]	norm. C [wt%]	Atom. C [wt%]	Error (1 Sigma) [wt%]
Al 13 K-series	82,03	89,92	93,45	3,7
Zn 30 L-series	6,84	7,5	3,21	0,45
Mg 12 K-series	1,7	1,86	2,14	0,12
Si 14 K-series	0,09	0,62	1,09	0,17
O 8 K-series	0,57	0,62	1,09	0,17
Total	91,22	100	100	

Table 7.10: Weight percentages, atom percent and the error from point 2 of the EDS analysis of the 7108 middle specimen.

El AN Series	unn. C [wt%]	norm. C [wt%]	Atom. C [wt%]	Error (1 Sigma) [wt%]
Al 13 K-series	56,05	58,26	71,52	2,54
Zn 30 L-series	3,15	3,27	1,66	0,23
Mg 12 K-series	0,75	0,78	1,06	0,07
Fe 26 K-series	31,95	33,21	19,7	1,56
Si 14 K-series	3,49	3,63	4,28	0,18
O 8 K-series	0,83	0,86	1,79	0,21
Total	97,38	100	100	

Table 7.11: Weight percentages, atom percent and the error from point 3 of the EDS analysis of the 7108 middle specimen.

El AN Series	unn. C [wt%]	norm. C [wt%]	Atom. C [wt%]	Error (1 Sigma) [wt%]
Al 13 K-series	58,67	44,47	62,23	2,67
Zn 30 L-series	2,02	1,53	0,88	0,18
Mg 12 K-series	0,56	0,43	0,66	0,07
Fe 26 K-series	70,68	53,57	36,22	3,43
Total	131,93	100	100	

Table 7.12: Weight percentages, atom percent and the error from point 4 of the EDS analysis of the 7108 middle specimen.

El AN Series	unn. C [wt%]	norm. C [wt%]	Atom. C [wt%]	Error (1 Sigma) [wt%]
Al 13 K-series	74,53	68	81,09	3,37
Zn 30 L-series	3,57	3,26	1,6	0,27
Mg 12 K-series	1,11	1,01	1,34	0,09
Fe 26 K-series	30,38	27,72	15,97	1,6
Total	109,59	100	100	

The detected weight percentages, atom percent and the weight percent error from point 1-4 of the EDS analysis of the fracture surface of the 7108 rectangular specimen.

Table 7.13: Weight percentages, atom percent and the error from point 1 of the EDS analysis of the 7108 rectangular specimen.

El AN Series	unn. C [wt%]	norm. C [wt%]	Atom. C [wt%]	Error (1 Sigma) [wt%]
Al 13 K-series	59,52	93,63	95,65	2,69
Zn 30 L-series	2,47	3,89	1,64	0,18
Mg 12 K-series	0,86	1,36	1,54	0,07
O 8 K-series	0,05	0,09	0,15	0,04
Si 14 K-series	0,66	1,04	1,02	0,05
Total	63,56	100	100	

Table 7.14: Weight percentages, atom percent and the error from point 2 of the EDS analysis of the 7108 rectangular specimen.

El AN Series	unn. C [wt%]	norm. C [wt%]	Atom. C [wt%]	Error (1 Sigma) [wt%]
Al 13 K-series	60,1	77,76	86,6	2,71
Zn 30 L-series	2,81	3,64	1,67	0,2
Mg 12 K-series	0,94	1,21	1,5	0,07
Fe 26 K-series	12,25	15,85	8,53	0,58
Si 14 K-series	1,13	1,47	1,57	0,07
O 8 K-series	0,06	0,07	0,14	0,04
Total	77,29	100	100	

Table 7.15: Weight percentages, atom percent and the error from point 3 of the EDS analysis of the 7108 rectangular specimen.

El AN Series	unn. C [wt%]	norm. C [wt%]	Atom. C [wt%]	Error (1 Sigma) [wt%]
Al 13 K-series	44,54	81,56	86,29	2,02
Zn 30 L-series	2,99	5,48	2,39	0,21
Mg 12 K-series	1,07	1,96	2,3	0,08
Fe 26 K-series	2,34	4,28	2,19	0,15
Si 14 K-series	3,66	6,71	6,82	0,18
Total	54,61	100	100	

Table 7.16: Weight percentages, atom percent and the error from point 4 of the EDS analysis of the 7108 rectangular specimen.

El AN Series	unn. C [wt%]	norm. C [wt%]	Atom. C [wt%]	Error (1 Sigma) [wt%]
Al 13 K-series	55,98	71,03	82,58	2,53
Zn 30 L-series	2,04	2,59	1,24	0,15
Mg 12 K-series	0,8	1,02	1,31	0,07
Fe 26 K-series	19,12	24,26	13,63	0,88
Si 14 K-series	0,87	1,11	1,24	0,06
Total	78,81	100	100	

The detected weight percentages, atom percent and the weight percent error from point 1-4 of EDS analysis 1 of the fracture surface of the 7003 grade specimen.

Table 7.17: Weight percentages, atom percent and the error from the point 1 of EDS analysis 1 of the 7003 specimen.

El AN Series	unn. C [wt%]	norm. C [wt%]	Atom. C [wt%]	Error (1 Sigma) [wt%]
Al 13 K-series	60,19	95,44	97,17	2,72
Zn 30 L-series	2,15	3,41	1,43	0,16
Mg 12 K-series	0,62	0,98	1,11	0,06
O 8 K-series	0,11	0,17	0,29	0,05
Total	63,07	100	100	

Table 7.18: Weight percentages, atom percent and the error from the point 2 of EDS analysis 1 of the 7003 specimen.

El AN Series	unn. C [wt%]	norm. C [wt%]	Atom. C [wt%]	Error (1 Sigma) [wt%]
Al 13 K-series	48,53	59,63	72,99	2,2
Zn 30 L-series	2,17	2,67	1,35	0,16
Mg 12 K-series	0,57	0,7	0,96	0,06
Fe 26 K-series	26,17	32,16	19,02	1,18
Si 14 K-series	3,93	4,83	5,68	0,19
Total	81,38	100	100	

Table 7.19: Weight percentages, atom percent and the error from the point 3 of EDS analysis 1 of the 7003 specimen.

El AN Series	unn. C [wt%]	norm. C [wt%]	Atom. C [wt%]	Error (1 Sigma) [wt%]
Al 13 K-series	50,63	71,5	81,5	2,29
Zn 30 L-series	2,66	3,75	1,77	0,19
Mg 12 K-series	0,63	0,89	1,13	0,06
Fe 26 K-series	13,68	19,32	10,64	0,64
Si 14 K-series	3,21	4,53	4,96	0,16
Total	70,81	100	100	

Table 7.20: Weight percentages, atom percent and the error from the point 4 of EDS analysis 1 of the 7003 specimen.

El AN Series	unn. C [wt%]	norm. C [wt%]	Atom. C [wt%]	Error (1 Sigma) [wt%]
Al 13 K-series	48,34	63,37	75,08	2,19
Zn 30 L-series	2,64	2,64	1,69	0,19
Mg 12 K-series	0,61	0,8	0,8	0,06
Fe 26 K-series	20	26,22	15,01	0,92
Si 14 K-series	4,53	5,94	6,76	0,21
O 8 K-series	0,16	0,21	0,41	0,06
Total	76,28	100	100	

The detected weight percentages, atom percent and the weight percent error from point 1-4 of EDS analysis 2 of the fracture surface of the 7003 grade sample.

Table 7.21: Weight percentages, atom percent and the error from the point 1 of EDS analysis 2 of the 7003 specimen.

El AN Series	unn. C [wt%]	norm. C [wt%]	Atom. C [wt%]	Error (1 Sigma) [wt%]
Al 13 K-series	54,47	92,26	94,8	2,46
Zn 30 L-series	2,78	4,7	1,99	0,2
Mg 12 K-series	0,78	1,32	1,5	0,07
Si 14 K-series	1,02	1,72	1,7	0,07
Total	63,07	100	100	

Table 7.22: Weight percentages, atom percent and the error from the point 2 of EDS analysis 2 of the 7003 specimen.

El AN Series	unn. C [wt%]	norm. C [wt%]	Atom. C [wt%]	Error (1 Sigma) [wt%]
Al 13 K-series	45,25	58,69	72,37	2,05
Zn 30 L-series	1,73	2,24	1,14	0,13
Mg 12 K-series	0,4	0,52	0,71	0,05
Fe 26 K-series	26,05	33,79	20,13	1,18
Si 14 K-series	3,68	4,77	5,65	0,18
Total	77,11	100	100	

Table 7.23: Weight percentages, atom percent and the error from the point 3 of EDS analysis 2 of the 7003 specimen.

El AN Series	unn. C [wt%]	norm. C [wt%]	Atom. C [wt%]	Error (1 Sigma) [wt%]
Al 13 K-series	49,01	61,42	73,85	2,22
Zn 30 L-series	2,64	3,31	1,64	0,19
Mg 12 K-series	0,63	0,79	1,05	0,06
Fe 26 K-series	22,77	28,53	16,57	1,04
Si 14 K-series	4,75	5,96	6,88	0,22
Total	79,81	100	100	

Table 7.24: Weight percentages, atom percent and the error from the point 4 of EDS analysis 2 of the 7003 specimen.

El AN Series	unn. C [wt%]	norm. C [wt%]	Atom. C [wt%]	Error (1 Sigma) [wt%]
Al 13 K-series	53,05	79,79	87,57	2,4
Zn 30 L-series	2,95	4,44	2,01	0,21
Mg 12 K-series	0,77	1,15	1,4	0,07
Fe 26 K-series	8,11	12,2	6,47	0,4
Si 14 K-series	1,61	2,42	2,55	0,09
Total	66,48	100	100	

Appendix E

The results from the SE imaging and EDS analysis of the incremental elongation tested 6082 specimens from "Enhanced formability in tension by deformation induced precipitation" are presented below. The SE images are shown in Figure 7.1. Figure 7.2 show the points that were scanned during the EDS analysis, and these scans are presented in Figures 7.3-7.5. Table 7.25 summarises the weight percentages of Fe, Mn and Cr detected in each point.

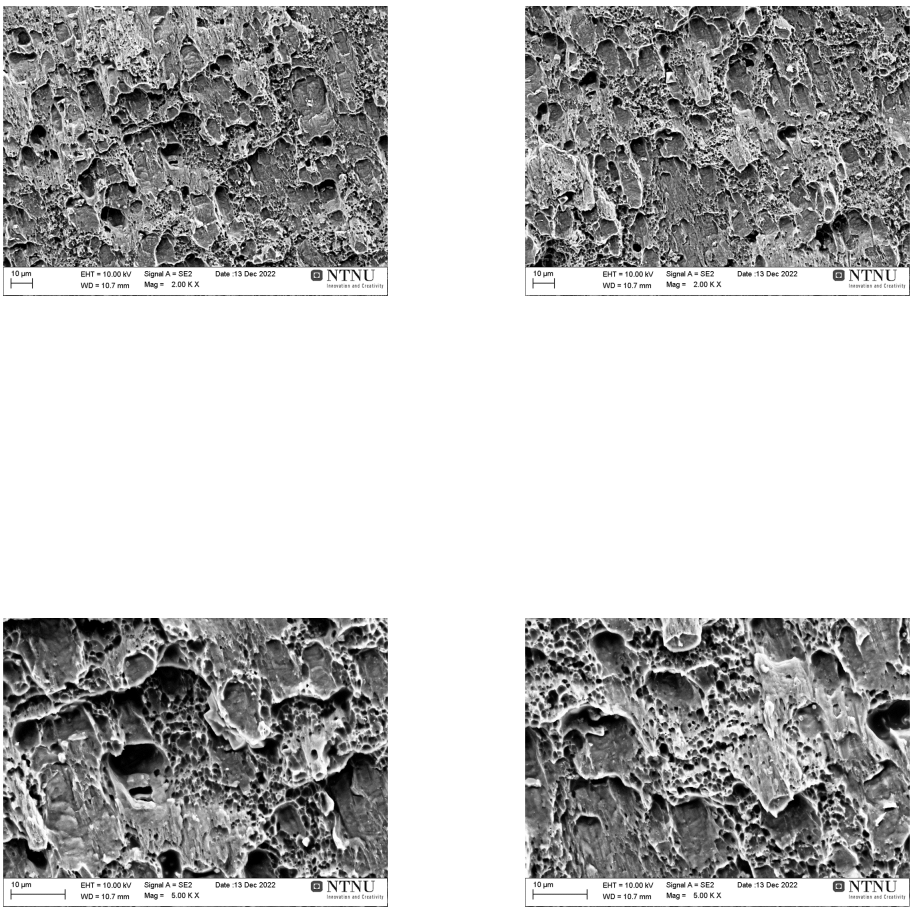

Figure 7.1: SE images from two areas of the fracture surface, at two different magnifications. 2k x and 5k x.

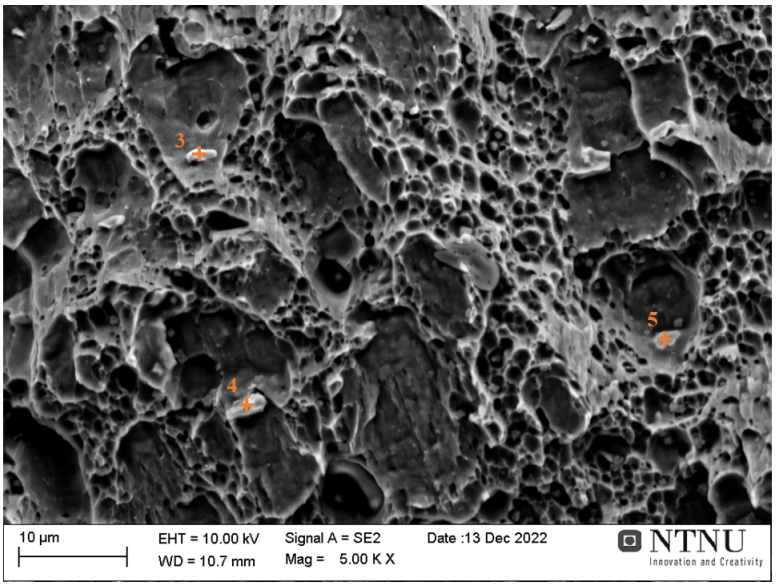

Figure 7.2: SE image at a magnification of 5k x with the three crosses showing the particles the EDS analysis was done on.

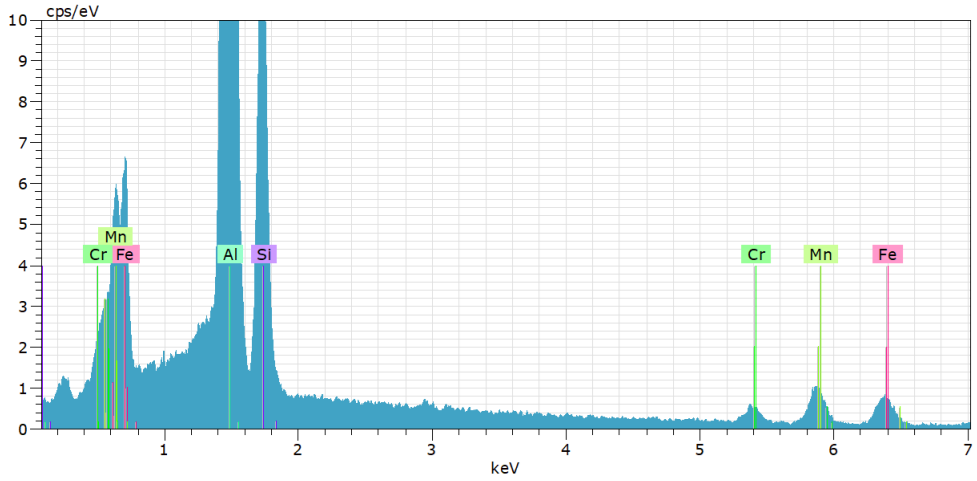

Figure 7.3: Resulting graph of the EDS scan of point 3.

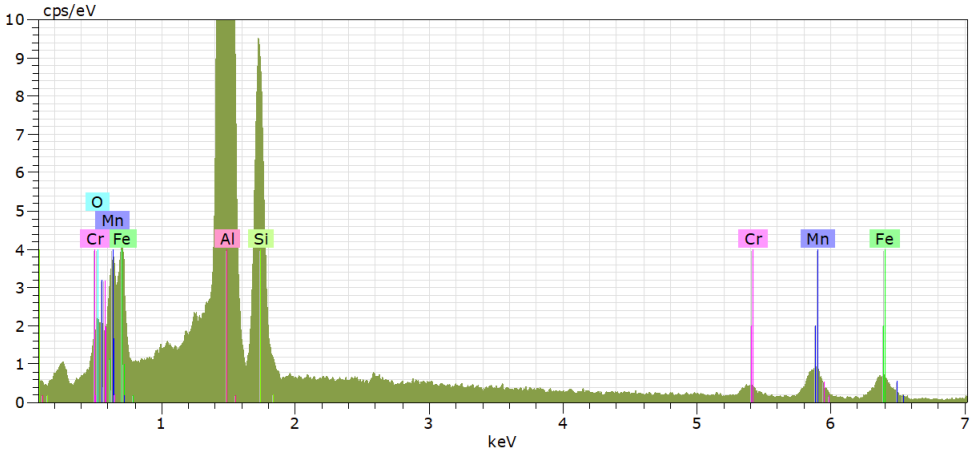

Figure 7.4: Resulting graph of the EDS scan of point 4.

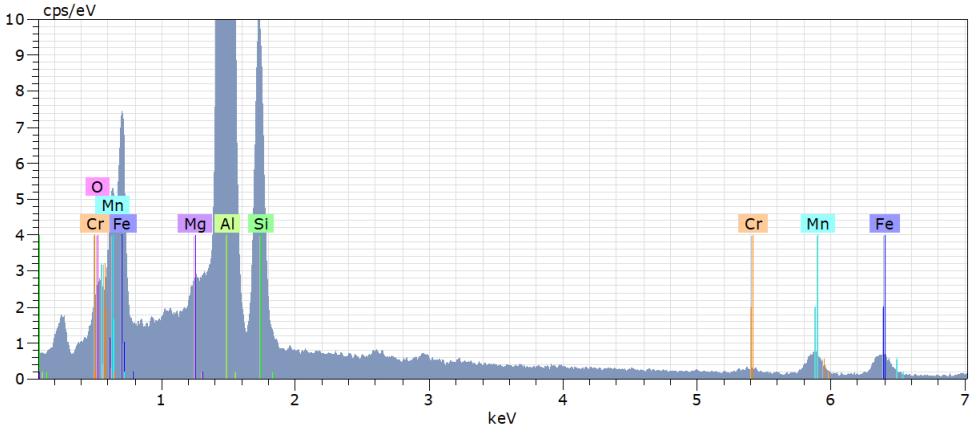

Figure 7.5: Resulting graph of the EDS scan of point 5.

Table 7.25: The amounts of iron, manganese and chromium in the particles in wt%.

	Point 3	Point 4	Point 5
Fe [wt%]	11,57	13,61	11,97
Mn [wt%]	9,32	11,02	7,43
Cr [wt%]	2,38	2,71	0,98

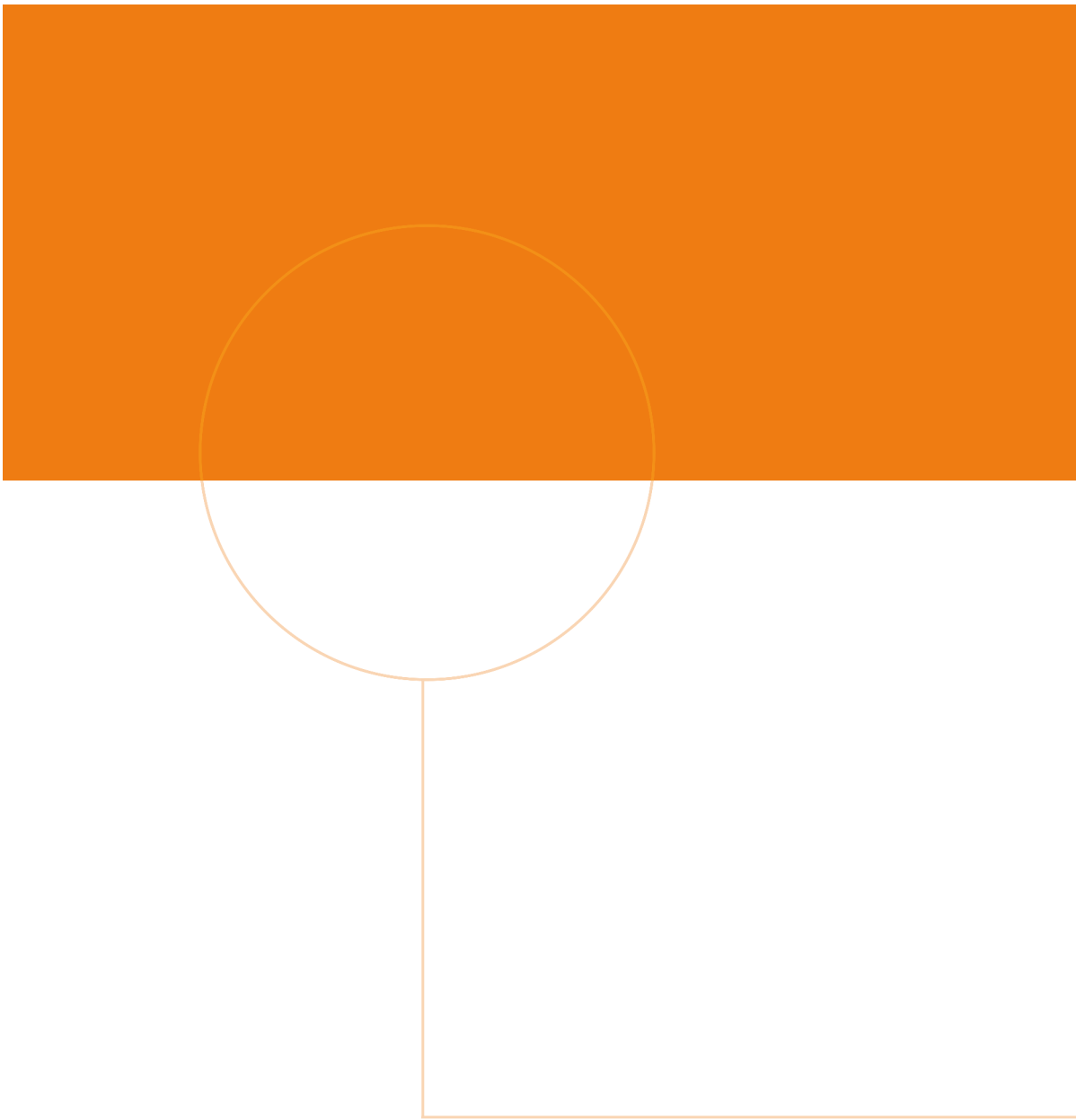

NTNU

Norwegian University of
Science and Technology